Selective Area Growth Techniques Using Metal Organic Chemical Vapour Deposition for III-V Semiconductor Quantum Well Laser Devices

Selective Area Growth Techniques Using Metal Organic Chemical Vapour Deposition for III-V Semiconductor Quantum Well Laser Devices

By

David McShannon

B.Eng.

A Thesis

Submitted to the School of Graduate Studies

in Partial Fulfillment of the Requirements

for the Degree

Master of Applied Science

McMaster University

© Copyright by David McShannon, September 2021

MASTER OF APPLIED SCIENCE (2021) MCMASTER UNIVERSITY

Department of Engineering Physics Hamilton, Ontario

TITLE:

Selective Area Growth Techniques Using Metal Organic Chemical Vapour Deposition for III-V Semiconductor Quantum Well Laser Devices

AUTHOR:

David McShannon, B.Eng, McMaster University (Hamilton, Ontario, Canada)

SUPERVISOR:

Professor Rafael N. Kleiman

NUMBER OF PAGES: VII, 101

Abstract

Selective area growth (SAG) is a technique used for semiconductor manufacturing to alter the epitaxial growth formation on the surface of a substrate. Surface feature modifications allow for local area semiconductor growth manipulation, increasing flux in the vicinity of non-growth mask edges. GaAs (100) wafers were processed with photolithographic direct laser pattern writing to create a series of silica rectangular prism masks on the surface of the substrate. The non-growth centers possess a very low sticking coefficient when placed within a metal-organic chemical vapour deposition (MOCVD) chamber with respect to the semiconductor materials deployed. In this work the establishment of a robust MOCVD process flow leading up to InGaAs compounds is defined at McMaster University's Centre of Emerging Device Technologies. Quantum-well laser devices were fabricated in surface cavities to highlight the capabilities of SAG with MOCVD. A micro-photoluminescence device was manufactured with spatial resolution to test quantum-well emission spectra. The growth mechanics and photoluminescence of the quantum-well lasers were examined and characterized to improve the parametric control of the MOCVD process flow.

Acknowledgements

I would like to thank my supervisor, Dr. Rafael Kleiman, for his consistent and knowledgeable support throughout my graduate degree. To Alaa Sharafeldin, thank you for your significant work ethic and notable teamwork on this project. To Shuiawen Gao, Anna De Leenheer, Taz Colangelo, Ruslan Khabibrakhmanov, Paramita Bhattacharyya and Dawson Bonneville, thank you for your suggestions and support in my experiments.

A special thank you to Doris Stevanovic, Shahram Tavakoli and Manu Hegde for their professional and timely experimental support in the CEDT facilities.

I would also like to extend a big thank you to my family and close friends who provided me invaluable encouragement throughout this degree.

Table of Contents

Abstract I
Acknowledgements II
List of Figures IV
List of Tables VII
1. Objective 1
  1.1. Introduction 1
  1.2. Photonic Integrated Circuitry 4
2. Literature Review 6
  2.1. Semiconductor Heterostructures 6
  2.2. Selective Area Growth 17
3. Experimental Procedure 27
  3.1. Semiconductor Wafer Processing 27
  3.2. Metal-Organic Chemical Vapour Deposition (MOCVD) 34
  3.3. Micro-Photoluminescence Detection with Spatial Resolution 38
  3.4. Post-Processing Evaluation 53
4. Results 57
  4.1. Growth Mechanics 57
    4.1.1. Scanning Electron Microscopy 60
    4.1.2. Atomic Force Microscopy 76
  4.2. Photoluminescence 81
5. Conclusion 91
  5.1. Conclusion 91
  5.2. Future Work 92
6. References 93
7. Appendices 97
  7.1. Appendix A 97
  7.2. Appendix B 101

List of Figures

Figure 1: Superinjection of Carriers (a) and Electrical Confinement (b) [8]

Figure 2: Lattice Parameters of Various Semiconductor Materials [12]

Figure 3: MBE Growth Chamber Schematic [20]

Figure 4: MOVPE System Schematic [21]

Figure 5: Basic Quantum-Well Energy Band Structure [24]

Figure 6: Layer Schematic of GaN Quantum-Well Laser [24]

Figure 7: SAG Schematic [26]

Figure 8: SAG Mask Structure [5]

Figure 9: Simulation Setup for SAG Mask Design [5]

Figure 10: SAG Mask Thickness Compared to Emission Wavelength of Quantum-Well Lasers [32]

Figure 11: Basic Schematic of CVD Reaction Chamber [34]

Figure 12: CIF File for Masking Design

Figure 13: Optical Microscopy Image of Mask Design During Photolithographic Processing

Figure 14: Photolithographic Processing Procedure [36]

Figure 15: McMaster University MOCVD Chamber

Figure 16: MOCVD at McMaster University

Figure 17: Basis of Photoluminescence in Semiconductors [38]

Figure 18: Dichroic Mirror Placement above XY Stage

Figure 19: Laser Emission Wavelength Calibration for 532 nm Nd:YAG Frequency Doubled

Figure 20: Basis of Lock-In Amplification [39]

Figure 21: Calibration Testing Example for ND:YAG Laser without Lock-In Amplification (2 Second Time Steps)

Figure 22: Calibration Testing Example for ND:YAG Laser without Lock-In Amplification (1 Second Time Steps)

Figure 23: Calibration Test for Sample X's GaAs Substrate Photoluminescence using Nd:YAG Laser with Lock-In Amplification

Figure 24: Sample X Tested for GaAs Substrate Photoluminescence with Ge/Si Detectors

Figure 25: Model 2032-UV-Silicon Responsivity Provided by Supplier Manual

Figure 26: Model 2033-IR-Germanium Responsivity Provided by Supplier Manual

Figure 27: Nd:YAG Laser in μ-PL Setup

Figure 28: Schematic of SEM Basis [40]

Figure 29: Schematic of AFM Basis [41]

Figure 30: S-28 Structure of Grown GaAs Quantum-Well

Figure 31: Optical Microscopy Image of Silica Masking Repeated Across the Substrate Surface

Figure 32: GaAs Wafer Cleaved for SEM Imaging with Silica Masking Repeated Across the Substrate Surface

Figure 33: SEM Image of Silica Masking on GaAs Substrate for Silica Mask Sizing Calibration

Figure 34: SEM Image of Silica Mask Structure on a GaAs Substrate with 20 μm Width

Figure 35: SEM Image of Silica Mask Structure on a GaAs Substrate with 10 μm Width

Figure 36: SEM Image of Quantum-Well Laser Cavity Surrounded by Silica Masking on GaAs Substrate (S-34)

Figure 37: SEM Image of Quantum-Well Laser Cavity in the Vicinity of the Mask Edge on GaAs Substrate (S-34)

Figure 38: Figure 37: SEM Image Down the Quantum-Well Laser Cavity on GaAs Substrate (S-34)

Figure 39: SEM Image of Mask Edge Defects on GaAs Substrate (S-34)

Figure 40: SEM Image of Silica Masking Structures on GaAs Substrate (S-34)

Figure 41: SEM Image of Silica Masking with High Contrast on GaAs Substrate (S-34)

Figure 42: SEM Image of Silica Masking with Low Contrast on GaAs Substrate (S-34)

Figure 43: Closeup SEM Image of Mask Edge on GaAs Substrate (S-34)

Figure 44: Cross-Sectional Image of Silica Mask (Dark) beside MOCVD Growth (Light) Demonstrating SAG (S-34)

Figure 45: Closeup Cross-Sectional Image of Silica Mask (Dark) beside MOCVD Growth (Light) Demonstrating SAG (S-34)

Figure 46: AFM Image of S-28 Surface - Atomic Terraces

Figure 47: AFM Image Zoomed In on Atomic Terraces (S-28)

Figure 48: AFM Image of Silica Masking (Dark) beside MOCVD Growth (Light) (S-34)

Figure 49: AFM Image of Laser Cavity (S-34)

Figure 50: S-28 Photoluminescence Output with AN Bourns Science Building Photoluminescence System at Room Temperature

Figure 51: S-31 Photoluminescence Output with AN Bourns Science Building Photoluminescence System at Room Temperature

Figure 52: S-32 Photoluminescence Output with AN Bourns Science Building Photoluminescence System at Room Temperature

Figure 53: HeNe Photoluminescence Setup

Figure 54: HeNe Chopper Mechanism Leading to Division of Photoluminescence Output by Dichroic Beamsplitter

Figure 55: Schematic of μ-PL System

Figure 56: Photoluminescence Output using New Setup (HeNe with Chopper Mechanism) for S-31 with Germanium and Silicon Photodetectors

Figure 57: Photoluminescence Output using New Setup (HeNe with Chopper Mechanism) for S-32 with Germanium and Silicon Photodetectors

Figure A.1: E-k curve for available quantum mechanical states [44]

Figure A.2: The density of states as a function of E for different dimensions [45]

Figure B.1: Quantum Confined Stark Effect (QCSE) - Quantum-well subband bending due to an applied electric field [46]

List of Tables

Table 1: InGaAs Samples

1. Objective

1.1. Introduction

The evolution of electronic integrated circuitry is arriving at the limit of its integration capacity. The consumer and commercial electronic marketplaces have been resilient and consistent in the past five decades following a famous pattern referred to as Moore's Law [1]. The number of transistors on microchips, as predicted, has followed a doubling capacity every two years for the past fifty-six years. This prediction has stood the test of time until recent cycles in which quantum mechanical limitations have been approached. The exponential miniaturization of electronics that has continuously followed this law, is set to flatten by 2025 due to near atomic scaling of transistors and a steady increase in fabrication costs at this scale [2]. The question driving innovation in computing is therefore simply stated - is it possible for high-performance electronics to continue this trend?

To challenge this shortfall of compacting with continuous improvement, a 3-dimensional approach in which the traditional packing of transistors is expanded to a 3-dimensional interconnect has been explored. Fundamentally, this method is quite intuitive, however, interconnecting off-chip in a new degree of freedom has presented a plethora of unique engineering and material science challenges. Undeterred, is the realization that ordinary silicon technology, either a 3-dimensional interconnecting approach, or a 3-dimensionally designed transistor such as the FinFET (fin field-effect transistor), are approaching an intrinsic operational capacity. This technological recognition has become a catalyst for the global research and development of alternative methods for digital computing. This is not to be confused with quantum or brain-inspired computation techniques which cannot, for the foreseeable future,

reproduce high quality graphic rendering or word processing. This realization is strictly a generational technological revision analogous to the advancement from vacuum tubes to modern day semiconductors.

With an unrelenting consumer basis built on proven, predictable product development for the past fifty-six years, there lies an immense background engineering undertaking and opportunity for innovation. Alternative digital computing devices hold an abundance of possibility, with engineering companies around the globe in the pursuit of the next great computational driven device. The answer of computability, compatibility, and the ability to compact, cannot be fully resolved presently, leaving the door wide open to substitute materials and technologies. One current main technological branch of exploration is photonic integration, the use of laser light connected within the electronic circuitry. This can be referred to as the integration of photonics with existing electrical components or also known as, optoelectronics.

Optoelectronic integration was first developed to overcome the necessary immense CPU/GPU off-chip bandwidth control. The well-defined laser technologies were adapted because of their bandwidth density and energy efficiency advantages [2]. Immediately, the main issue of scaling was evident, as the optical components are several orders of magnitude larger in volume than their electrical equivalents. Optical components were first specifically designed for use in the telecommunication marketplace, as a drastic increase in internet users occurred in the early 2000's [3]. An optical fiber communication system can propagate a signal for thousands of kilometers, conveniently fulfilling long-haul data transfer in a time where an unprecedented amount of information was being collected and transferred around the world. It was well understood that optical components possessed the potential to drastically change the digital

computing space, however, in the 2000's optical fiber communication was a lucrative market and Moore's Law had yet to reach stagnation.

In the 2010's it became increasingly evident that the evolution of electronic circuitry was reaching a plateau of scientific advancement. The introduction of full photonic integrated circuits (PICs) has developed around the potential of marketplace superiority and within the scope of next-generation technological opportunity. A single PIC can now be fabricated at the wafer-scale level, drastically reducing cost and size [3]. Several semiconductor platforms including Silicon-on-Insulator (SOI), SiN, InP and Silica have been fabricated as potential platforms for computing paradigm shifts. Each system utilizes light amplification by stimulated emission of radiation (laser), to package and unravel data at the beginning and end of an optical fiber. Within these on-chip systems there is immense complexity of design and optical manipulation, however, the laser requirement for operation is universal. As design improvements continue to develop and material science opportunities are concurrently examined, the objective of this work is to investigate opportunities to drastically decrease manufacturing costs of laser devices built for PICs.

Optical platforms will continue to evolve throughout the next several decades, and the importance of progressing the capabilities and manufacturing of laser systems is commercially critical. The optical platforms will require a series of interconnected laser outputs at micron level scaling, manufactured for low cost with robust repeatability. The exploration of imaginative manufacturing techniques is of high priority in preparation for the full transition to the next age of photonic integration. Selective area growth (SAG) is a technique that was developed for cost savings in semiconductor manufacturing, allowing for local area semiconductor growth manipulation. Using SAG, the manufacturing of laser devices can provide multiple distinct lasers

in a single growth process. This is paramount for high bandwidth operation providing multiple wavelength outputs for signal processing in an optical fiber.

1.2. Photonic Integrated Circuitry

The photonic integrated circuit industry is rapidly developing towards faster, more reliable, and cheaper methods for manufacturing at the device level. To achieve this goal, the introduction of selective area growth (SAG) or selective area epitaxy, based on the finding by Aoki, et al [4] can be modified for metal-organic chemical vapour deposition (MOCVD) mass production. SAG describes the process that involves outlining regions of a semiconductor with a mask of an amorphous layer, such as silicon dioxide. The chemical species impinging on the amorphous layer migrate to adjacent regions through surface diffusion processes due to a very low sticking coefficient, thereby increasing the flux in the vicinity of the mask edges, over a length scale of tens of microns. This growth feature results in the thickness of adjacent regions increasing in a controlled manner based on the surface area of the nearby masked regions.

A related effect is that the adsorbing species have different selectivity between the masked and unmasked regions. This also leads to compositional variations that are systematically related to the area of the nearby masked regions. This feature is the main parameter that will later control the laser emission wavelength, which is also a result of the bandgap of the material grown. The composition variation also directly controls the quantum confinement effects of individual, isolated laser structures. SAG can be used to grow local material variations with laser emission wavelengths that can be altered laterally across the wafer, as controlled by the masking structures which define the thickness of the quantum confinement cavity.

This project will seek to develop a robust SAG process, using the MOCVD at McMaster University's Centre of Emerging Device Technologies (CEDT), with the project collaboratively analyzed with ArtIC Photonics in Ottawa, Ontario. This project will investigate further development for MOCVD growth using AlGaInAs alloys with the SAG method. The objective of this project is to establish a repeatable growth process, calibrate growth mechanics by microscopy and photoluminescence testing and explore masking/growth alterations to increase yield, throughput, and device level control.

The first step in this development is the demonstration of lateral bandgap variations based on SAG growth, using InGaAs on GaAs. Once this process can be recreated fluently in our facility, AlGaInAs alloys on InP will be introduced because of their large conduction/valence band discontinuity split resulting in a high electron confinement which leads to improved gain, absorption, and thermal characteristics of components [5]. The structures will be assessed by photoluminescence (PL) measurements using a μ-PL apparatus and compared to theoretical expectations [6]. Material quality will also be assessed by X-ray diffraction (XRD) and scanning electron microscopy (SEM), as needed to evaluate suitability for device quality applications. ArtIC Photonics will be involved through all stages of the project, particularly sharing their expertise in advanced photonic device design and foundry processes. This project is a step in the right direction for Canada to continue to champion the telecommunications industry.

2. Literature Review

2.1. Semiconductor Heterostructures

Epitaxial deposition of semiconductor material has been critical for integrated circuitry development over the past half century. The control and mass deployment of epitaxial growth techniques has led to a plethora of pivotal advancements in nearly all engineering disciplines. The precision of semiconductor material growth has proven an integral part to the expansion of high quality electronic, optoelectronic, and photonic devices. The selectiveness of growth processing has often followed progress in maintaining Moore's Law, in which consistent miniaturization of feature sizes continues to be a topic of interest today.

The limitations of feature sizes became evident when quantum tunnelling and other quantum mechanical phenomenon destabilized the control of device performance. For example, when electrically controlled MOSFETs (metal-oxide semiconductor field effect transistors) reached single digit nanometer channel width, the voltage activated gate could no longer be controlled due to quantum tunnelling of charge carriers [7]. The importance of highly selective semiconductor growth can be extended to many engineering fields including electronic circuitry, third-generation photovoltaics, and photonic integrated circuitry.

The selectivity of growth mechanics is predominantly attributed to pre-processing techniques and growth parametric control. The pre-processing stage often includes a photolithographic pattern or mask to create growth cavities to inhibit or promote localized growth. The growth parametric control refers to controllable parameters such as elemental composition, deposition

time and substrate temperature. In this work, the history of development for selective area pre-processing techniques will be explored, including the encompassing general term of SAG.

SAG describes local growth control by pre-processed dielectric pattern masking on the surface of a semiconductor substrate. This local growth control can be utilized in a variety of deposition techniques including chemical vapour deposition (CVD), MOCVD and molecular beam epitaxy (MBE). The pre-growth process of dielectric masking has proven to be beneficial on a semiconductor substrate surface for device level uniformity and electrical discrimination [5]. Semiconductor growth techniques have significantly improved their parametric control throughout the past half century however - the ingenuity of device level engineering design lies within the pre-growth phase of semiconductor manufacturing processing.

To understand the history of development leading up to modern day photonic device growth, the basic model of the double heterostructure laser device will serve as a starting point on the roadmap to multi-quantum well lasers. The double heterostructure laser is the basis of solid-state physics operating by non-equilibrium carrier injection and impurity atoms [8]. A heterojunction defines a semiconductor contact of dissimilar materials which can create unique phenomena at the interface, often referred to as the junction. The main three phenomena that were outlined in the original heterostructure hypothesis of 1966 [9], are the superinjection of carriers, optical confinement, and electron confinement [8], demonstrated below in Figure 1.

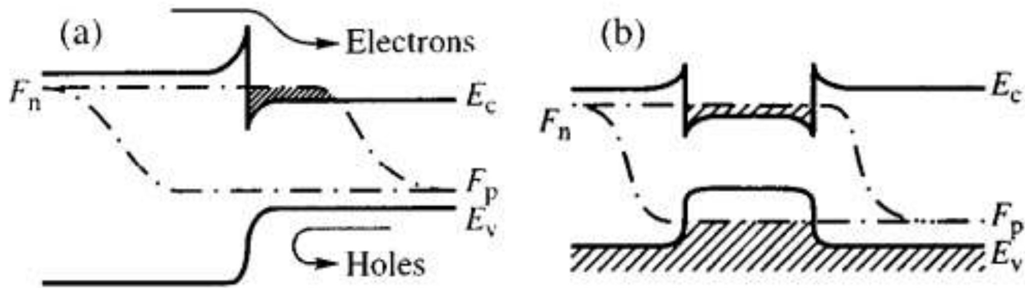

Figure 1: Superinjection of Carriers (a) and Electrical Confinement (b) [8]

The superinjection of carriers can be attributed to placing a dissimilar semiconductor between two semiconductors with wider bandgap energy and then applying a forward bias voltage [10]. The injection constitutes a significant increase in the concentration of electron and holes within the packaged central semiconductor. The process begins with the applied forward bias voltage which drives electrons into the central semiconductor where they ultimately recombine [11]. The conditions impose additional carriers to be collected until the number of carriers exceeds the doping density of the remaining semiconductor layer at the end of the forward bias. Superinjection is the fundamental basis of modern semiconductor lasers and light-emitting diodes.

Optical confinement is an imperative characteristic for a multitude of semiconductor devices including light-emitting diodes. Within the double heterostructure, complex differences in the indices of refraction between adjoining layers confines the optical field within the central layer. The confinement of optical emission prevents absorption of the emitted radiation by the materials surrounding the heterojunction. The material selection is paramount for device operation, requiring a balance between optical and electrical confinement, indicative of material properties.

Tuning heterojunction materials is an essential part of fabricating a functional and robust semiconductor device. The charge carrier confinement is made possible by differences in the bandgap energy of adjacent layers. The bandgap energy variance creates an inherent energy barrier that confines the charge carriers in the central region, often referred to as the active region. The bandgap of the semiconductor heterostructure is critical for the device emission wavelength defined in (1) below. The outer two semiconductor layers that surround the active region are commonly referred to as the cladding. The cladding functions as the basis of superinjection, confining forward biased charge carriers with a potential difference. The relationship between a three-layer slab heterostructure, for D, normalized thickness, is shown below in (2). The optical confinement factor Γ is a parameter to define the fraction of electromagnetic energy that exists within the active region (3).

$$\lambda = \frac{hc}{E_g} \quad (1)$$

$$D = \left(\frac{2\pi}{\lambda}\right) d\sqrt{{n_a}^2 - {n_c}^2} \quad (2)$$

$$\Gamma \approx \frac{D^2}{2 + D^2} \quad (3)$$

The hypothesis that once outlined the possibility of heterostructure potential carried skepticism around the feasibility of such a device. For functionality to exist there needed to be a small effective mass, wide bandgap energy, effective radiative recombination, sharp optical absorption edge and high carrier mobility. It was theorized that by manipulating GaAs-AlAs, materials with similar lattice constants, a heterojunction system could be developed [8]. Below in Figure 2, is a commonly used metric for defining lattice matching in semiconductor materials for the creation

of heterojunctions. GaAs-AlAs can be grown with high-quality crystallographic structure as a binary material system because of the lattice constant similarity. This similarity profoundly matched the necessary parameters of heterojunction creation, however, the entire functionality of a heterojunction was limited by the semiconductor growth process.

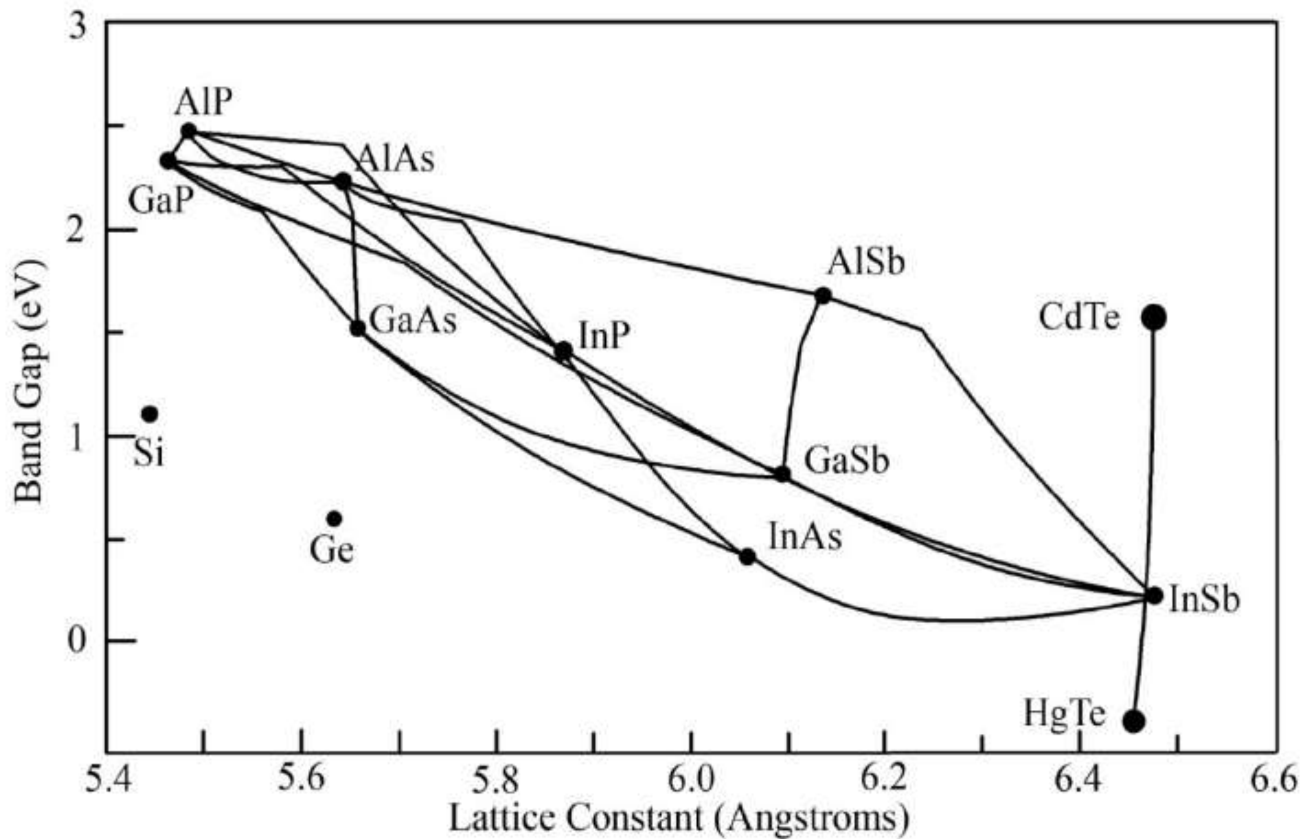

Figure 2: Lattice Parameters of Various Semiconductor Materials [12]

Vapour-phase epitaxy (VPE), the common semiconductor growth method of the time, could not stabilize the AlGaAs crystals [13]. It was clear that there was a requirement for a new type of growth process to stabilize III-V semiconductor compounds post-growth. Through a subtle alteration to solid solutions, the liquid-phase epitaxy (LPE) method was able to grow the first

AlGaAs crystals successfully [13]. With this discovery, semiconductor heterojunctions drastically evolved, creating low threshold double heterostructure (DHS) lasers [14], high effective DHS light-emitting diodes [15], heterojunction photovoltaic cells [16], heterostructure bipolar transistors [17], and p-n-p-n switching devices [18].

As development of new devices flourished in the 1970's, new methods of growth were required to fit the demands of new materials systems. An example of this is the introduction of InP, the most common substrate for fiber optical communication devices, with emission in the infrared region, the region of lowest attenuation in fiber transfer. The necessity to explore more precise growth techniques became additionally apparent when layer thickness limitations for device improvement and miniaturization were not met with traditional VPE or LPE techniques. The creation of MBE and metal-organic vapour-phase epitaxy (MOVPE) provided the imperative precision of monitoring thickness, planarity, and composition [19].

MBE utilizes an ultra-high vacuum chamber in which a processed beam of atoms or molecules are directed upon a heated crystal [20]. In Figure 3 below, the front view of an MBE growth chamber is shown. To begin the process, the substrate is placed on a heating block facing a series of source ovens used to evaporate the constituent atoms or molecules [20]. The relative temperature difference between the substrate and the side walls of the chamber limits the molecular beam to a single pass, through promoting condensation on the sidewalls. This structure preserves the purity of the film and ensures that the reflection high-energy electron diffraction (RHEED) gun does not cross path with residual vapours. The RHEED provides a diffraction pattern on a phosphor-coated window that is indicative of the ordering of the substrate surface [20].

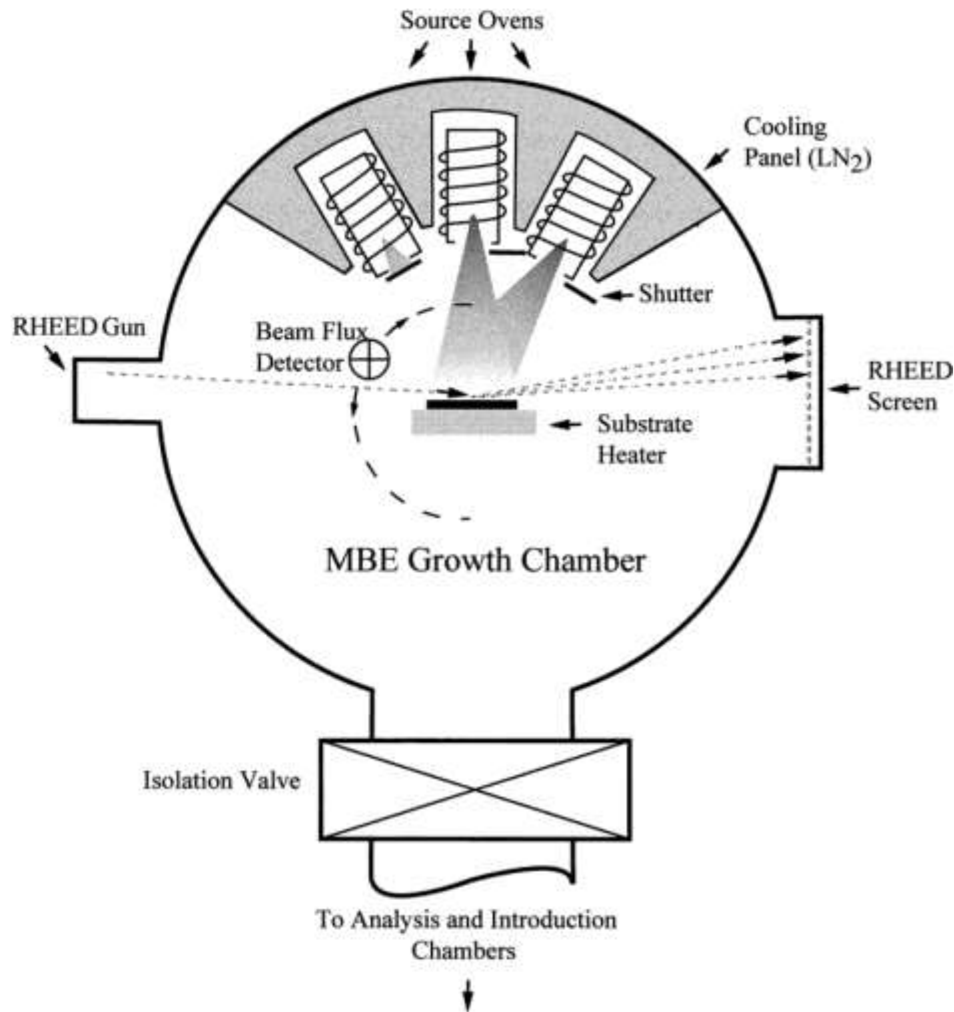

Figure 3: MBE Growth Chamber Schematic [20]

The precision of the MBE system is unmatched in semiconductor growth processing with the ability to create interfaces that are atomically abrupt. The MBE process is designed for growing thin epitaxial films which can be grown sequentially to create devices such as quantum-well lasers or superlattice devices. The issue with the mass production utilization of MBE is the cost of control, demanding atomic precision with near idealized models of growth [20]. MBE is currently employed primarily in various industrial and academic research laboratories to explore fundamental principles of solid-state physics. The MBE mechanism exists principally as an

investigative tool for the future of solid-state physics and the theoretical understanding of thin film growth. The main industrial manufacturing limitation of MBE is the lower throughput compared to MOVPE.

An additional semiconductor growth mechanism that can create high performance electronic and optoelectronic devices is MOVPE. This process involves the operation of metal alkyls as the compound source which travel to a reaction chamber alongside hydride compounds. Through a process called pyrolysis, organometallics and hydrides can recombine as atomic or molecular species at the surface. Each material can be controlled with partial pressures via electronic mass flow controllers to create percentage variations of semiconductor material combinations. Below in Figure 4, a common MOVPE chamber schematic map is shown [21].

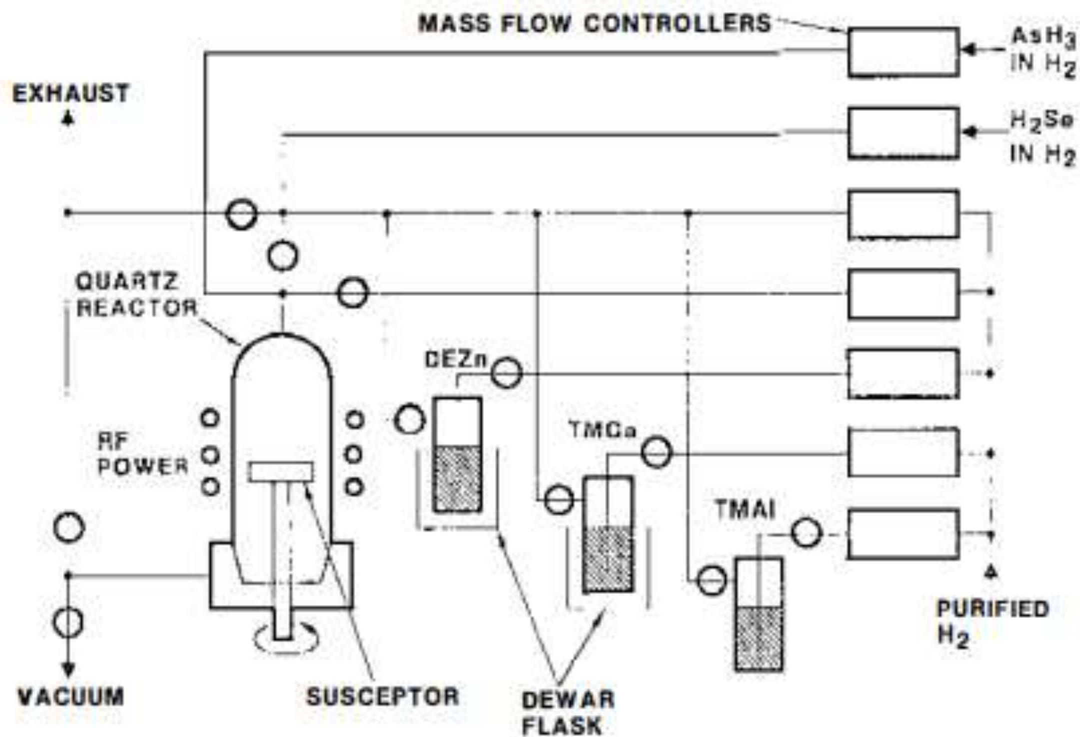

Figure 4: MOVPE System Schematic [21]

In the early stages of development, MOVPE demonstrated the ability to work with a wide variety of compound semiconductors including group III-V, II-VI and IV-VI [21]. It was realized that this process can lead to high throughput and is ideally suited for switching between many epitaxial layers, an inherent characteristic of modern device structures. MOCVD is the overarching technique that MOVPE falls under, which specifically refers to the use of metal alkyls for the compound source.

The limitations of VPE led to the saturation of device level design which severely limited the ability to test solid-state theory and semiconductor device control. With the introduction of advanced growth techniques such as MOCVD and MBE, quantum mechanical attributes were unlocked, including creating devices with single atomic layer capabilities. The past several decades has seen growth techniques simultaneously expand and evolve with the quantum mechanical possibilities. The MBE system can identify experimental and fundamental limitations while also exploring unique material and device prospects. The MOCVD system can provide necessary throughput for commercial scale functionality, delivering high performance electronics to everyday consumers.

Semiconductor compound growth on the monoatomic level generated an abundance of state-of-the-art quantum devices. The distinct manifestation of quantum-well effects in optical spectra of GaAs-AlGaAs semiconductor heterostructures with an ultrathin GaAs layer was first demonstrated in 1974 [22]. This advanced laser system is made possible by the thin layer control of MBE or MOCVD, which allows for single digit nanometer optimization. At this scale of layer thickness, quantum confinement will occur in an ordinary double heterostructure. This led to improvements in the ability to produce shorter emission wavelengths, lower threshold current and higher differential gain [8]. The main advantage of the quantum-well laser device over the

standard double heterostructure is the noticeable increased density of states with reducing of the dimensionalities of electron gas [8].

An example of a quantum-well laser device is shown below in Figures 5 and 6, including the characteristic confinement of the charge carriers. The density of states theory was formulated to understand the proportion of states that are occupied by the system at a specific energy, see Appendix A. Each discrete step occurs when a new subband energy level is reached confining electron density to those energy levels. The benefit of this energy state discretization is a lower threshold current, higher quantum efficiency and higher modulation control [23].

The quantum-well laser exists as a series of semiconductor layers assembled on-top of one another. The functionality of the laser device is dependent on the thinnest layer, the quantum confinement layer, in which charge carriers are confined to a 2-dimensional space. The layer is 3-dimensional grown (<10 nm) however, the electrons are confined to a 2-dimensional plane as the density of states is altered at this thickness range. This confinement inhibits charge carriers from leaving the cavity until they achieve sufficient energy to overcome the potential energy barrier. This allows for discontinuity in the density of states which promotes the charge carriers to form population inversion. The semiconductors that construct the quantum-well laser are immensely dependent on the thickness of the quantum confinement layer. This active layer is a minuscule proportion of total device thickness, however, this thin layer is pivotal for device performance.

In Figure 6, the sapphire substrate is first covered with a GaN buffer layer which will create a foundation for the next growth layer. The defects of the sapphire substrate lattice can be covered with sufficient GaN thickness while simultaneously introducing a lattice parameter matching material for the adjacent top layer. The n-doped AlGaN layer creates the first section for adjacent

quantum confinement discretization. The main objective of the discretization of pn-junction formation (DHS) is higher quantum efficiency within the cavity. The adjacent layer is a similar n-doped AlGaN semiconductor layer however, this AlGaN layer will have a lower bandgap energy controlled by compositional alterations. The quantum layer is placed between the p-doped surface layer and the n-doped transition layer beneath, creating a quantum-well cavity by packaging InGaN with GaN cladding. Placed above the p-doped AlGaN layer is a capping layer of p-doped AlGaN, with a higher bandgap energy. This structure energetically is demonstrated in Figure 5 below. The discretization of bandgap energy as a staircase is showcased as a light guided structure with a multi-QW (MQW) output wavelength of 413 nm.

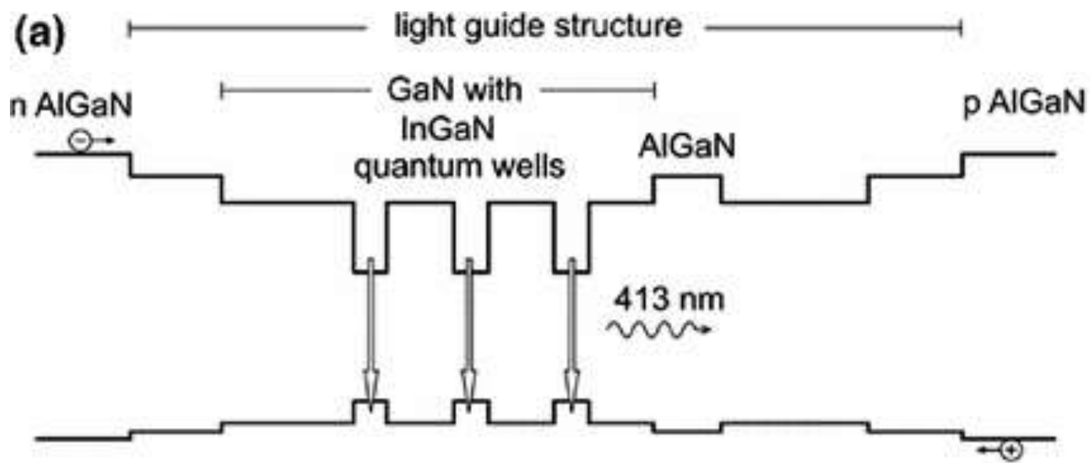

Figure 5: Basic Quantum-Well Energy Band Structure [24]

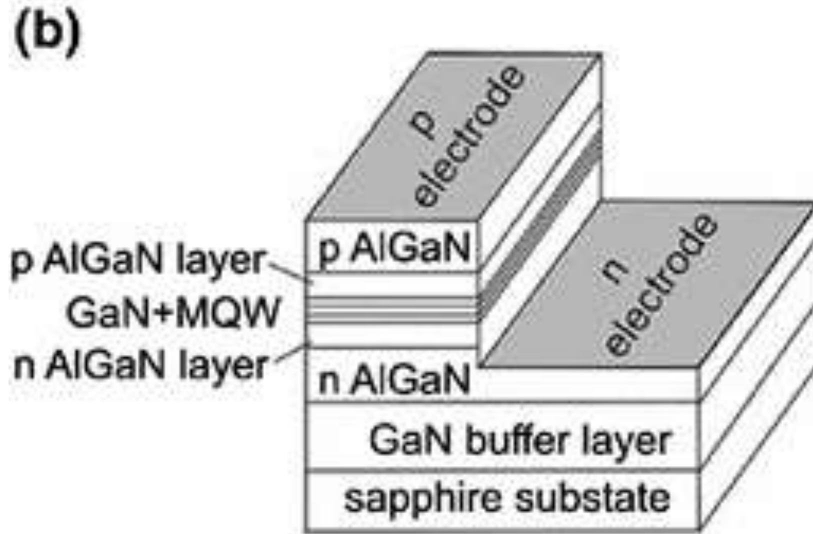

Figure 6: Layer Schematic of GaN Quantum-Well Laser [24]

In summary, the theorization of quantum-well double heterostructures was realized through the enhancement of semiconductor growth techniques. The ability to create precise semiconductor material layers legitimized theories of quantum mechanical properties. The quantum confinement of charge carriers has led to the rapid development of modern-day optoelectronics, driving the telecommunications industry. The process development of the quantum-well laser continues today with new materials and finer modulation while tuning parametric growth control. The pre-growth technique propelling the industry towards the vital mastery of semiconductor deposition is SAG.

2.2. Selective Area Growth

The first evidence of selective area semiconductor growth is attributed to the deposition of GaAs into pre-growth processed surface cavities on a GaAs substrate [25]. The mass adoption of lithographic and etching methods in the semiconductor manufacturing sector closely followed the development of early modern functional growth techniques including CVD. The ability to

manipulate chemical etching methodology provided the revolutionary process of semiconductor growth layout control. The layout control of semiconductor growth processes allowed for a single growth procedure to create multiple devices repeated, either identical or dissimilar on the same surface of a semiconductor wafer.

By the 1990's the epitaxial growth process was predominately managed by lithographic and etching mechanics post-growth [26]. This method defined the structures both laterally and longitudinally in the growth plane, however - as this technique matured the pre-growth dielectric masking began to evolve [26]. It was discovered in 1991, that by utilizing the dielectric pre-growth masking, users were provided the ability to control diffusion of reactant species from a nongrowth surface to a growth surface. Through gas phase partial pressure modulation, the growth rate of selected species can be controlled simultaneously. The magnitude of this effect with MOCVD is well-suited for growing structures in 3-dimensions [26]. It was first theorized that pre-growth masking accompanying semiconductor material compositional control could create multiple quantum-well devices in a single growth process [26].

In 1991, the identification of pre-growth dielectric masking become a prevalent device fabrication topic, leading to the first demonstrated device by MOCVD SAG in that same year. A novel MQW electroabsorption modulator was grown beside a distributed feedback laser (DFB) in the same MOCVD process [4]. The precision of MOCVD combined with the tuning possibilities of SAG created a MQW structure with bandgap energy control and discrimination. The photoluminescence of this MQW structure demonstrated a variation of 130 nm from the same MOCVD occurrence [4,27]. This device fabrication dramatically altered the landscape of pre-growth manufacturing of MQW devices, providing a fundamental new field of epitaxial opportunity.

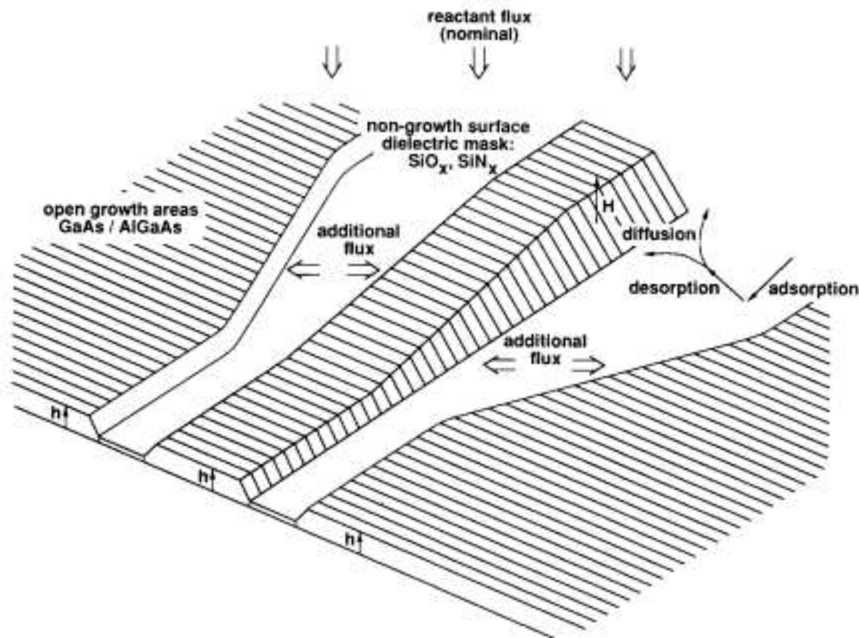

Figure 7: SAG Schematic [26]

Advancement in the field of SAG continued with novel semiconductor materials including III-V InP MQW lasers [28]. The technological shift towards a photonic integrated future revolved around the telecommunications industry of the 1990's. The driving force behind the development of SAG was the commercialization of optical fiber communication. The magnitude of the optical fiber industry was universally understood, as revolutionary progress into the internet age of digital computation was prevalent. The real benefit for SAG is the requirement of nearly all semiconductor devices to be grown epitaxially. This requirement in tandem with that of a pre-requisite laser device needed for optical fiber transmission has guided SAG to the mass production scale.

In principle, monolithic fabrication techniques involved several regrowth procedures in which MOCVD was utilized in between lithographic etching procedures [4,28]. SAG seeks to offer

identical results to a multiple growth procedure with the MOCVD system only required to be activated once. A decrease in the number of MOCVD stages will decrease the overall cost of manufacturing. Initiating epitaxial growth onto a patterned dielectric mask while concurrently controlling the growth rate and composition of the epilayers will lead to selective area reactant flux variations [28]. The specific patterned growth regions can be altered for additional flux by increasing the width of the non-growth masking regions. This alteration in the flux density will change a quantum-well layer thickness leading to unique wavelength emission spectra.

The quantum-well thickness variation is the critical piece of fabrication leading to a higher bandwidth of laser emission. The third technique that has been explored is quantum-well intermixing, a post-growth slicing procedure that attempts to create distinct laser devices [28]. To intermix quantum-well lasers, crystal damaging is required in the structure after the growth process is completed. The intermixing damage creates a shape modification that alters the quantization energies of carriers within the active layer. This technique can lead to increased transitional energies to several hundred meV [28].

The principal issue for the use of SAG and quantum-well intermixing is the limitations that arise when deploying either technique for an array of devices; it becomes increasingly difficult to optimize at the single device level. A critical trade-off exists between optimizing for throughput and quality control of individual device level performance. In this specific investigation, the SAG technique will continue as the focus of pre-growth epitaxial design however, it is now clear that progress in this field has become equal part art and science.

In 1997, the process flow of utilizing selective growth patterning continued with buried heterostructure techniques which involve more than one MOCVD growth [29]. This technique involves multiple SAG stages, creating buried structures that will act as enclosed quantum-well

lasers. This technique encompasses both the SAG patterning and selective area regrowth method and is ironically renamed as SAG. A buried heterostructure is desirable because of the strong index guiding and current confinement provided by the heterostructure discontinuity in the lateral direction [29]. Multiple MOCVD processes with SAG designs at each stage will not defeat the purpose of SAG, rather, it amplifies the complexity of design. By incorporating a unique design for non-growth masking at each stage, the multiple growth process can further increase the number of unique devices [30].

Intricate semiconductor material systems developed alongside MOCVD improvements throughout the 2000's, leading to the AlGaInAs alloys that will later be utilized in this work. MQW structures can provide lower threshold current, while applying the Stark quantum confined effect, see Appendix B. The AlGaInAs material system has a growing industrial importance because of a large conduction/valence band discontinuity split ($\triangle E_c/\triangle E_g \approx 0.7$), resulting in a high electron confinement [5]. A higher degree of electron confinement will result in a device with improved gain, absorption, and dynamic and thermal characteristics of components [5]. Dupuis et al [5], have outlined the parameters required to successfully create a MQW selectively grown array deploying AlGaInAs alloys.

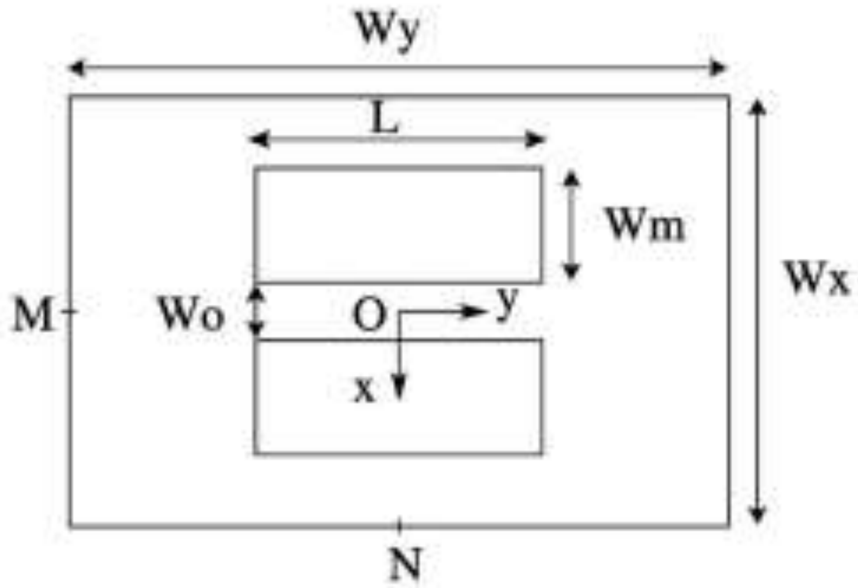

Figure 8: SAG Mask Structure [5]

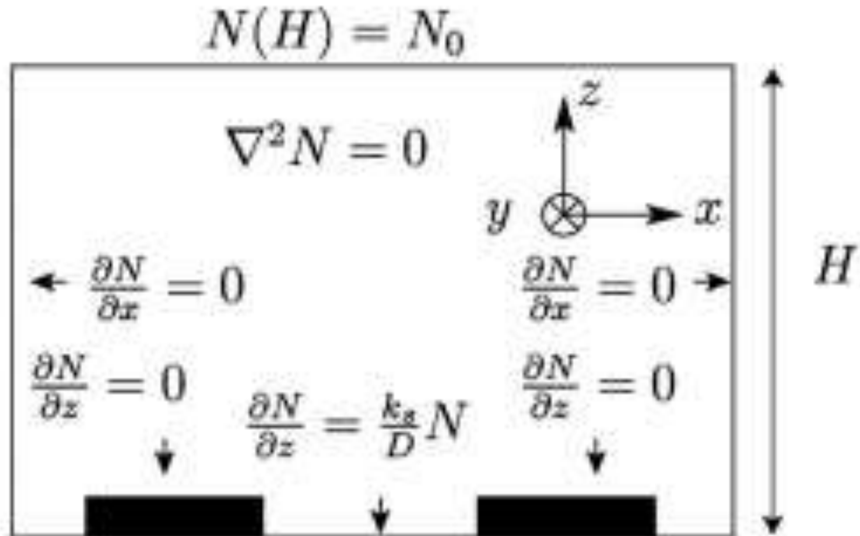

Figure 9: Simulation Setup for SAG Mask Design [5]

It was determined that the material properties directly influenced the ability to selectively grow in specific cavities based on the diffusion length of each material [5]. The diffusion length can be determined by a Langmuir isotherm condition, to determine D, the diffusion coefficient of the reactants in the vapour phase and k_s, a sticking rate constant which depends on the reactivity of source materials [5]. Using a fast Fourier transform (FFT) method, the parameters for each compound can be determined equal to $(D/k_s)_{Al}$, $(D/k_s)_{Ga}$ and $(D/k_s)_{In}$. This model solidifies the width/surface area of the masking structures for growth thickness enhancement by SAG. The diffusions lengths were determined to be 50 μm, 85 μm and 10 μm for Al, Ga and In, respectively [5].

$$D(\frac{\partial N}{\partial Z})_{z=0} = k_s N \quad (4)$$

Provided the diffusions lengths for alloys pertaining to AlGaInAs, the W_o, the width of the cavity can be parametrically evaluated with W_m and L, the width and length of the mask structure. The main concern for mask design is the limitations that arise from the 10 μm In diffusion length. The In species, which has the shortest effective diffusion length, highly enriches in the near vicinity of the mask while Al and Ga, have an influence which extends further from the mask edge [5]. The W_m parameter's effect can be limited by increasing the mask width beyond the threshold of the largest diffusion length ($W_m > D/k_s$), thus, the dependency on the W_o will become more significant for growth control.

SAG mask exploration has been expanded to a model of computational simulation which is then confirmed after MOCVD with post-processing calibration techniques for thickness variation. Debrégeas et al [31], utilized optical interferometry to understand individual layer thicknesses for SAG masking calibration. The masking width (W_m) was evaluated from 20 μm to 100 μm

with a width opening (W_o) of 20 µm to 40 µm [31]. If each growth material has a unique dependency to diffusion, the cavity of growth will possess a non-uniform growth composition from one mask edge to the center of the cavity. The non-uniformity is an additional parameter to consider for bandgap engineering modifications, to ultimately change the photoluminescence emission of the well.

An enrichment of In is obtained in the vicinity of the mask edge induces a lattice mismatch of the AlGaInAs material compared to the InP substrate. This process can lead to a compressive strain in the grown layer [32]. While growing thicker layers, the strain can concentrate, and misfit dislocations can occur in the material [33]. During SAG both the growth enhancement and the In enrichment are higher in the vicinity of the mask, resulting in a larger compressive strain. If crystallographic defects are formed at the edges of the SAG mask, they can propagate through the whole active material between the two mask stripes [32]. To compensate for this issue, calibration is needed for compositional control during MOCVD. With compositional control, the In species can be layered with pre-determined strain modifications to avoid drastic crystallographic defects. By imposing a stepwise function of increasing or decreasing strain values to accommodate strain changes in the lattice, the crystallographic matching can be resolved over several layers.

Décobert et al [32], was able to showcase the SAG dependency of µ-PL over a range of 0 µm to 35 µm for the mask width and a set 20 µm width opening. An increasing SAG mask width will increase the emission wavelength of the grown structure by altering the internal composition. In this case, a larger mask width will lead to a lower In content in the cavity, raising the bandgap energy, thus increasing the output wavelength. The average photoluminescence wavelength range extends over 203 nm (1449 nm to 1652 nm).

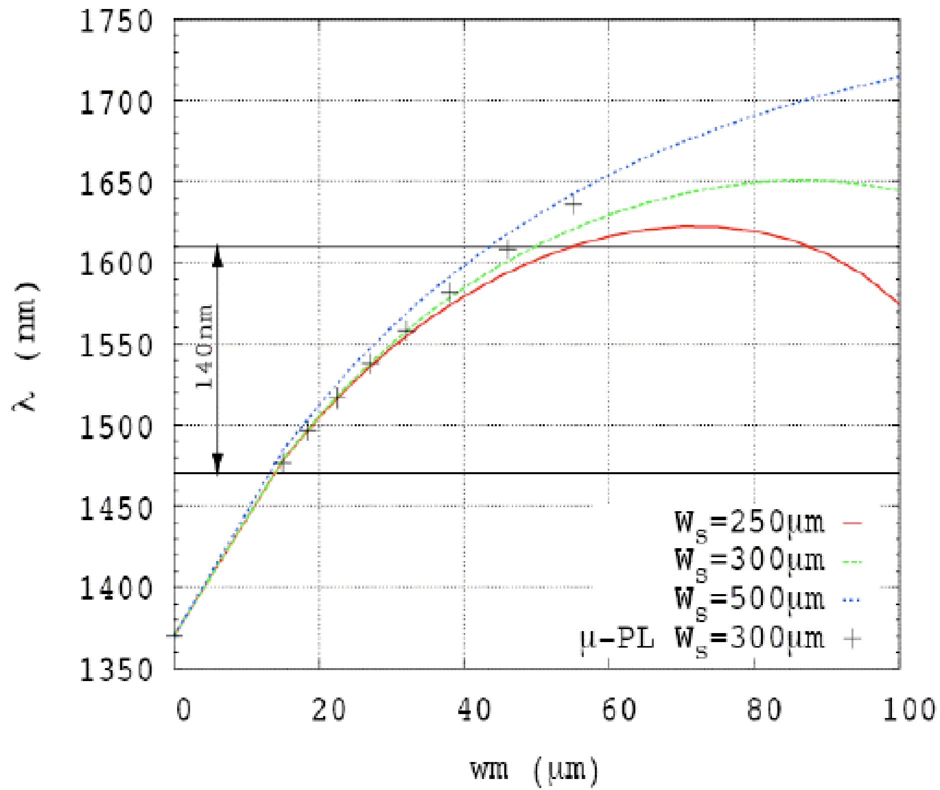

Figure 10: SAG Mask Thickness Compared to Emission Wavelength of Quantum-Well Lasers [32]

In summary, the SAG masking design has been thoroughly simulated for parametric analysis of masking and cavity width to determine growth dependency. The SAG mask design is commonly dependent on the growth materials, growth temperature and the partial pressures leading to the compositional variations of the grown layers. It was demonstrated that changing the mask width and the cavity width will alter the photoluminescence of the grown MQW structure. With this knowledge, the definition of a large area rapid prototype mask can be developed for laser direct writing that will contain both transitional ranges for mask width and cavity width. This will allow for a significant number of structures to be grown in a single MOCVD growth process, with an immense number of mask and cavity width variability.

The fundamental basis of SAG will be explored in this work to quantitatively justify parametric control with the MOCVD at McMaster University. Utilizing SAG is not necessarily a new technique in MOCVD, however, the advancement for mass production purposes pertaining to embedded complex PICs is a recent topic of interest. This work will define the foundation for a multi-purpose, research MOCVD system, defining system level parametric control. Concurrently, the process of fine-tuning the direct laser writing procedure, post-imaging/calibration/characterization techniques and μ-PL will be prepared for implementation at McMaster University for the current and future use of MOCVD with SAG.

3. Experimental Procedure

3.1. Semiconductor Wafer Processing

The semiconductor wafer of choice must be patterned using SAG to successfully grow a responsive active quantum-well laser created by MOCVD. During this investigation both GaAs and InP wafers were patterned with a recipe that was consistently adapted for discrepancies that arose from the direct laser pattern writing. Due to the lengthy delays between laser operation, there was a necessity to alter the recipe for full original functionality of photoresist development. The current recipe will be explained in this section and the importance of each stage of the process will be outlined.

The mechanism of SAG is activated by top surface patterning of an amorphous layer. In nearly all examples of selective area growth, silicon dioxide is deployed, also commonly referred to as silica. Silica can be deposited onto the surface of both GaAs and InP directly. The amorphous layer's deposition onto the surface of a semiconductor wafer functions as a growth barrier during MOCVD. This process is made possible by silica's very low sticking coefficient relative to the MOCVD elements that will be employed in this investigation including In, P, Ga, As and Al. The semiconductor manufacturing process flow was designed around GaAs 100 ± 0.1° Si doped, n-type, single side polished, 350 ± 25 μm wafers. This selection was in collaboration with Dr. Ryan Lewis and MOCVD Research Engineer Dr. Manu Hegde, to optimize MOCVD growth conditions which could be controlled. The process began with the deposition of silica onto the surface of a GaAs wafer by CVD.

The Technics Micro-PD CVD chamber was utilized as a silicon oxynitride deposition chamber for the amorphous layer. A CVD chamber surface plate was heated to 300°C on which the GaAs substrate was placed. The silica amorphous layer can be grown by deploying precursor gases of silane (SiH_4) and nitrous oxide (N_20), leading to silica (SiO_2) deposition. The process flow is shown below in Figure 11.

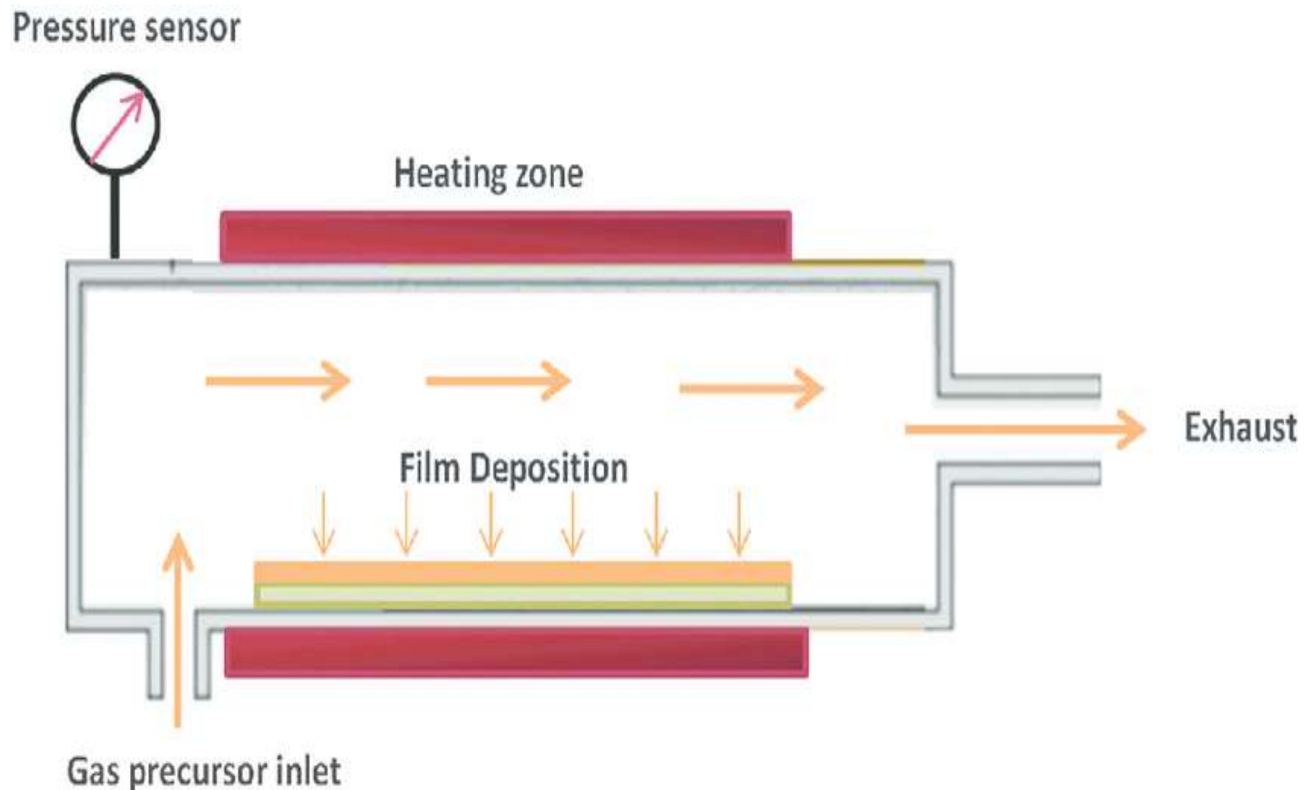

Figure 11: Basic Schematic of CVD Reaction Chamber [34]

The precursor gases are activated by a filament to create a plasma cloud that dissociates to form a solid coating on a heated substrate. The vacuum sealed reaction chamber sample holder is perpendicular to the process gas flow, allowing for a consistent electronic mass flow-controlled deposition rate.

As outlined above, the thickness of the amorphous layer is critical for selectivity during MOCVD. Ideally, the thickness of amorphous layer should match the thickness of the quantum-well laser device however, issues could arise with the elements sliding down the side walls for several microns into the cavity. Additionally, the amorphous layer was limited to 1 micron of deposition per chamber cleaning cycle, elevating the deposition timeline to several days. It has been demonstrated that SAG is possible with a significantly thinner amorphous layer relative to the MOCVD total growth thickness [35]. This is made possible by the lattice parameter matching of the compound semiconductors, creating a well matched, low defect crystallographic structure, able to grow upwards within the cavity beyond the amorphous layer.

The silica layer's thickness is first confirmed with the use of ellipsometry, and a tolerance of 100 ± 5 nm was selected. This tolerance was determined by averaging the CVD growth thickness error for five silica 100 nm layers grown under the exact same conditions and exposure time. The ellipsometry measurements were additionally confirmed with the use of a profilometer however, due to the immense thickness difference between the silica and quantum-well laser device, the 5 nm error was determined to be sufficient through ellipsometry measurements exclusively. It should be noted that the surface area of the silica structures is the most important characteristic, and this tolerance simply exists to create consistency in future growth mechanics.

To control the MOCVD, the silica layer must be patterned in a predefined, purposeful series of isolated structures that will act as non-growth centers. A patterning mechanism for silica is the utilization of photosensitive layers that can be exposed and developed, leaving behind a 3-dimensional etching channel. The surface of the substrate is first cleaned by acetone, to remove oils and organic residue. The residue left behind by acetone cleaning is further removed by isopropyl alcohol, leaving a clean wafer surface for spin coating. MPHP (hexamethyldisilazane)

primer is spin coated to provide an inert foundation for S1808 photoresist placement. Each solution is spun for 30 seconds at 4000 RPM, thus leaving an 800 nm thin film of photoresist uniformly distributed across the surface of the substrate. The precision of this film thickness is based on supplier recommendations and is not explicitly confirmed however, laser exposure power can be calibrated according to photoresist thickness.

Deployment of S1808 can be credited to its relative low cost and availability as a positive photoresist. A positive photoresist when exposed, becomes soluble to the photoresist developer. This leads to the subsequent removal of the exposed regions of photoresist in the development process. Before patterning the photoresist, a hot plate was utilized to heat the substrate to 110°C for 90 seconds to drive off solvents and solidify the film. The cleanroom at the CEDT possesses orange lighting to ensure that the photochemical reaction does not occur by UV exposure. The sample is now ready for pattern generation by direct laser writing and is transported within aluminum foil to protect the thin film from contamination and possible exposure.

The Heidelberg µPG 101 (micro-pattern generator) can expose photosensitive material using a 375 nm UV laser with customizable power (up to 70 mW), duty cycle and optical filtering/focusing. This laser system can create unique patterns sourced by crystallographic information files (CIF) that determine exact laser exposure positions based on a calibrated grid formation. By deploying a unique raster scanning module, exceptionally accurate patterns can be created with precision on the order of single digit microns. The system provides mask-less patterning for rapid prototyping, increased security of design and reduced cycle times. Ultimately, this device is designed to eliminate the necessity to produce photolithographic masks in the development process. The pattern manipulated for the structures is shown below in Figure

12, The ingenuity of the laser pattern direct writer has revolutionized the pace of photolithographic patterning including the use of silica masks in MBE or MOCVD processes.

The generated pattern shown in Figure 12, is setup parametrically for a consistent mask length of 175 µm, stepping through mask widths of 20 µm, 40 µm, 60 µm and 80 µm with cavity widths of 20 µm, 30 µm, 40 µm and 50 µm.

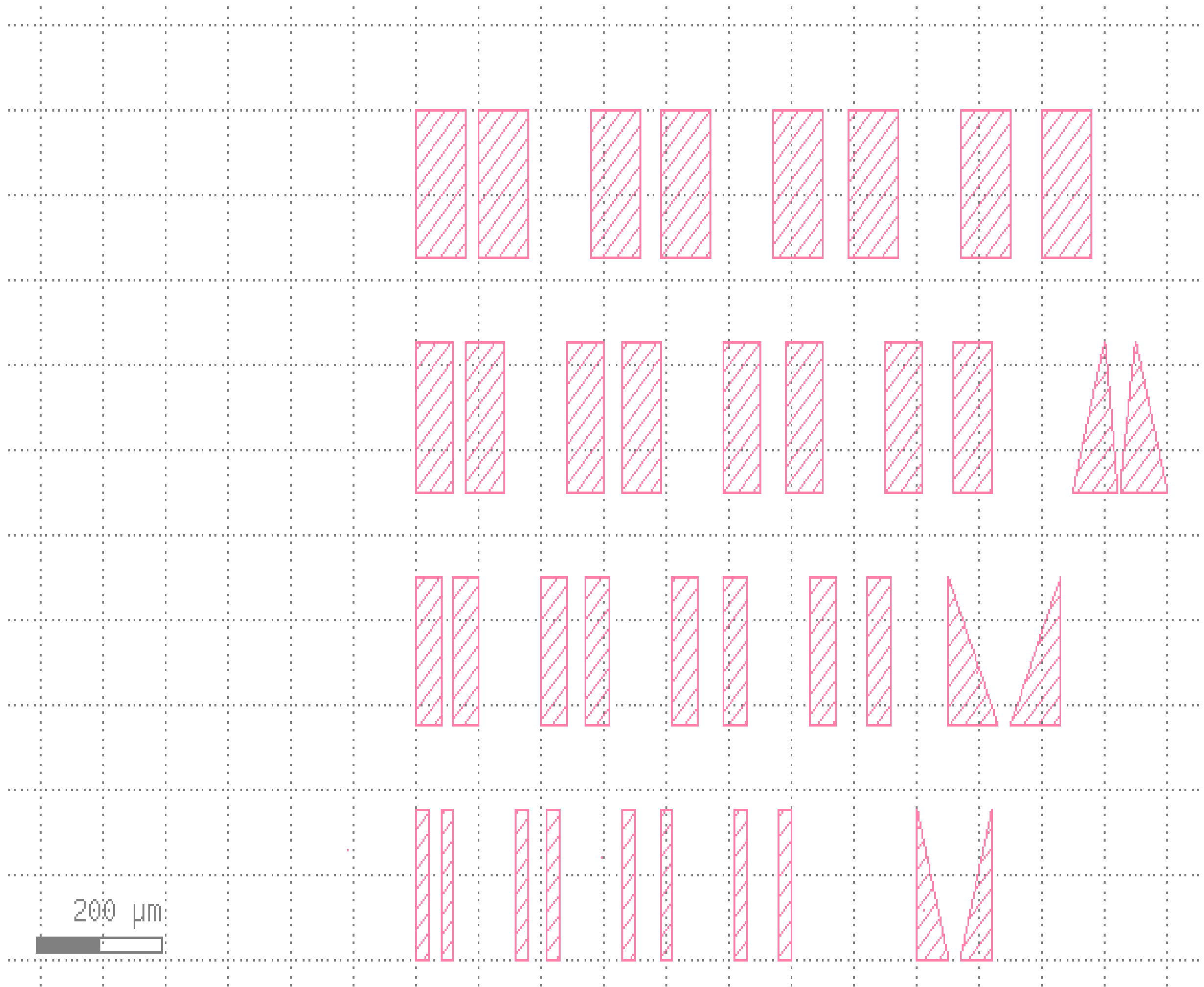

Figure 12: CIF File for Masking Design

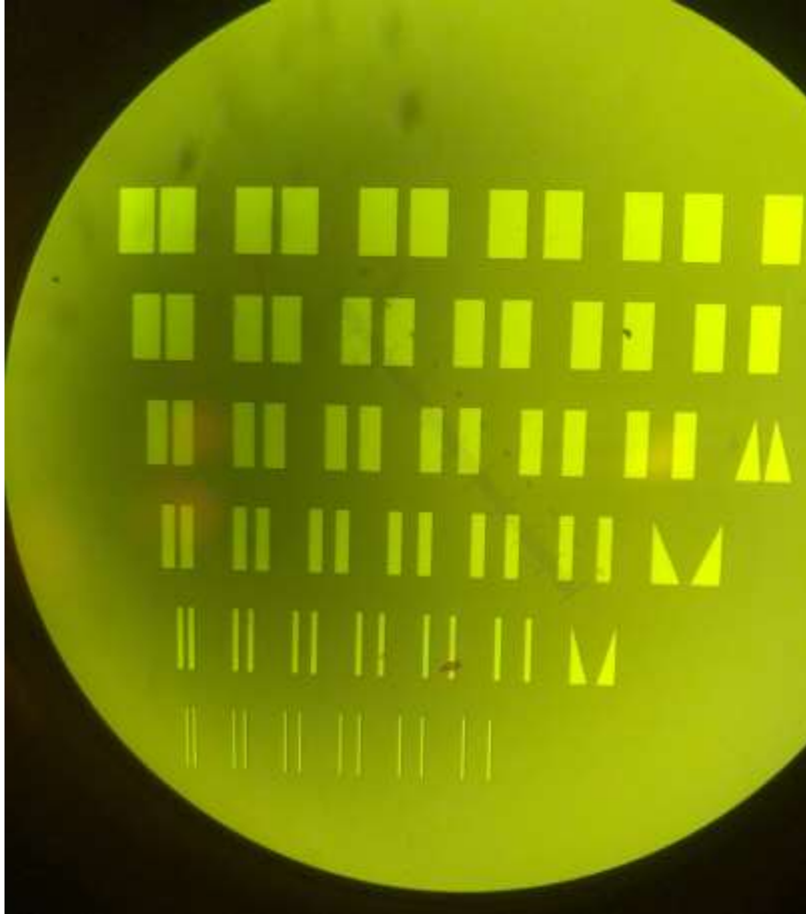

Figure 13: Optical Microscopy Image of Mask Design During Photolithographic Processing

The laser direct writer is first calibrated by mapping the edges of the sample of interest for optimizing pattern writing position. Once the center and edges of the sample have been located, the pattern can be exposed onto the thin film. By collaborative CEDT optimization, the S1808 resist is exposed at 11 mW with a 60% duty cycle while deploying write mode III. Write mode III offers 2.5 μm feature sizing and a write speed of 35 $mm^2/minute$. The total write time for a full sample exposure is approximately 40 minutes. Write mode I in comparison is roughly four times more precise (0.9 μm) however, it can take nearly seven times longer (5 $mm^2/minute$). For the purposes of our structures, it was determined that write mode III was sufficient for the feature sizing and abrupt right-angled corners of the prisms.

When the direct writing is completed, a secondary bake (110°C for 90 seconds) is used to improve surface adhesion. The sample is then developed by dipping the wafer into MF319 photoresist developer solution. Development may take several minutes leading to the positive photoresist, that was exposed, to be completely removed from the surface. At this stage the wafer surface is patterned, leaving behind a protection layer of photoresist with rectangular prism cutouts. Each rectangular prism is designed for a specific position during the MOCVD process and will now act as an etching channel to create the laser cavity.

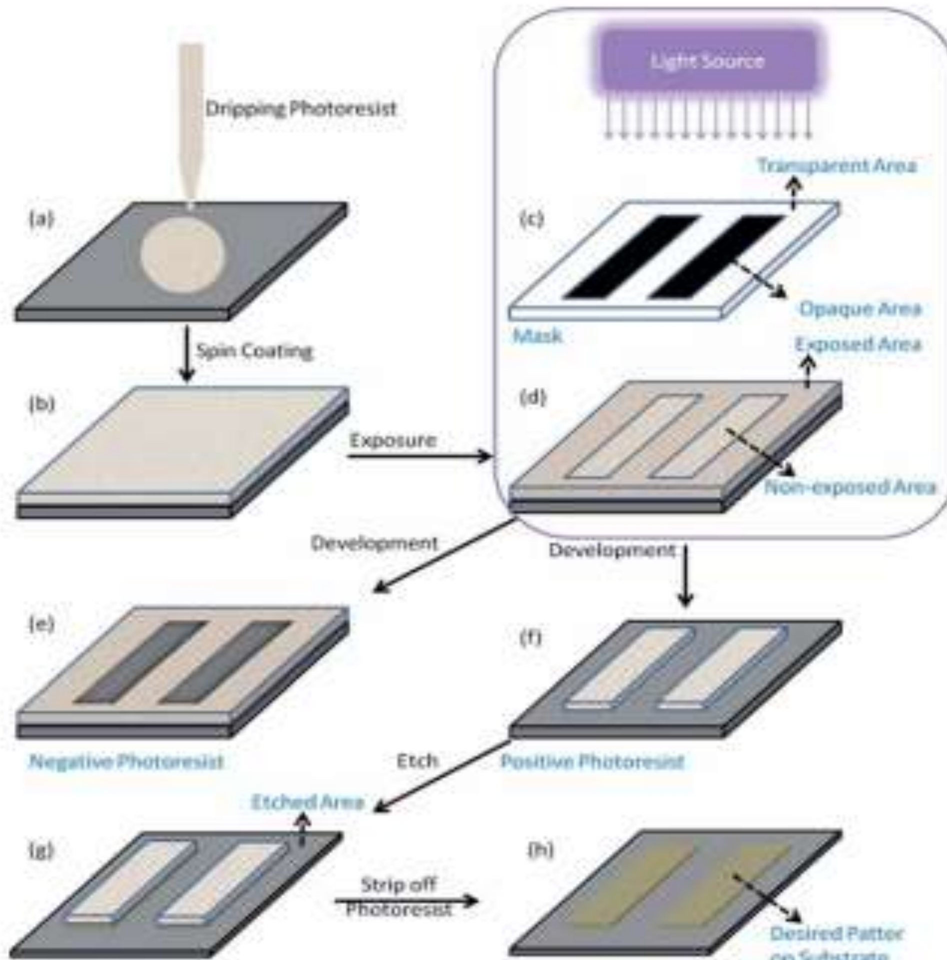

Figure 14: Photolithographic Processing Procedure [36]

Prior to the chemical etch a tertiary bake, referred to as the hard bake, is used to stabilize the remaining photoresist. The hard bake (130°C for 90 seconds) removes any excess solvents while also improving the resistance of the photoresist to the chemical wet etching. Using hydrofluoric acid with an ammonium fluoride (NH_4F) agent (to increase surface etching uniformity), the silica layer beneath the photoresist can be removed exclusively in the positions in which the photoresist had previously been exposed, developed, and removed. The silica etching process is completed in a consistent timed procedure (90 seconds), to ensure that over-etching does not occur. An over-etched silica mask can lead to altering of the silica uniformity (thickness), by etching beneath the photoresist protective layer. To expose the silica structures the photoresist layer is then removed using an acetone bath.

In summary, this procedure leads to the formation of rectangular prisms of silica on the surface of GaAs or InP wafers. The dimensions of the silica in the 2-dimensional plane parallel to the wafer surface were previously demonstrated [35]. This method has provided highly selective masking regions by virtue of direct laser writing precision. The sample is now ready for MOCVD, including the selective growth contribution of the 3-dimensional deployment of silica non-growth centers strategically located across the substrate’s surface. Lastly, the sample is packaged in protective wrapping for transport to the Tandem Accelerator Facility in which the MOCVD is located.

3.2. Metal-Organic Chemical Vapour Deposition (MOCVD)

At the Tandem Accelerator Building at McMaster University there exists a MOCVD machine empowering semiconductor manufacturing research and development. This system grants industrial level throughput and a high standard of quality control mimicking the large-scale semiconductor manufacturing standard operating procedure. During January 2020, the MOCVD

system became operational under Research Engineer Dr. Manu Hegde. The system is a series of complex interconnected instruments leading to a final deposition chamber originally designed and built by SMI, Inc., with specifications provided by Dr. Shahram Ghanad-Tavakoli. Initial operation was completed as a collaborative effort between Dr. Hegde and I, with confirmation by Dr. Ryan Lewis, Dr. Rafael Kleiman and Spencer McDermott. This effort led to autonomous control by Dr. Hegde in Spring 2020 and has developed with additional elements and process techniques made available to research groups throughout the faculty.

The MOCVD system is a marvel of manufacturing engineering leading to the rapid deployment of deposition for thin film layers onto semiconductor substrates. The MOCVD system is commonly utilized to manufacture light-emitting diodes, laser diodes, photovoltaic cells, and photodetectors. The MOCVD mechanism is a staple of optoelectronics in both the research sector as well as the mass production manufacturing process. At the research level, the capabilities of the MOCVD are constantly tested for industrial processing improvement while exploring and defining benchmark process requirements and possibilities. To achieve a high degree of purity, control, and consistency in semiconductor growth, the MOCVD process has been designed with decades of improvements to the process flow.

MOCVD utilizes metalorganic compounds for one or more of the precursor gases leading to alternative names such as OM (Organometallic) CVD, MOVPE (Vapour phase epitaxy) and OMVPE. Each name defines the exact same process except when labeled exclusively as epitaxy, which refers more generally to a special case of thin film deposition where the layer replicates the crystal structure of the host substrate [37]. The industry standardization of MOCVD and the development that has followed, has led to increased uniformities, a wider variety of materials and unlocked bandgap engineering opportunities. The process has allowed for nearly all III-V and II-

VI semiconductors and their alloys to have been grown successfully, creating the world's most versatile growth technique for compound semiconductors [37].

The compound semiconductor growth process by MOCVD is often delivered to a cold wall reactor with a heated substrate within a vacuum chamber. A plethora of metal atoms with several alkyl radicals attached (methyl/ethyl/isopropyl) exist for precursor deployment. For an effective precursor gas to exist, it must maintain a reasonable vapour pressure at room temperature. Unfortunately, most metalorganic precursors are highly reactive with oxygen requiring a stainless steel bubbler and an additional inert gas such as nitrogen or highly purified hydrogen for transport to the chamber [37]. The III-V compound semiconductors require hydride gases, which are highly toxic yet less expensive than their highly reactive counterparts.

The main difference between the deployment of nitrogen versus highly purified hydrogen is the deposition rate that is available with different compound semiconductor materials. The precursor gases are selectively chosen to flow into the MOCVD reactor chamber in which the incoming materials will partially decompose and/or combine. The precursor gases, which are essentially only carriers of material, split into unique elements in which radicals and atoms are adsorbed onto the surface. The precursor gases allow for the material to travel through an external pipe system to the chamber without reacting with the sidewalls and depositing. This process leaves behind a 2-dimensional smooth layer replicating the structure of the substrate [37].

The McMaster MOCVD system (Figure 16) utilizes an overhead showerhead nozzle deposition approach in which the chamber entrance for precursor gases is perpendicular to the surface of the substrate holder. The most success thus far has come in the form of $(CH_3)_3Ga$ or TMGa (trimethylgallium) with AsH_3 (Arsine) which will react in the chamber and deposit onto the surface of the substrate below. The carrier gas, hydrogen, has a significantly higher deposition

rate than nitrogen with these semiconductor materials because of a higher reactivity level. This growth process and the difficulties surrounding the usage of Al and In compounds will be discussed below in Section 4.1.

Figure 15: McMaster University MOCVD Chamber

Figure 16: MOCVD at McMaster University

3.3. Micro-Photoluminescence Detection with Spatial Resolution

Photoluminescence describes the process of exciting an electron to a higher electronic state, leading to the radiation of a new photon as the electron returns to a lower energy state. This process (Figure 17) can be quantified through the evaluation of the photon emission in both power and wavelength output. The wavelength output of the laser device is a critical piece of information for the evaluation of the selectivity available from the SAG process. The surface area of the rectangular amorphous layer is specifically designed to slightly alter the wavelength emission. An increase in the width of the amorphous prisms will theoretically increase the amount of material that enters the cavity by altering the surface area ratio between the cavity and the amorphous layer.

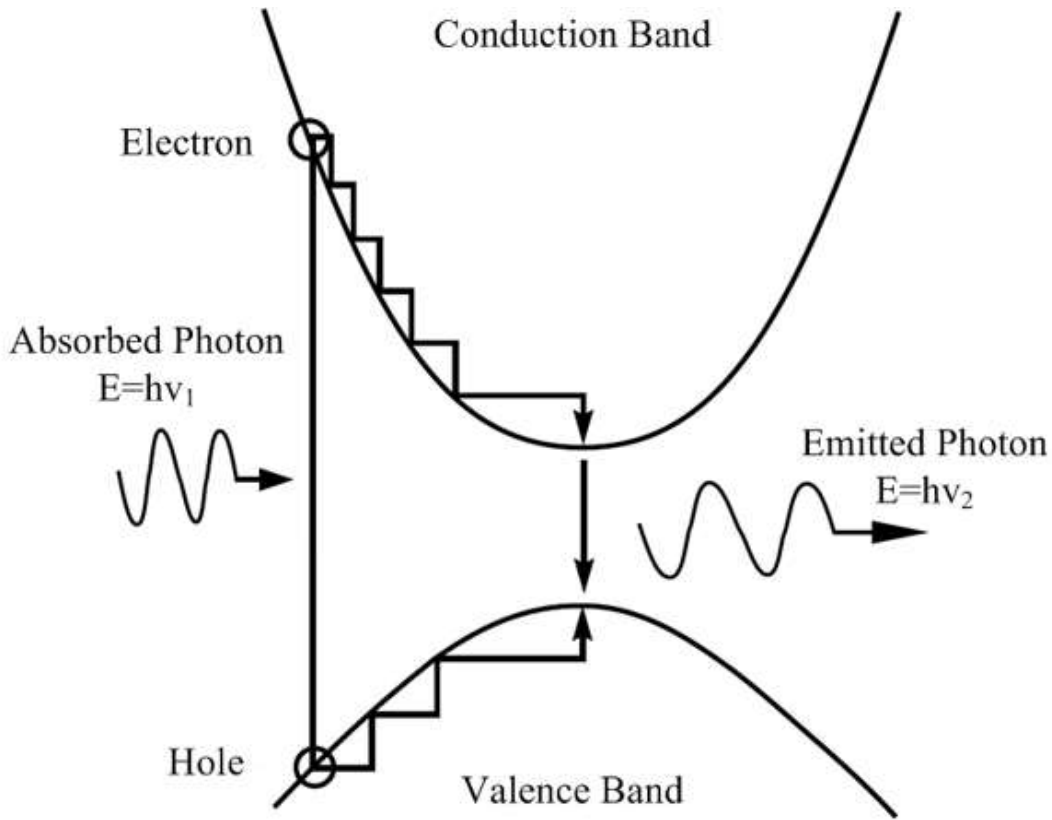

Figure 17: Basis of Photoluminescence in Semiconductors [38]

The laser emission wavelength discrepancies that arise from amorphous layer width alterations are an important parameter for device operation. The wavelength emission difference between two unique devices can be tuned for bandwidth optimization for signal processing. This is dictated by the design and understanding of the MOCVD growth mechanics, including the ability to utilize SAG on the micron scale. The emission changes that are a direct result of width alterations must be quantified to determine SAG calibration and the MOCVD parametric setup. The photoluminescence results are therefore the primary framework of SAG interpretation and modification.

To detect photon emission at the micron scale, a μ-PL system was designed and built. This device must be able to resolve single quantum well laser device photoluminescence and allow for spatially resolved scanning of the wafer surface to determine wavelength alterations in specific cavities. The system requirements are extremely sensitive, with a miniaturized laser beam spot focused onto a quantum-well laser cavity. The focused laser beam spot's width cannot exceed the cavity width, while the output emission is to be captured simultaneously. Several alterations of μ-PL designs were drafted to conform with the elusive emission capture requirement.

To first stimulate the emission of photons from the quantum-well laser, a pulsed laser was selected for operation with an external lock-in amplifier connected. The pulsed laser activates the device with significant energy per unit time however, the real difficulty is resolving the extremely weak generated emission. This process was tested extensively to minimize the distance travelled by the emission. It was determined that given the requirements of collection, the design must utilize 3-dimensional beam path modifications. The pulsed laser was directed above the sample, following the vertical plane, perpendicular to the sample. The intricacy of altering the beam path in the vertical plane required several iterations to establish an exclusive emission assembly.

A dichroic beam splitter was selected to alter the beam path post emission activation, creating a highly selective short pass filter for collection and redirection for a bandwidth above the pulsed laser emission wavelength. The dichroic filter is designed to allow light in the range of 410 nm – 633 nm to pass through with transmission band expectations at $T_{avg} > 90\%$. The filter is extremely reflective when the incoming wavelength is in the range of 685 nm – 1600 nm ($R_{avg} > 95\%$). If the filter is positioned at a 45° angle to that of the stimulated emission, the beam will deflect towards a monochromator, another selective light transmission device. The 45°

degree dichroic mirror (Figure 18) placement is independent of the original beam path because the laser wavelength will be in the transmission band region.

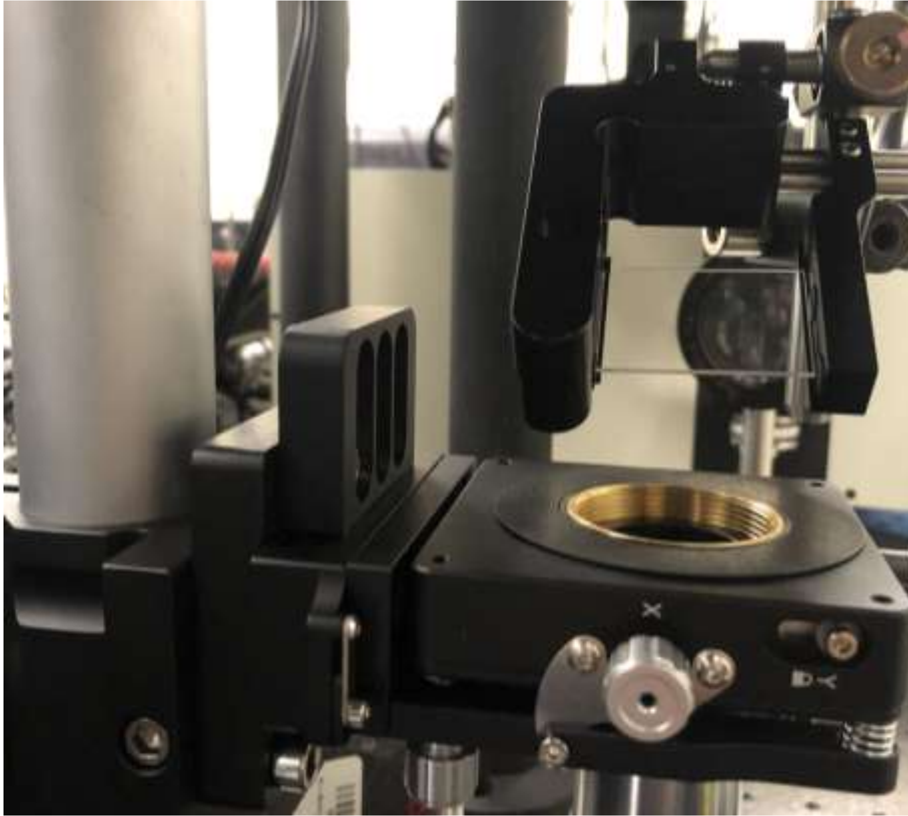

Figure 18: Dichroic Mirror Placement above XY Stage

The Katana-OneFive Nd:YAG frequency doubled (532 nm) High Power Picosecond Laser (Output shown in Figure 19) is linked with the Model SR830 DSP Lock-In Amplifier for improved signal processing discrimination. The mechanism of a lock-in amplifier, shown below in Figure 20, will allow for discretization of signal processing. Lock-in amplification will allow for phase matching of the photoluminescence signal, provided by the frequency set on the pulsed laser. When the frequency of the pulsed laser is matched with a reference signal, the detection of the µ-PL is attainable by deterministic square wave high to low signal ratio. The reference signal

is dependent on an offset to the pulsed laser frequency which will allow for detection of the μ-PL signal's entirety, providing high and low thresholds of the output signal.

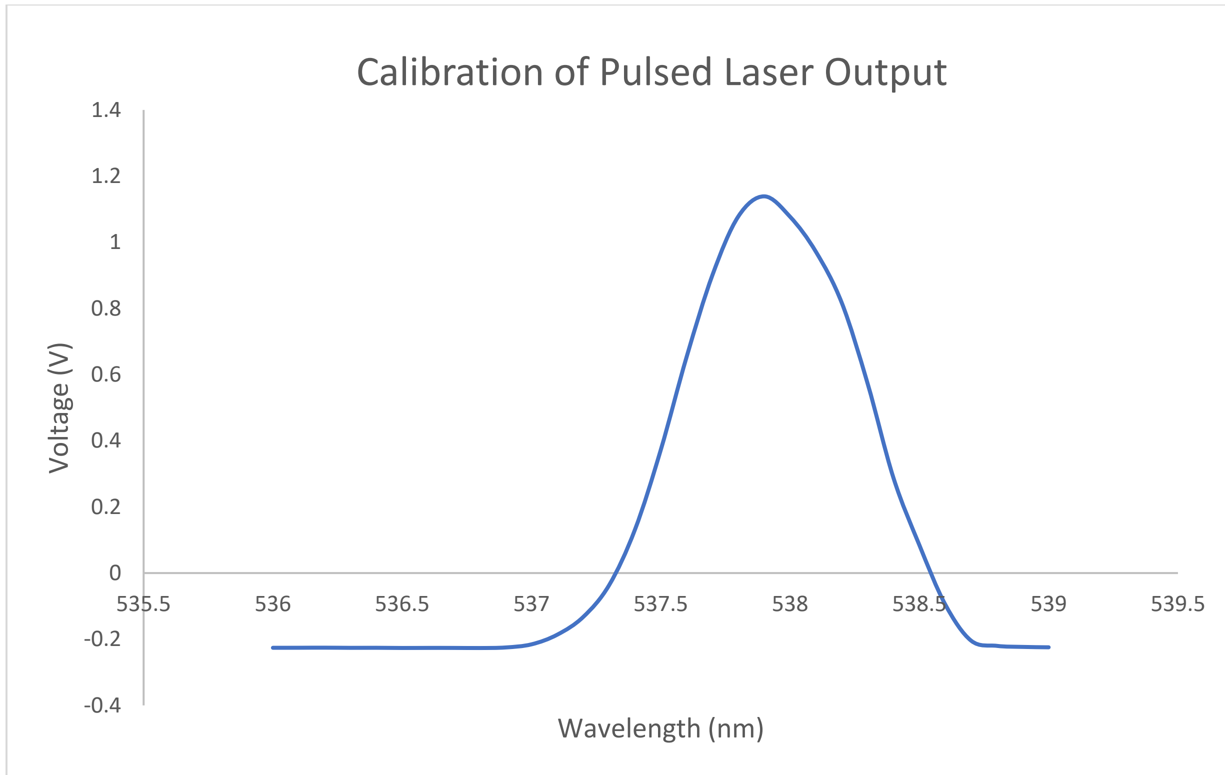

Figure 19: Laser Emission Wavelength Calibration of 532 nm Nd:YAG Frequency Doubled

The original setup could not successfully resolve data points without lock-in amplification shown below in Figures 21 and 22. This is a result of constant fluctuations in the measurement readings displaying on the voltmeter. To solve this, lock-in amplification offset can quantify signal high to signal low for optimal control of signal processing output of voltage. The pump laser must initiate the photoluminescence process while maintaining a perpendicular orientation relative to the wafer. This process will allow for the pump laser beam and the stimulated emission spectrum to be concentrated through both ends of a microscope focusing lens. Several design decisions

were necessary to manipulate the beam path for full repeatable operation, with distinguished quality and precision of measurement.

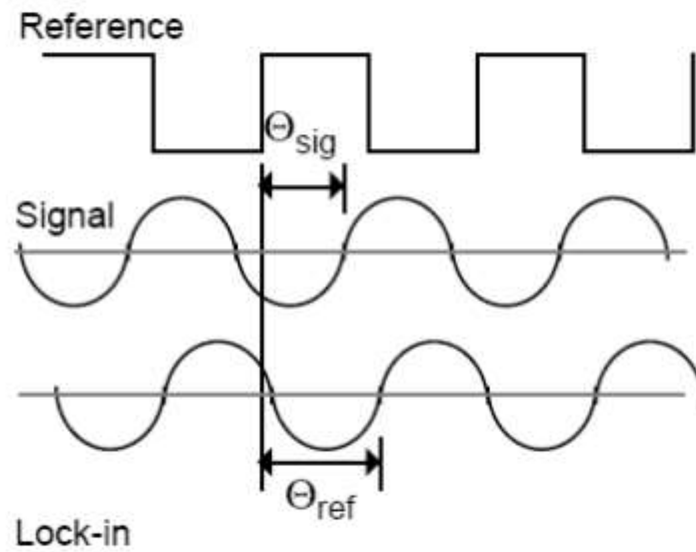

Figure 20: Basis of Lock-In Amplification [39]

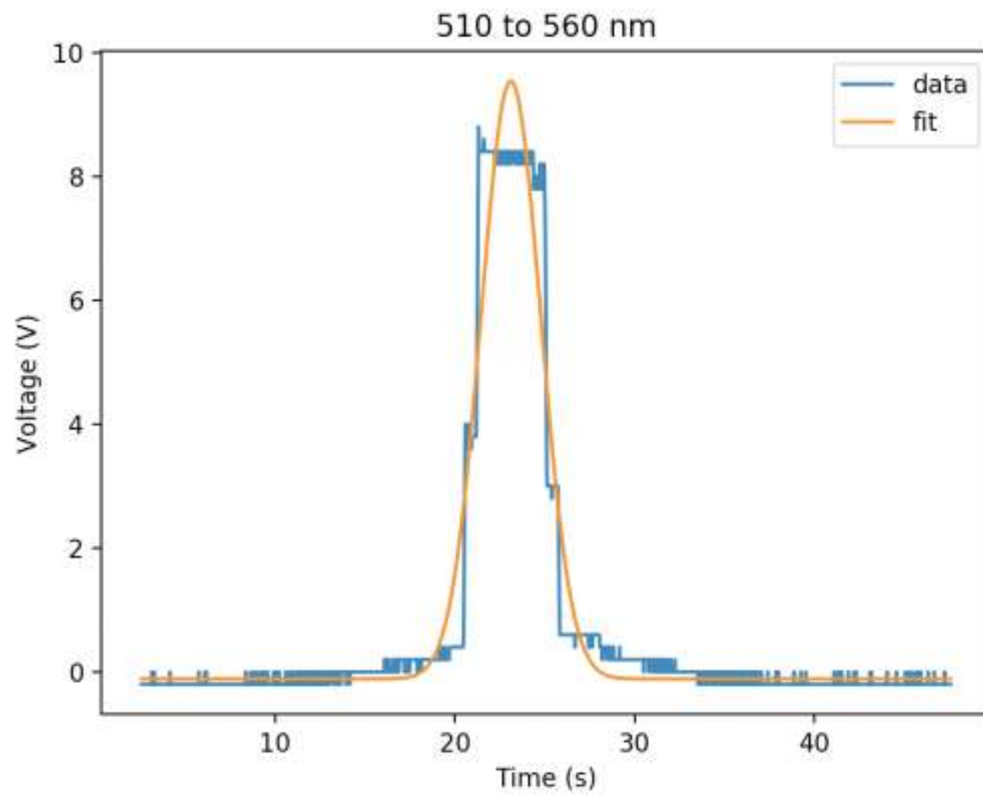

Figure 21: Calibration Testing Example for Nd:YAG Laser without Lock-In Amplification (2 Second Time Steps)

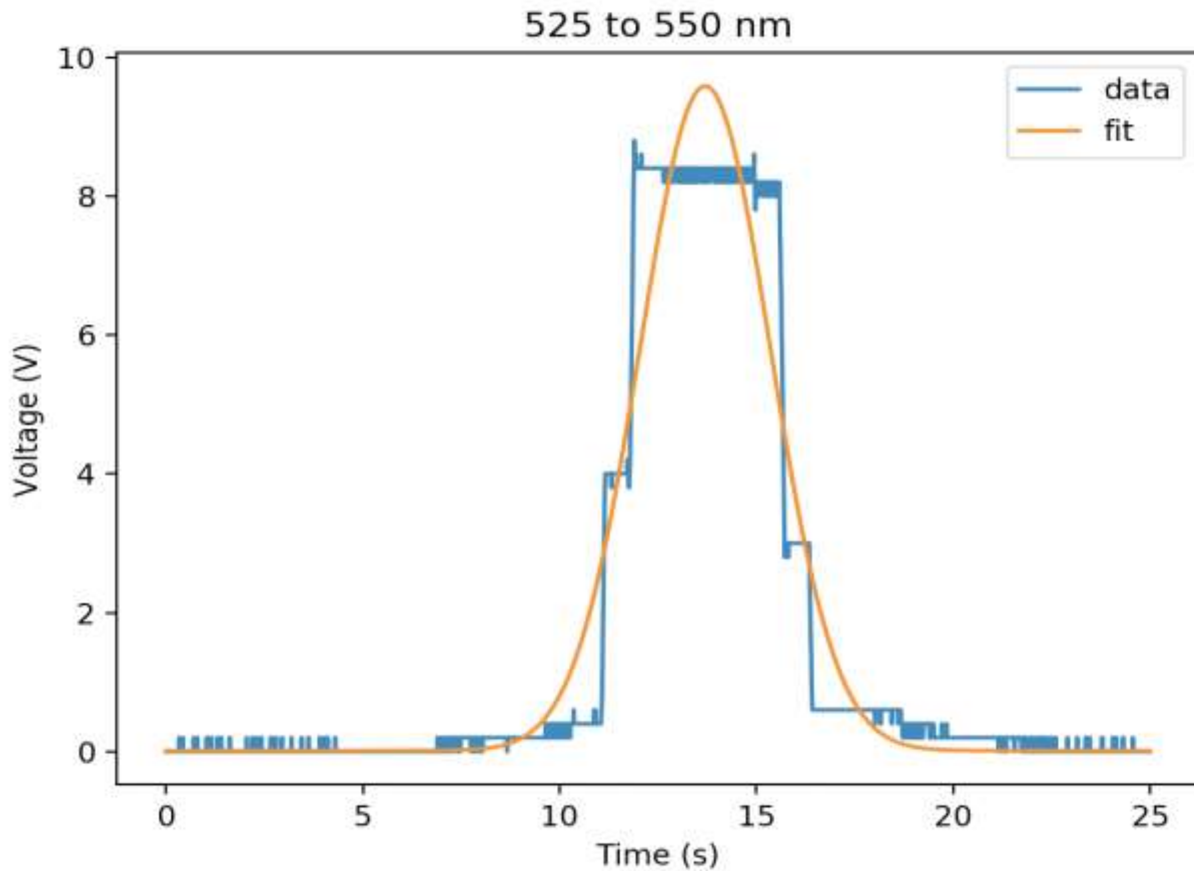

Figure 22: Calibration Testing Example for ND:YAG Laser without Lock-In Amplification (1 Second Time Steps)

To begin, the pump laser was directed 35 cm above the optical table to allow for a perpendicular beam path relative to the table orientation and a sufficient working distance. This would allow for the sample, which will essentially mimic a mirror, to lay flat onto a mobile surface. The division of the beam path was divided into two filtering mechanisms including camera imaging and wavelength bandpass filtering. The difficulty of this filtering process stems from the free space manipulation necessary to direct a beam path on a vertical trajectory through multiple filters without blocking the beam path itself.

The NanoGenie™ camera was selected to provide high quality micron scale imaging of the wafer surface to quantify the coordinates and width of the pump laser focused beam spot. Imaging of the surface provides the user with valuable information to resolve the beam spot alignment relative to the test cavities. The main laser beam path is altered along the vertical plane in a position at approximately 20 cm above the sample. In this position there exists a 50/50 polarizing beamsplitter that will allow the transmission of the 420 nm – 680 nm light ($\frac{Tp}{Ts} > 500:1$) to travel to the camera's field of view. Due to the pulsed laser's power, a factor of two for loss at this stage was not estimated to be an issue with photoluminescence activation.

The pulsed laser beam that is partnered with the lock-in amplifier is directed down on to the sample in which the stimulated emission deflects into the monochromator for absorption by an external photodetector. The photodetector, Silicon Model 2032 Large-Area UV Photoreceiver, can resolve the voltage of the stimulated emission and provide an output power. The voltage values can then be altered for sensitivity and a μ-PL graph can be produced. The μ-PL graph is created by a LABVIEW connection that cycles the monochromator through a set range of wavelength outputs while simultaneously reading the voltage values. The graphical output in this context will depict the voltage versus the wavelength range highlighting the emission spectrum of the sample. The voltage exists as an arbitrary unit pending calibration. This formulation leads to the critical evaluation of μ-PL in terms of signal shape, not necessarily emission power.

The purpose of this setup is to determine the variability of quantum-well laser emission in different surface cavities. The Zaber XY stage allows the user to determine the absolute position of the laser beam spot by translational discrete movement. The translational movement can be monitored by the camera that is placed above the sample, ensuring both the position and width of the beam spot. The dynamic XY stage is placed directly beneath the static microscope focusing

lens, providing 2-dimensional movement of the sample. The entire system is administered by LABVIEW software, automating the wavelength range of the monochromator, XY stage movements and voltage readout.

A coarse beam photoluminescence system at the Tandem Accelerator Building Annex in the CEDT was utilized to calibrate the μ-PL system using a GaAs substrate with proven consistent photoluminescence. The coarse system deploys a chopper mechanism at 100 Hz with a HeNe laser (632.8 nm), the emission spectra of the GaAs calibration sample is shown below in Figure 23. The emission spectrum of this sample (Sample X) functioned as the baseline test for the new μ-PL system, contributing to a sample standardization regardless of beam spot size. This sample was rigorously tested with multiple detectors at different frequencies to understand the limitations and capabilities of the first functional iteration.

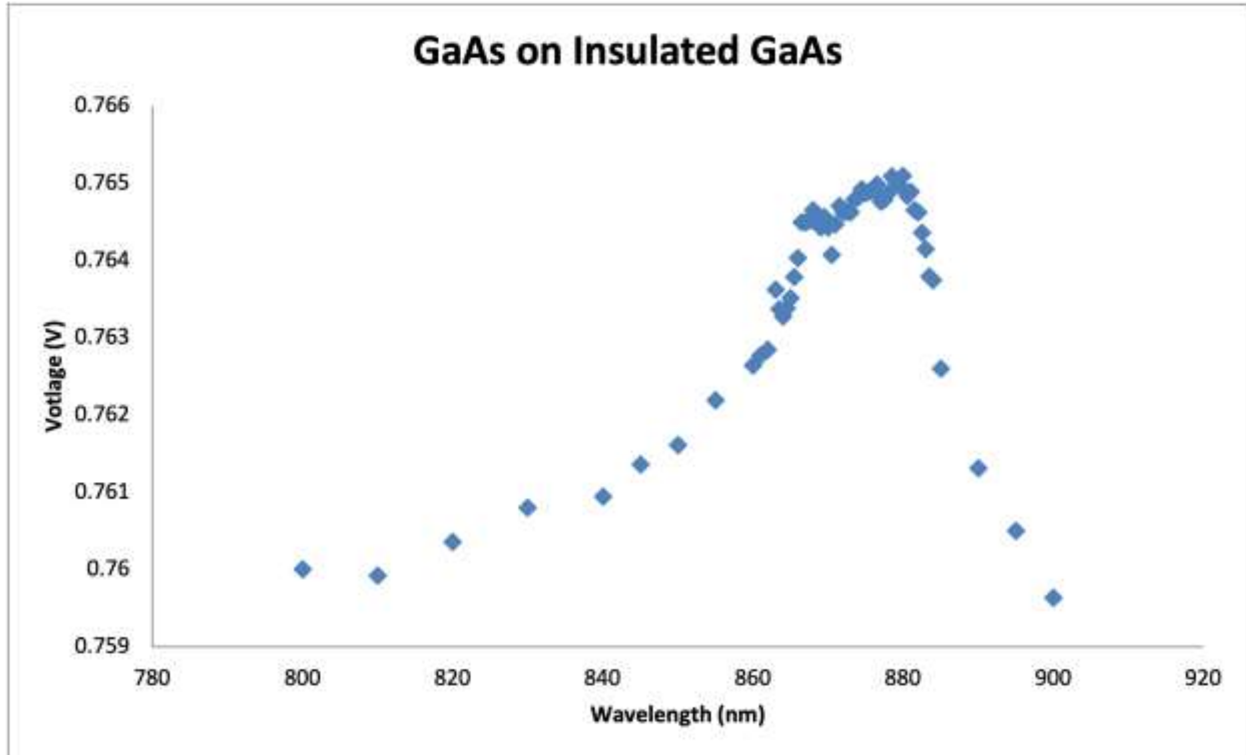

Figure 23: Calibration Test for Sample X's GaAs Substrate Photoluminescence using Nd:YAG Laser with Lock-In Amplification

The silicon detector showed promising results in the first iteration while producing the μ-PL baseline of GaAs on insulated GaAs (Sample X). The Model 2033-Infrared-Germanium detector was also tested with the same sample shown below in Figure 24. The detector comparison is made possible by interpolating the system sensitivity data shown below in Figure 25 and 26. The emission wavelength range of specific interest will consistently produce in the near-IR range (800 nm – 2500 nm) based on the compound semiconductors that will be utilized later. The sensitivity of the silicon detector evidently drops off at the bandgap edge of silicon at approximately 1100 nm therefore, for the purposes of calibration the silicon detector can be utilized only in the short term. For future work, specifically the targeted AlGaInAs, the detector

must coincide with a range of approximately 1300 nm – 1650 nm, pertaining to the use of InGaAs or Ge detection.

In summary, the μ-PL system illuminates a semiconductor wafer that is placed on an XY translational stage to detect photoluminescence output. A high-powered pulsed laser is directed perpendicular to the substrate and is diverted at two unique filtering stages to create an image in a camera system for beam spot assurance and selective short pass mirror. The laser system is connected to a lock-in amplifier to create a high level of discrimination for signal processing and emission power output. The system at this stage is calibrated for an emission wavelength up to 1100 nm and will be tested with samples directly from MOCVD processing with room temperature photoluminescence.

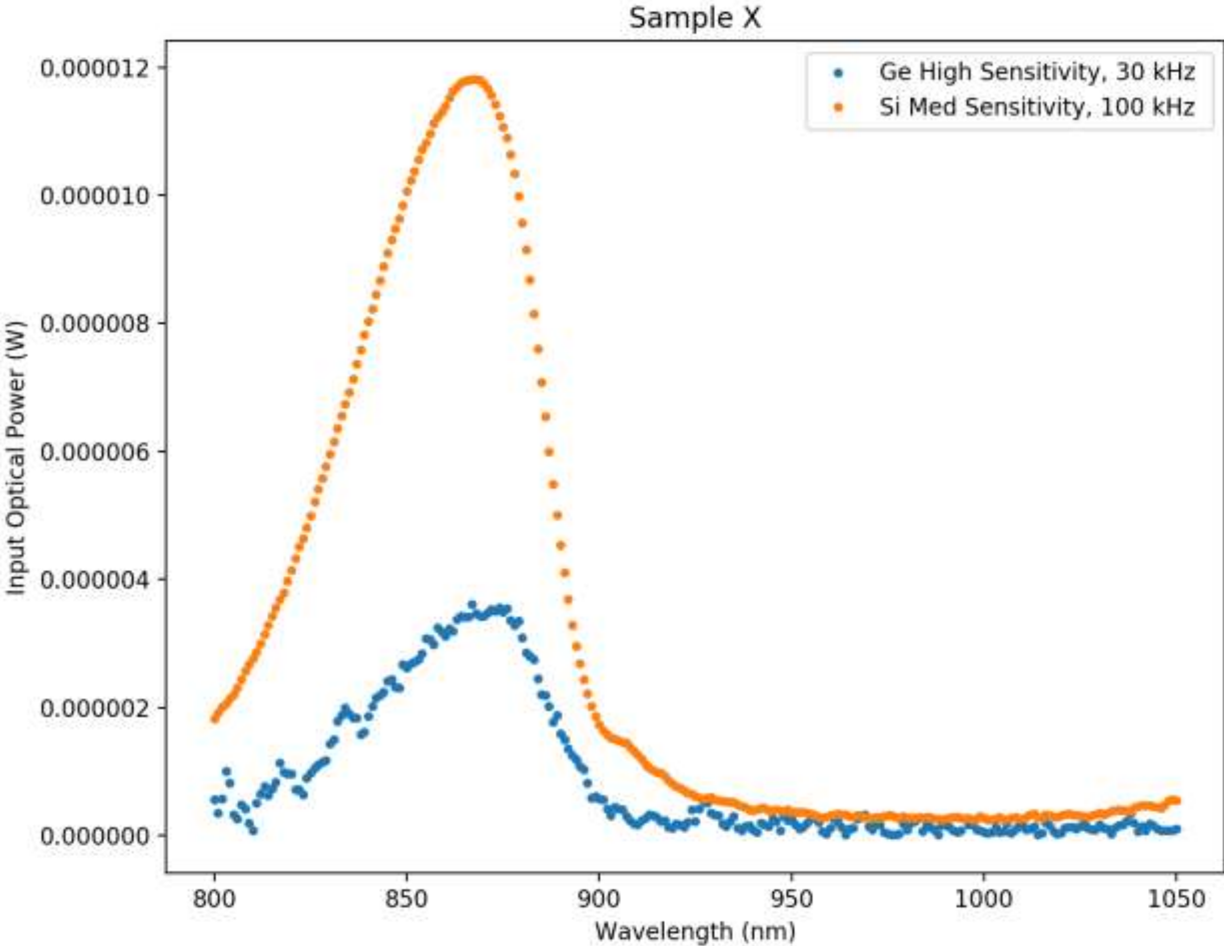

Figure 24: Sample X Tested for GaAs Substrate Photoluminescence with Ge/Si Detectors

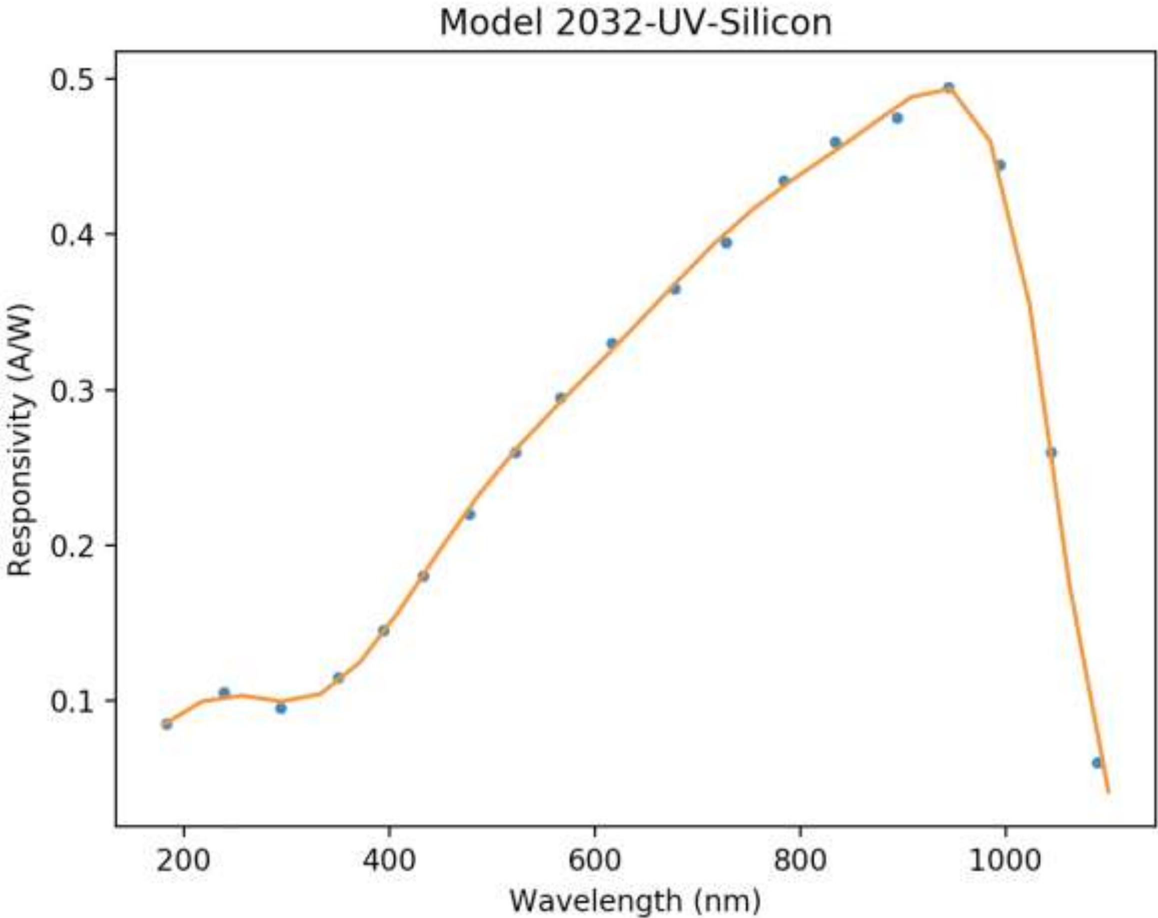

Figure 25: Model 2032-UV-Silicon Responsivity Provided by Supplier Manual

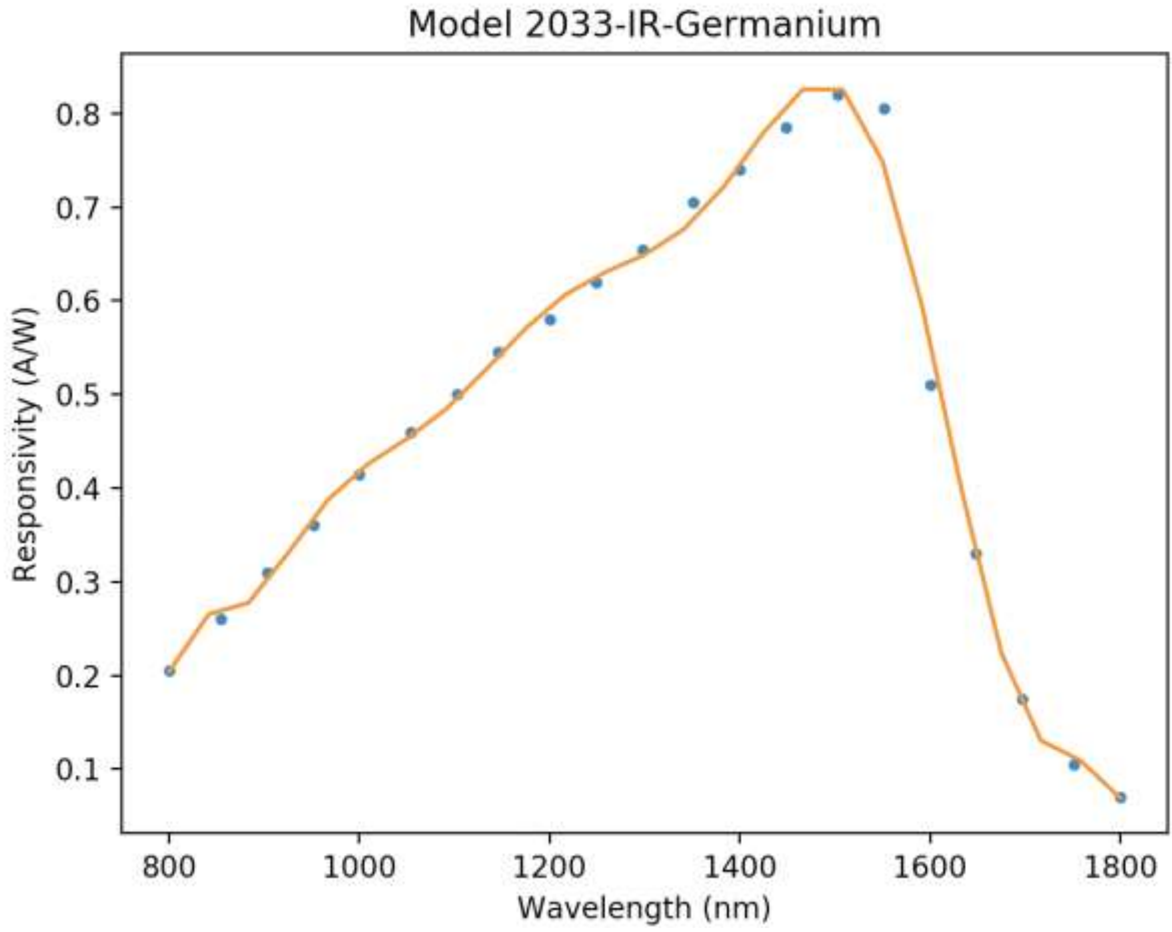

Figure 26: Model 2033-IR-Germanium Responsivity Provided by Supplier Manual

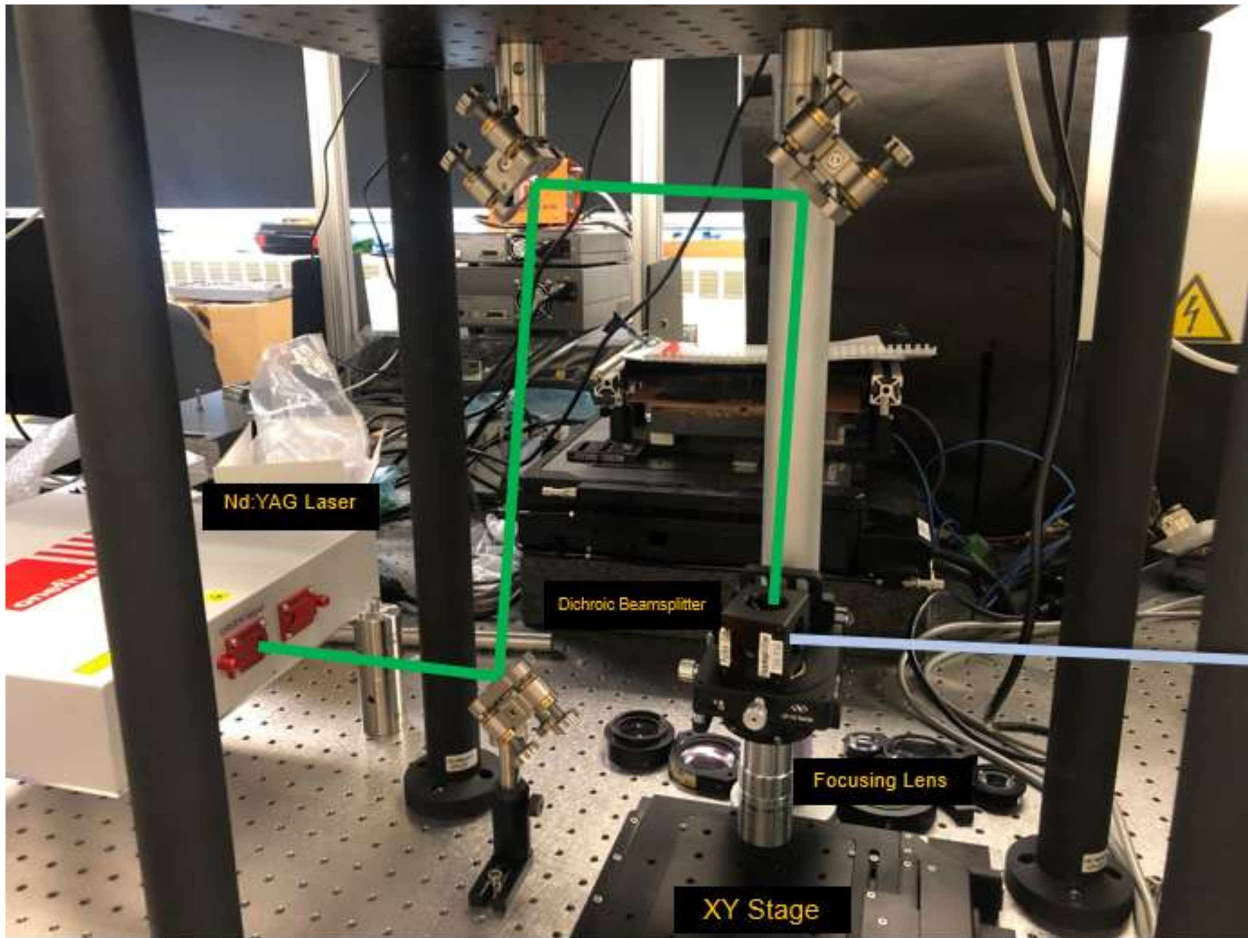

Figure 27: Nd:YAG Laser in μ-PL Setup

3.4. Post-Processing Evaluation

Characterization of the growth process will provide invaluable information for the calibration of the MOCVD process and SAG deployment. Prior to MOCVD the sample is imaged using an optical microscope to confirm the uniformity and placement of the 3-dimensional structures. Optical microscopy can provide a significant understanding of the coarse quality of each structure's edge however, it is not possible to determine if overetching occurred during the procedure at this scale. The optimal adjustment is to image the sample with higher magnification and introduce a cross sectional divide. This method is strictly for the calibration of device level

growth repeatability, and to acknowledge the relationship between MOCVD and pre-growth processing.

To quantify the growth mechanics of MOCVD, cross sectional imagery from a scanning electron microscope (SEM) will be utilized to determine parameters such as reproducibility and layer thickness. The SEM imagery will provide a comparison to a set MOCVD recipe in which Dr. Manu Hegde can collaboratively solidify the growth parametric control. Each layer thickness will be slightly altered by the SAG however, the discrepancy in each layer should be consistently set by the surface area of the adjacent structures. The SEM imaging of the SAG sample is crucial for the timeline of MOCVD development at McMaster University.

To achieve a scanning electron beam, an electron producing gun is fired through a series of lenses and apertures to produce a focused beam of electrons guided towards the surface of the sample. The sample is mounted in an isolated chamber area which is evacuated to a high vacuum setting that can often be adjusted with the user interface. A set of scanning coils facilitate the scanning and directional manipulation of the beam across the sample surface. The high-energy beam reacts with the material on the sample creating a new source of electrons. The produced electrons exist as secondary, auger, backscattered and characteristic X-rays. A detector is placed adjacent to the sample, collecting the produced electrons to create an image for the operator.

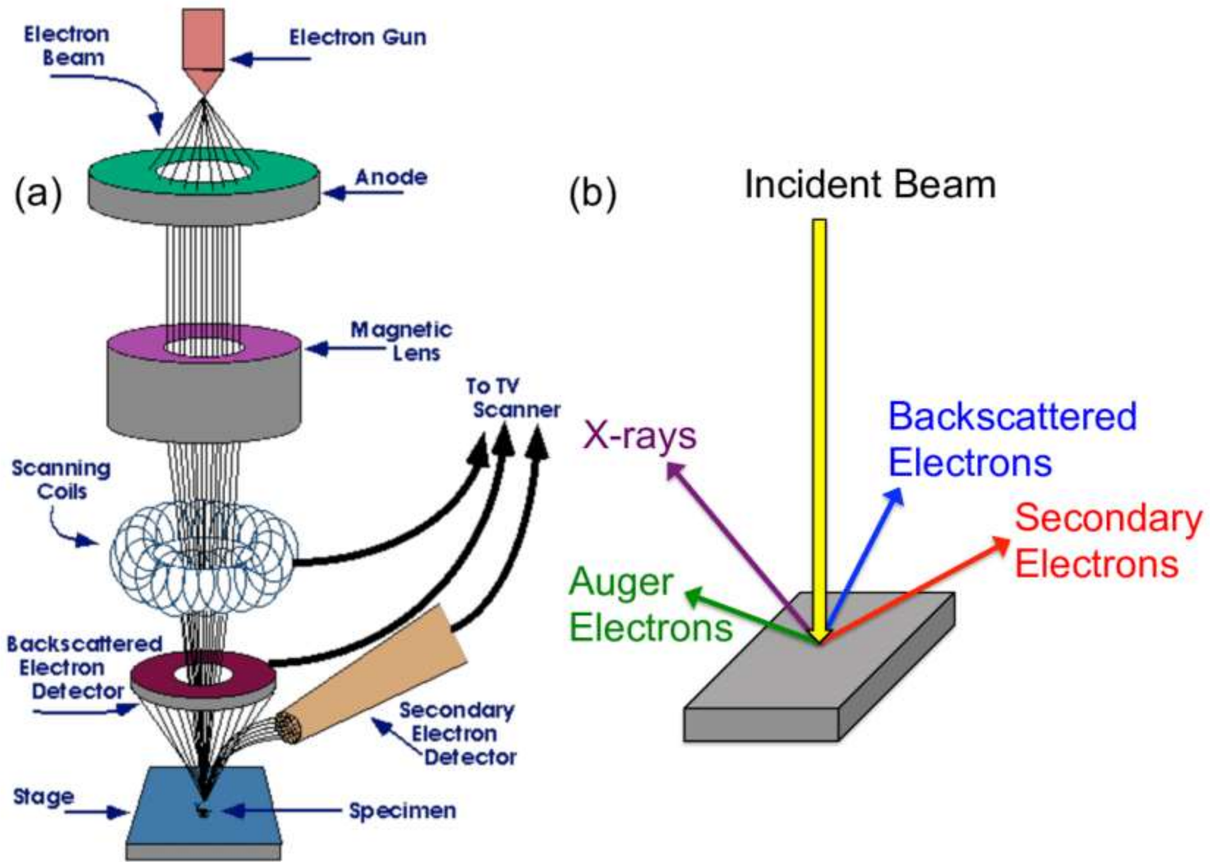

Figure 28: Schematic of SEM Basis [40]

Atomic force microscopy (AFM) is an analysis technique to resolve topographic information from a substate's surface. The system utilizes a raster scanning module with a piezoelectric element to enable precision surfacing scanning. AFM will allow for the understanding and confirmation of total thickness of structures, with a surface topographic map. The precision of the topographic quantitative measurement can be compared to SEM imagery as a qualitative baseline. The progress of MOCVD growth control can be determined by a scan of the structure edge to determine the selectivity of growth within the cavity. SEM provides very high-resolution images, but feature thicknesses are difficult to quantify. AFM is the preferred method for thickness determination.

The AFM system operates with a cantilever tip or point probe that scans across the surface of sample. The cantilever, often made of Si or SiN, is a miniature tip whose radius is on the order of single digit nanometers. When the tip is driven across the surface, forces between the tip and the sample will cause deflection of the cantilever.

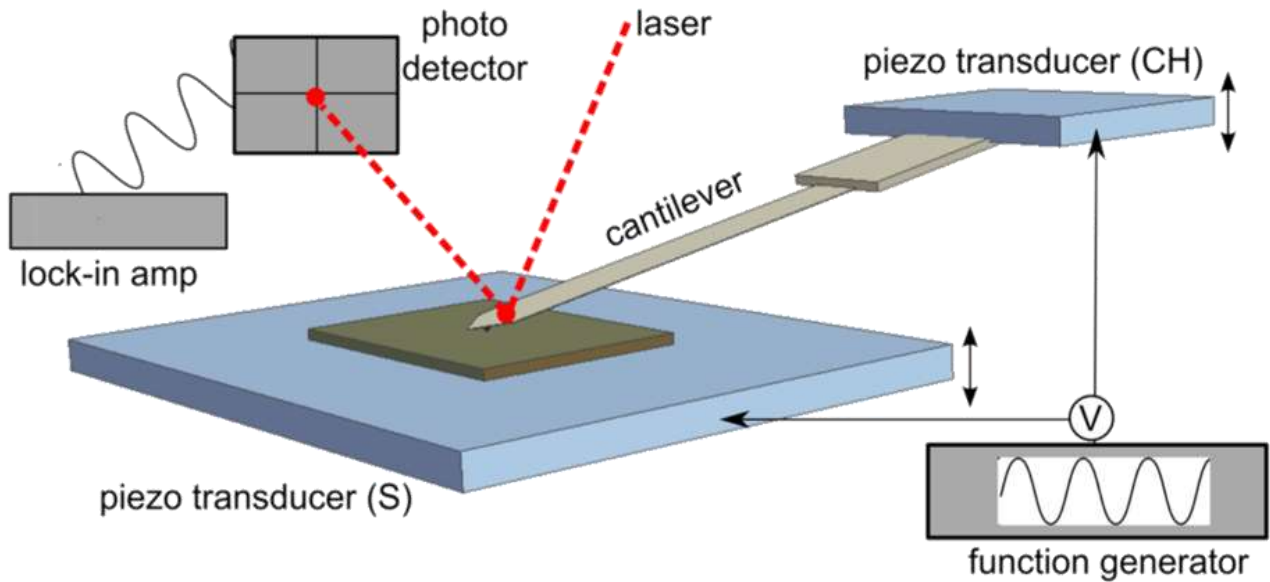

Figure 29: Schematic of AFM Basis [41]

4. Results

4.1. Growth Mechanics

The MOCVD material capabilities were initially limited for the calibration and operational setup of the facility. The timeline of full functionality was also extended due to the COVID-19 pandemic. The material system AlGaInAs is the full system objective of this project however, the timeline for growth with Al and As at this facility is still a work in progress. The material system that is explored in this section depended solely on the calibration sequencing that Dr. Hegde was utilizing at the time of the experiment.

To begin MOCVD operation, individual material calibration was to be completed before new material systems could be introduced. Dr. Hegde began the procedure with GaAs substrates, leading to the first development of a quantum-well structure of AlGaAs-GaAs-AlGaAs. The growth mechanics were initially difficult to understand without several iterations because characterization can lead to several parametric changes that could be made. During the calibration of GaAs with Al, it became clear that this material system, although promising, required an immense amount of arsine compared to other material systems.

The Al material system has a very low vapour pressure and high reactivity with contaminates. This issue drove the amount of arsine, an expensive pre-cursor gas, to drastically increase to compensate for the Al reactivity. With the limitations apparent with initial Al results, it was decided the best course of action was to proceed with InGaAs.

The InGaAs material system has developed throughout 2021, leading to fine compositional control for GaAs-InGaAs-GaAs quantum-well structures. When initial characterization began,

the surface features were an order of magnitude thinner than anticipated. It was discovered when deploying TEGa (triethylgallium), the growth rate is lower than predicted. This process was then calibrated for TMGa (trimethylgallium), which can now successfully provide approximately 2.5 μm per hour of InGaAs growth.

To institute an enduring foundation of SAG at McMaster University, InGaAs was deployed to showcase initial selectivity and growth success. The following section will showcase the growth of InGaAs quantum-well lasers on GaAs substrates, resulting in initial MOCVD characterization. This section will evaluate the current state of MOCVD SAG capabilities at McMaster University and deliver an action plan for future work based on initial characterization findings and evaluation.

The structure of the GaAs-InGaAs-GaAs quantum-well was designed around basic double heterostructure design as an initial approach to create a device with photoluminescence (Figure 30). The GaAs substrate was first covered with a GaAs buffer layer (600 nm) to introduce a perfect lattice match and institute a high-quality crystallographic order for the quantum-well growth. The simple quantum-well structure contains 30% [In] and 70% [Ga] composition, with a 10 nm thickness that is placed on the surface of the buffer layer. The quantum-well structure is then covered with a capping layer of GaAs (150 nm) to reduce strain of the lattice and eliminate blue-shifting of photoluminescence by strain release.

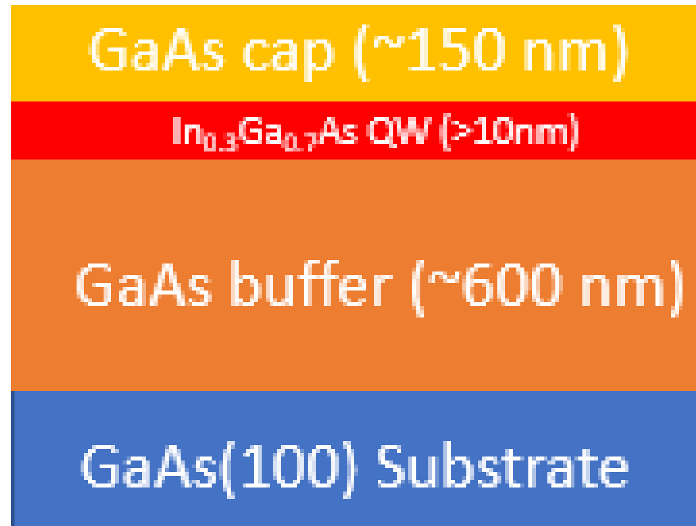

Figure 30: S-28 Structure of Grown GaAs Quantum-Well

This system was also altered for 15% [In], a common compositional equivalency for solid-state devices. The 30% [In] is designed to boost the confinement factor of the quantum-well and produce photoluminescence for calibration purposes. Several iterations of growth occurred for calibration purposes; the samples of interest are highlighted in the following sections including:

Table 1: InGaAs Samples

Name	*Gallium Precursor*	*Buffer Layer Thickness (nm)*	*Chemical Formula*	*Cap Layer Thickness (nm)*
S-28	TEGa	600	$In_{0.29}Ga_{71}As$	150
S-31 (BETH)	TMGa	600	$In_{0.13}Ga_{0.87}As$	150
S-32	TEGa	600	$In_{0.29}Ga_{71}As$	150
S-34	TEGa	600	$In_{0.29}Ga_{71}As$	150

In the following sections, the characterization is shown, both before and after MOCVD processing using various techniques including SEM and AFM.

4.1.1. Scanning Electron Microscopy

Utilizing SEM imaging can significantly benefit the semiconductor growth process by exploring and identifying growth mechanics. The surface scanning and rotational features allow for a complex 3-dimensional understanding of the growth's surface identity. A coarse SEM system was deployed for imaging of the silica mask while an exceptionally fine SEM was used for MOCVD growth mechanic investigation. The final iteration of the silica mask is shown in Figure 31. This structured pattern was repeated on the surface of the substrate to create photoluminescence redundancy. Shown below in Figure 32, the entire surface area of S-34 is covered with the pattern repeated.

The SEM imaging was initially a procedure to characterize the growth of the silica mask, however, the complexity of SEM for cross-sectional evaluation was completed by Spencer McDermott an experienced operator at 90-degree offsets.

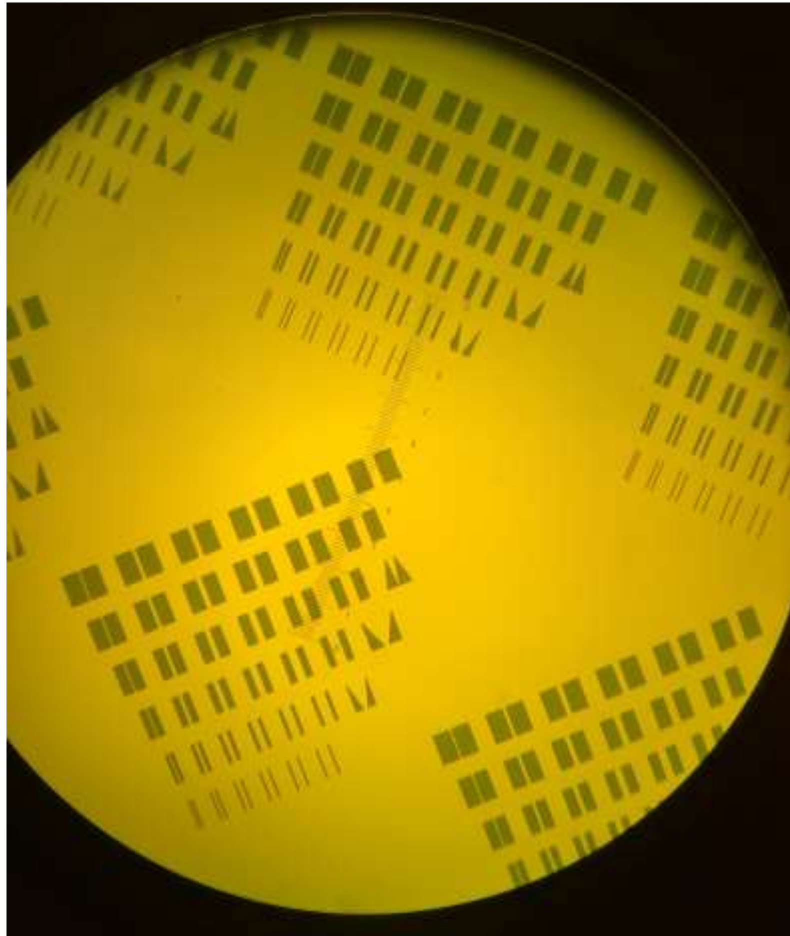

Figure 31: Optical Microscopy Image of Silica Masking Repeated Across the Substrate Surface

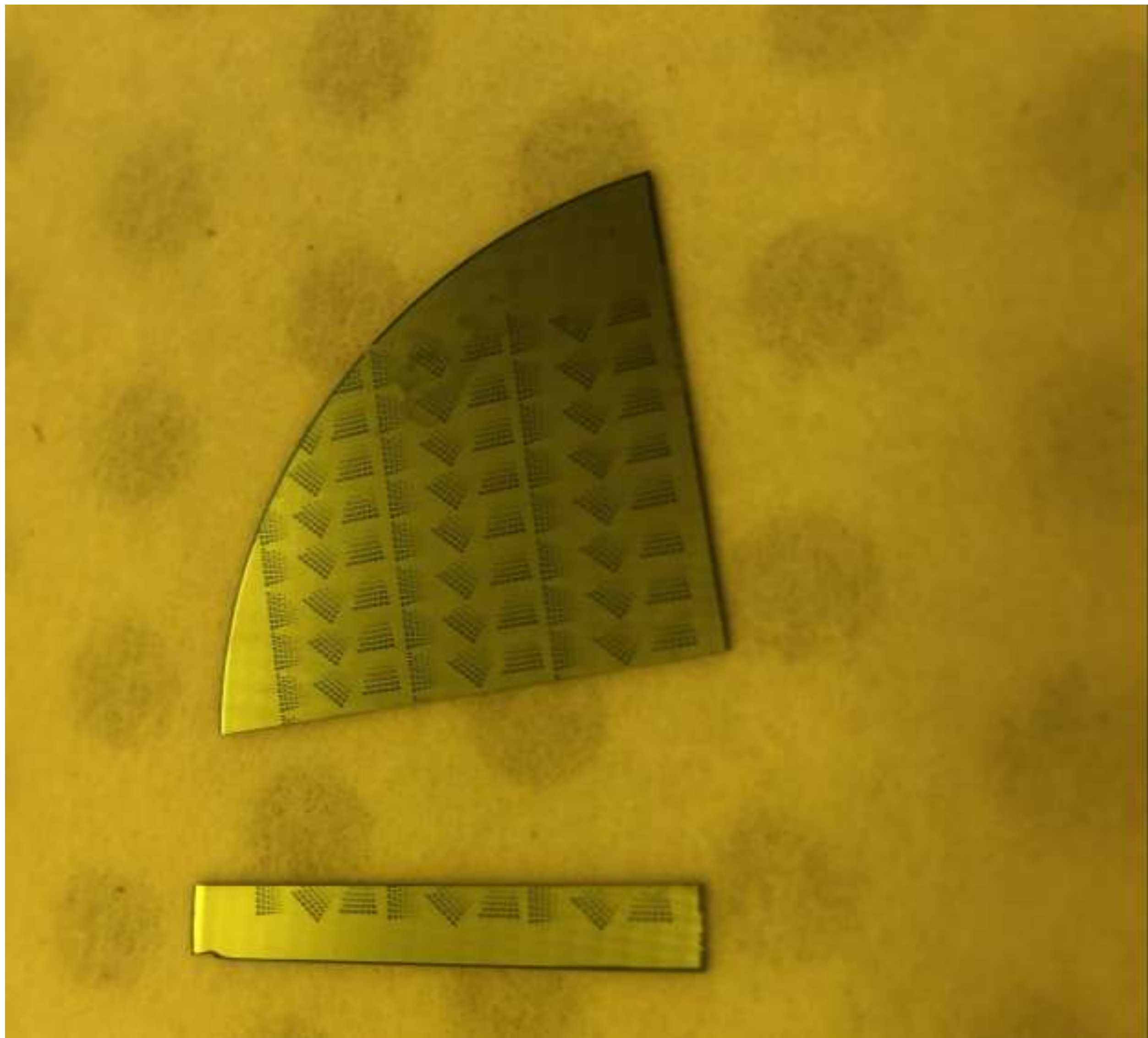

Figure 32: GaAs Wafer Cleaved for SEM Imaging with Silica Masking Repeated Across the Substrate Surface

The selectivity of creating the silica mask was demonstrated with coarse SEM to explore the sizing limitations of the masking features. In Figure 33, the entire feature comparison is shown with offsets between the rectangular prisms as well as parametric comparisons of length and width. In Figure 34, the 20 µm structure is shown, demonstrating the continuous top leveled plane to be compared below with the 10 µm structure shown in Figure 35. The 10 µm feature sizing is attainable using the direct writing laser system however, the selectivity during the

MOCVD process would be hindered by a surface plane that is dominated by faceted side walls. It was determined that the minimal feature sizing for silica masking was to be 20 µm. Additionally, there was also no evidence that length was affected until the same 20 µm threshold was approached.

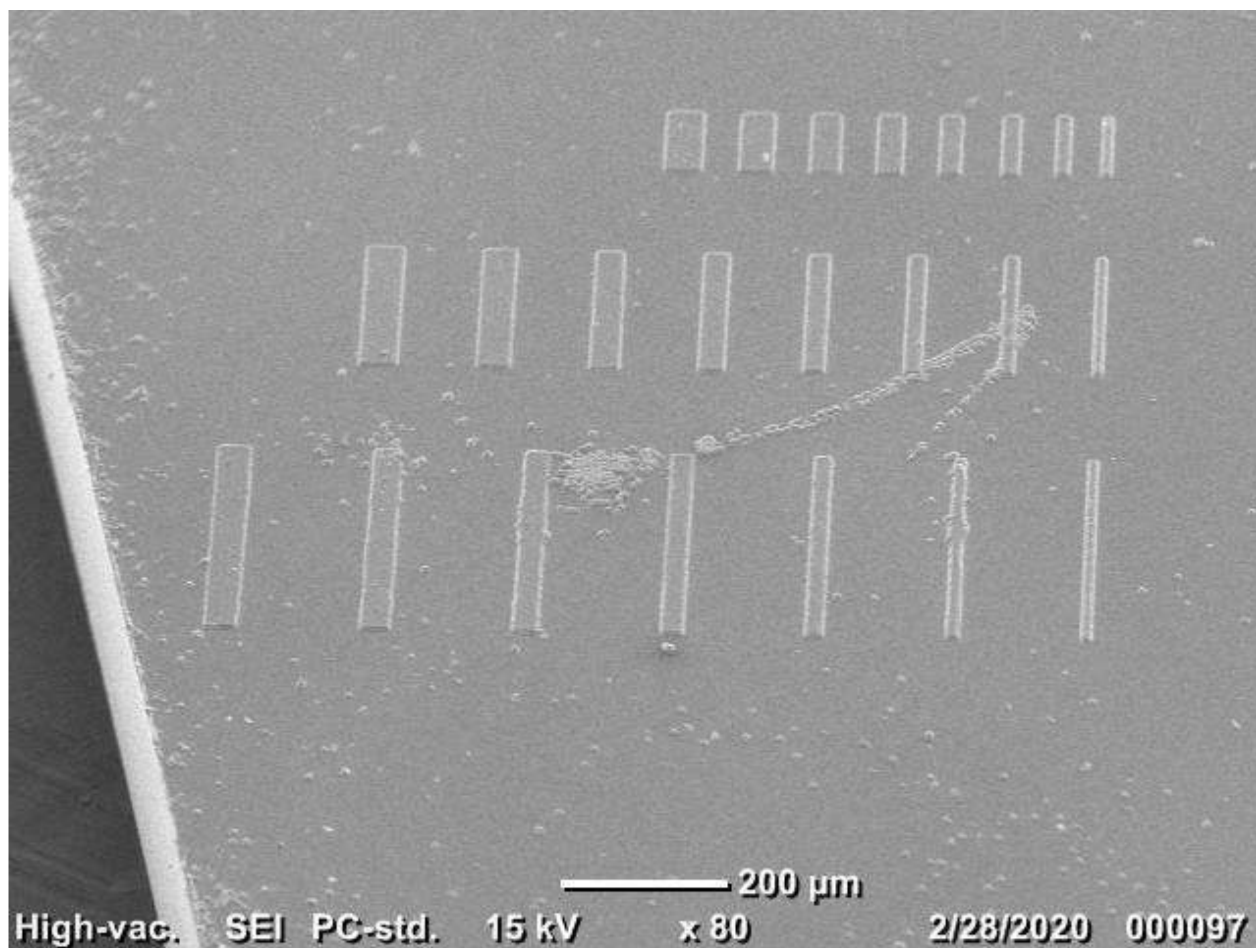

Figure 33: SEM Image of Silica Masking on GaAs Substrate for Silica Mask Sizing Calibration

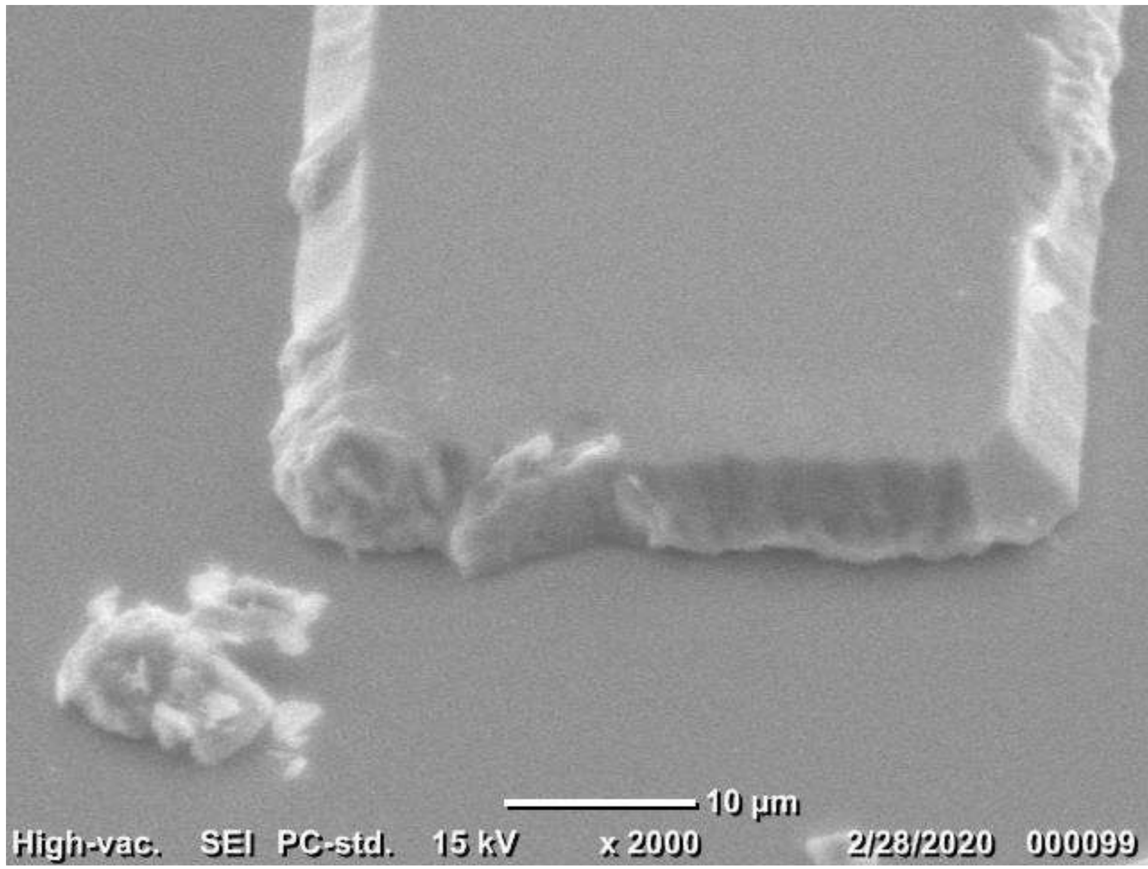

Figure 34: SEM Image of Silica Mask Structure on a GaAs Substrate with 20 µm Width

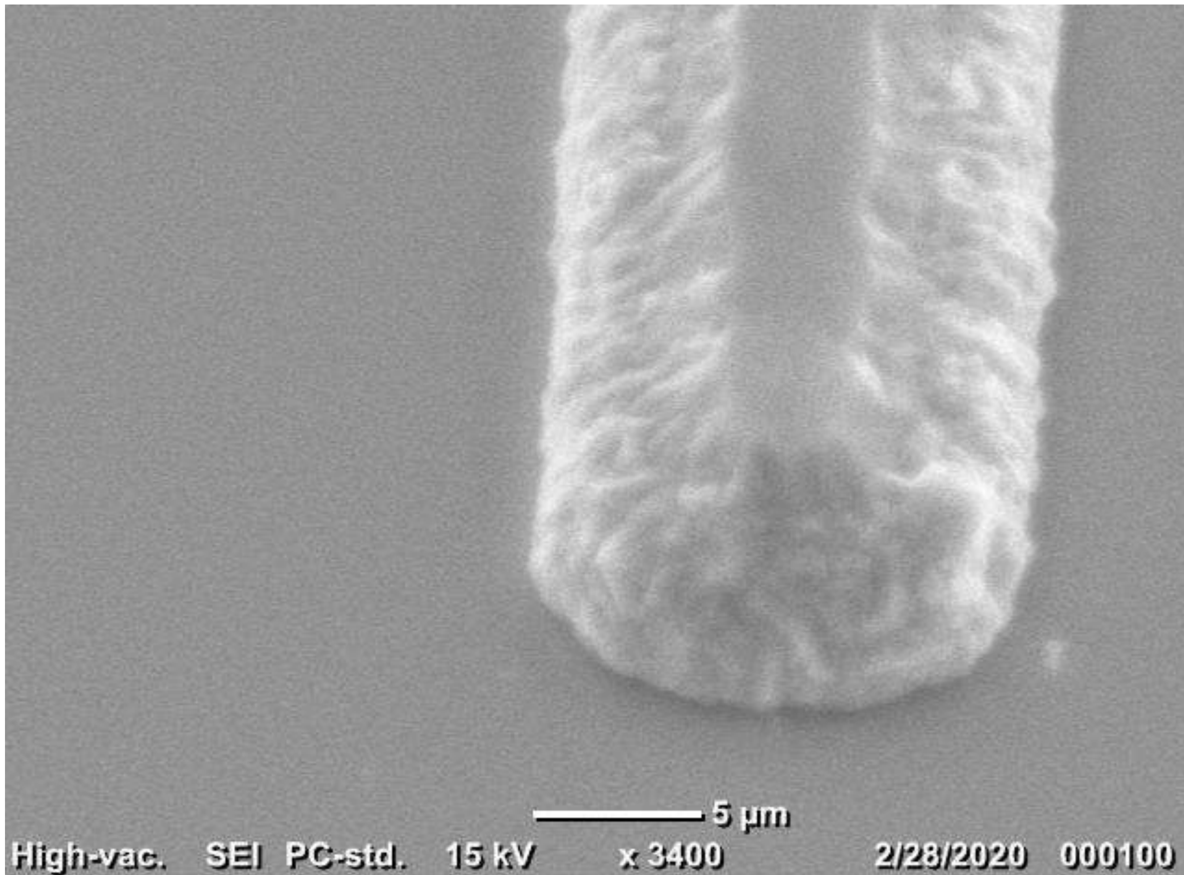

Figure 35: SEM Image of Silica Mask Structure 10 µm Width

The silica masking was consistently demonstrated leading up to the MOCVD growth process by SEM imaging and optical microscopy. The MOCVD growth was then completed, and S-34 was evaluated for growth mechanics. Leading up to the growth process, it was anticipated that the MOCVD growth would be an order of magnitude thicker than the 100 nm silica layer. Upon SEM imaging it became apparent that the MOCVD growth was difficult to determine topographic information from a top-angled view. Shown in Figure 36, there is a thickness discrepancy between the silica mask and the MOCVD growth.

Upon further investigation it was determined using Figure 44/45 that the growth rate of the process was immensely over-estimated. As stated above, this growth utilized TEGa, which acted

as a limiting factor for the growth rate in the chamber. This image was the initial characterization of TEGa and will provide the necessary alterations to parametric control moving forward. The light section on the left is the MOCVD growth, placed above the dark silica masking on the right of Figure 44/45. The expected thickness (760 nm) was not achieved based on the apparent size discrepancy of the silica (100 nm) to MOCVD growth, however, this is the first demonstration of SAG at McMaster. This demonstrates that there is minimal growth from the MOCVD on the surface of the silica masking, showcasing high selectivity based on Figure 44/45 and the colour of the surface features respectively.

This discovery, an initial characterization of the InGaAs quantum-well growth, significantly benefits the control of TEGa methods moving forward with this MOCVD system. The SEM images of the surface are shown below, demonstrating the silica in fine SEM image quality.

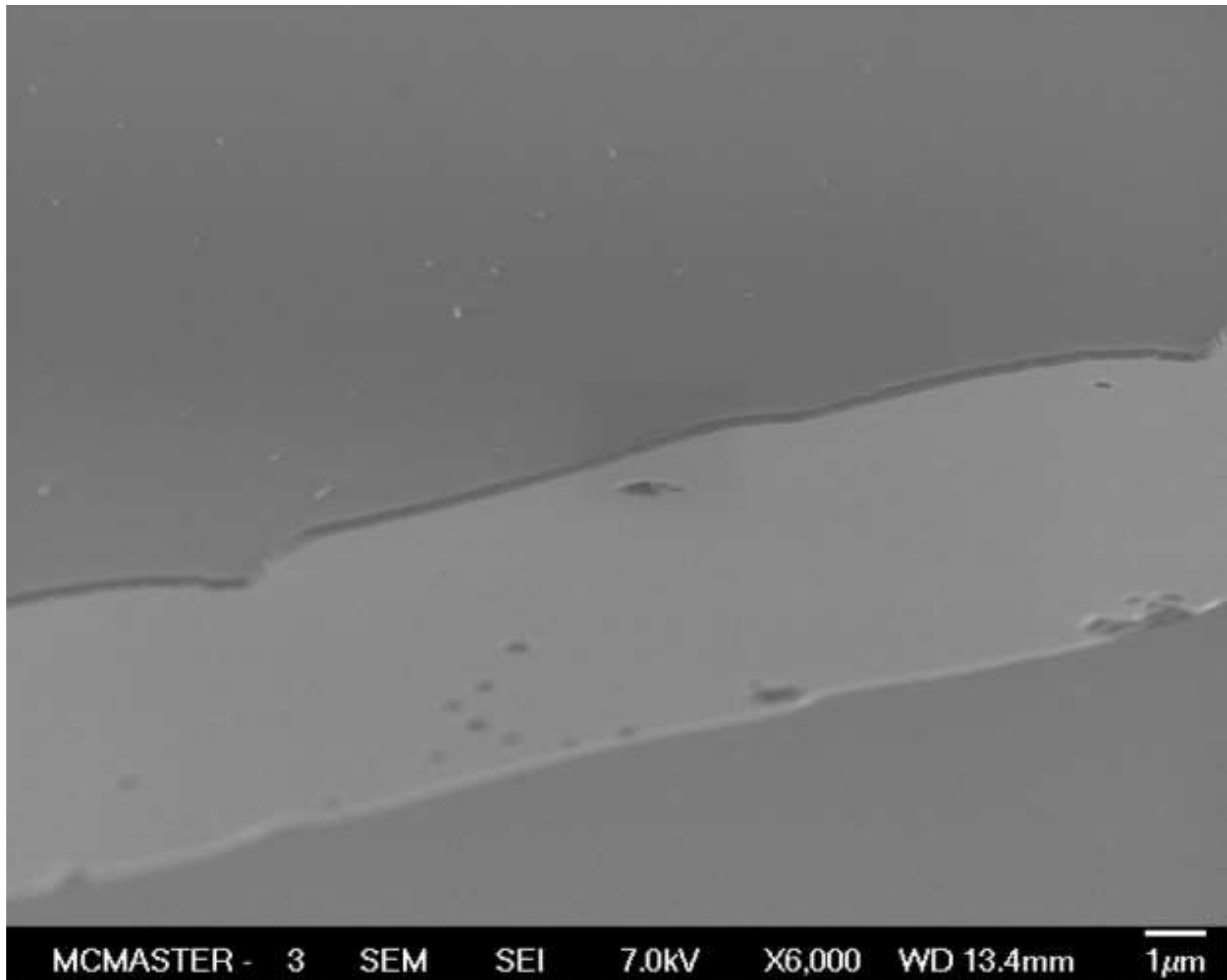

Figure 36: SEM Image of Quantum-Well Laser Cavity Surrounded by Silica Masking on GaAs Substrate (S-34)

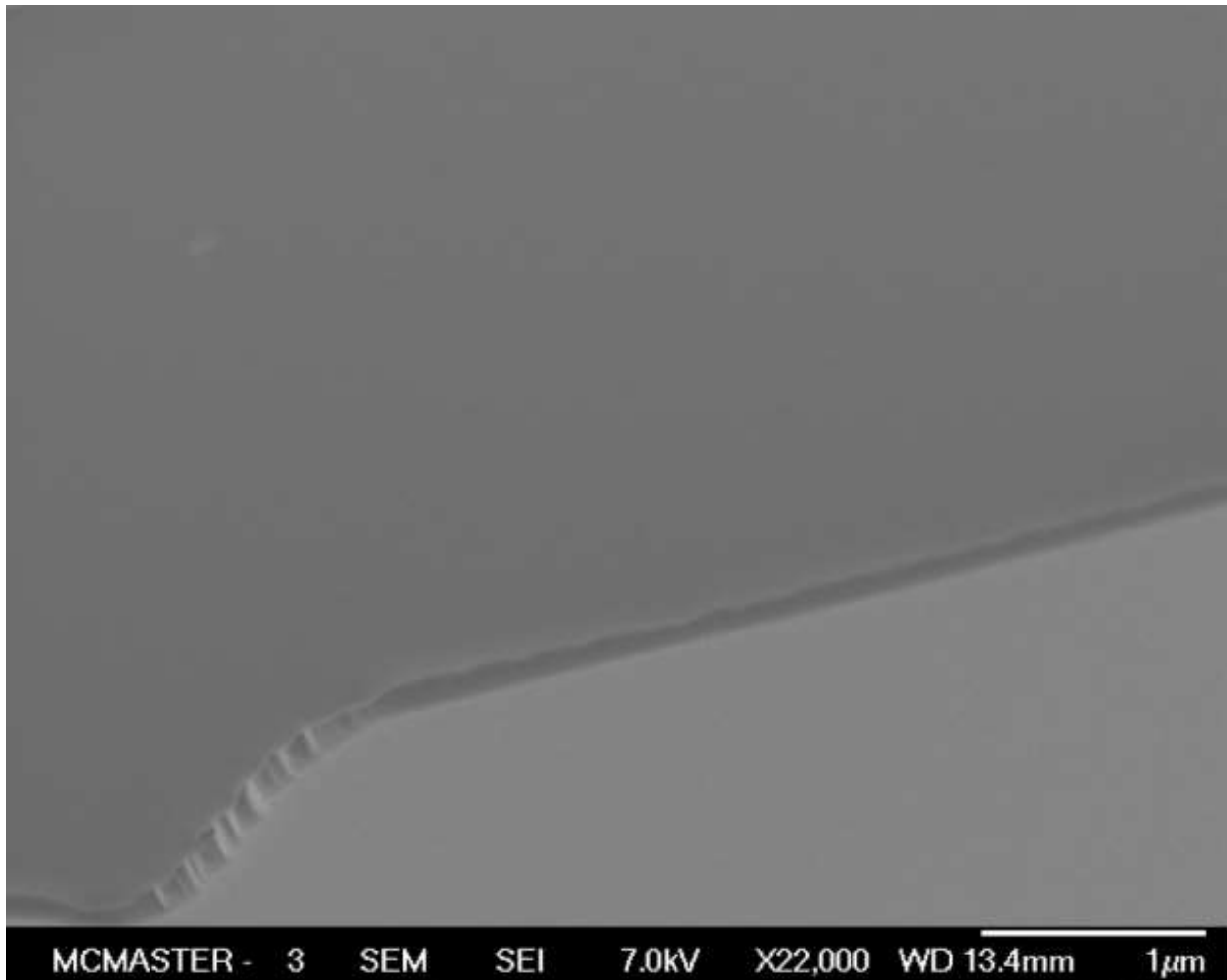

Figure 37: SEM Image of Quantum-Well Laser Cavity in the Vicinity of the Mask Edge on GaAs Substrate (S-34)

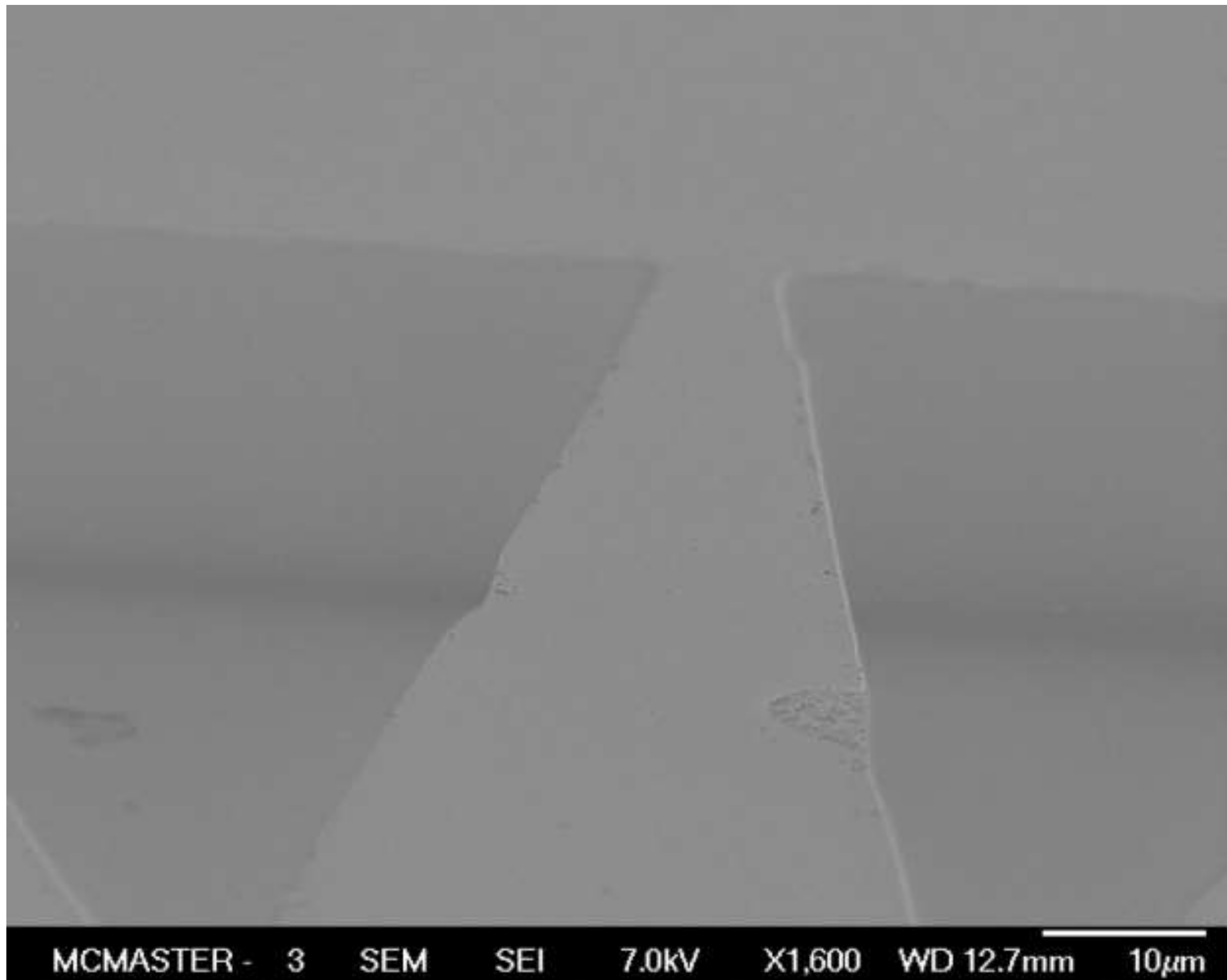

Figure 38: SEM Image Down the Quantum-Well Laser Cavity on GaAs Substrate (S-34)

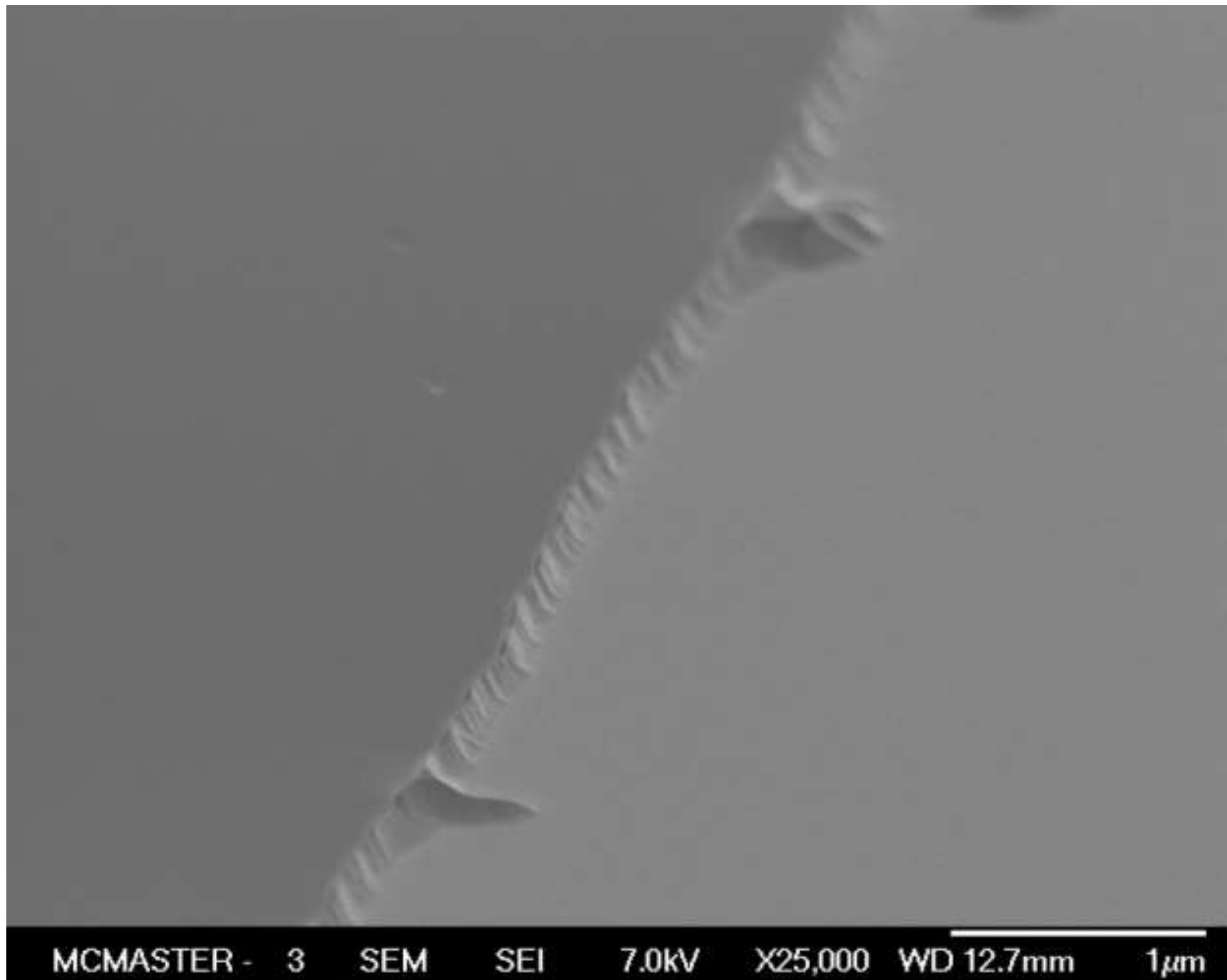

Figure 39: SEM Image of Mask Edge Defects on GaAs Substrate (S-34)

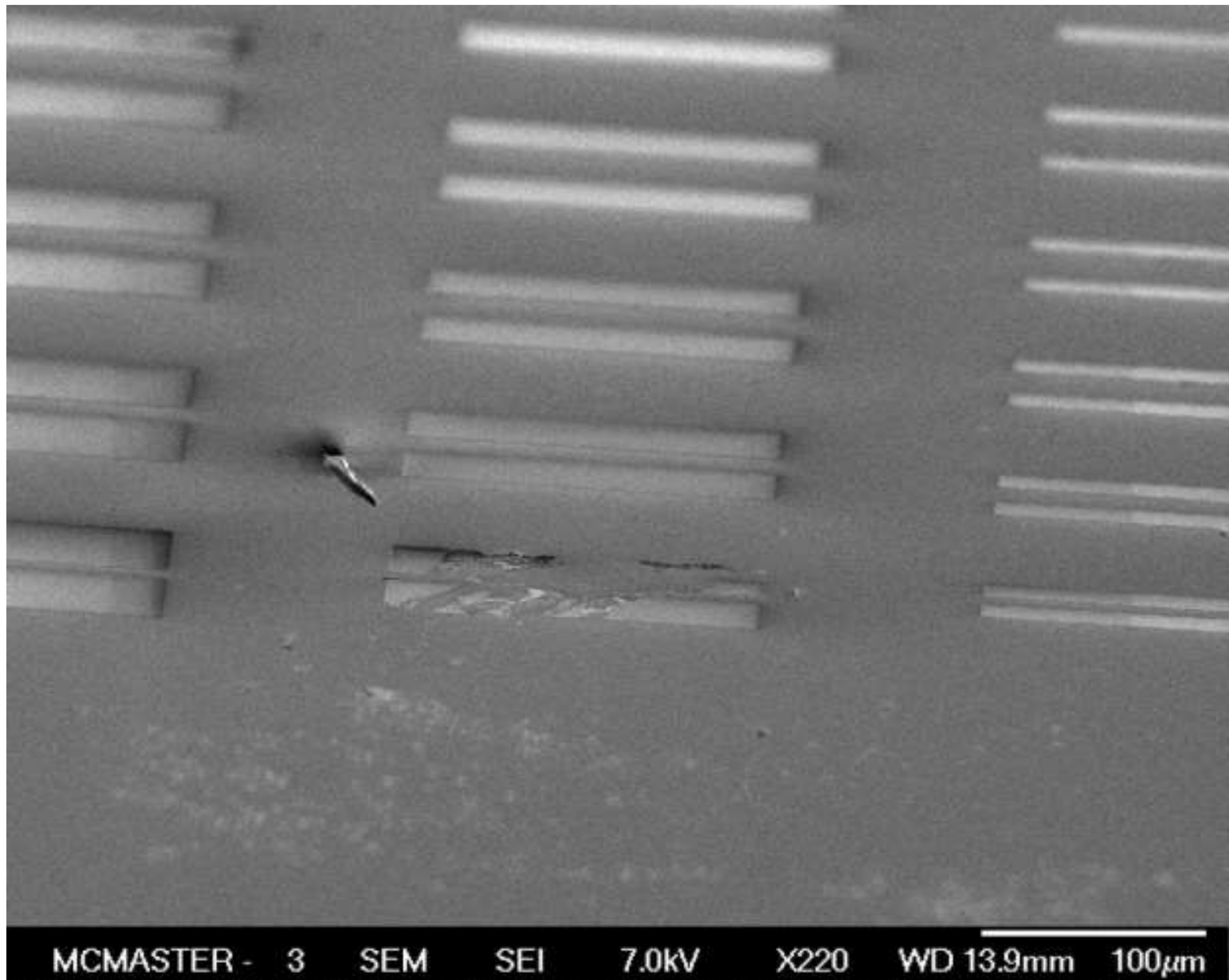

Figure 40: SEM Image of Silica Masking Structures on GaAs Substrate (S-34)

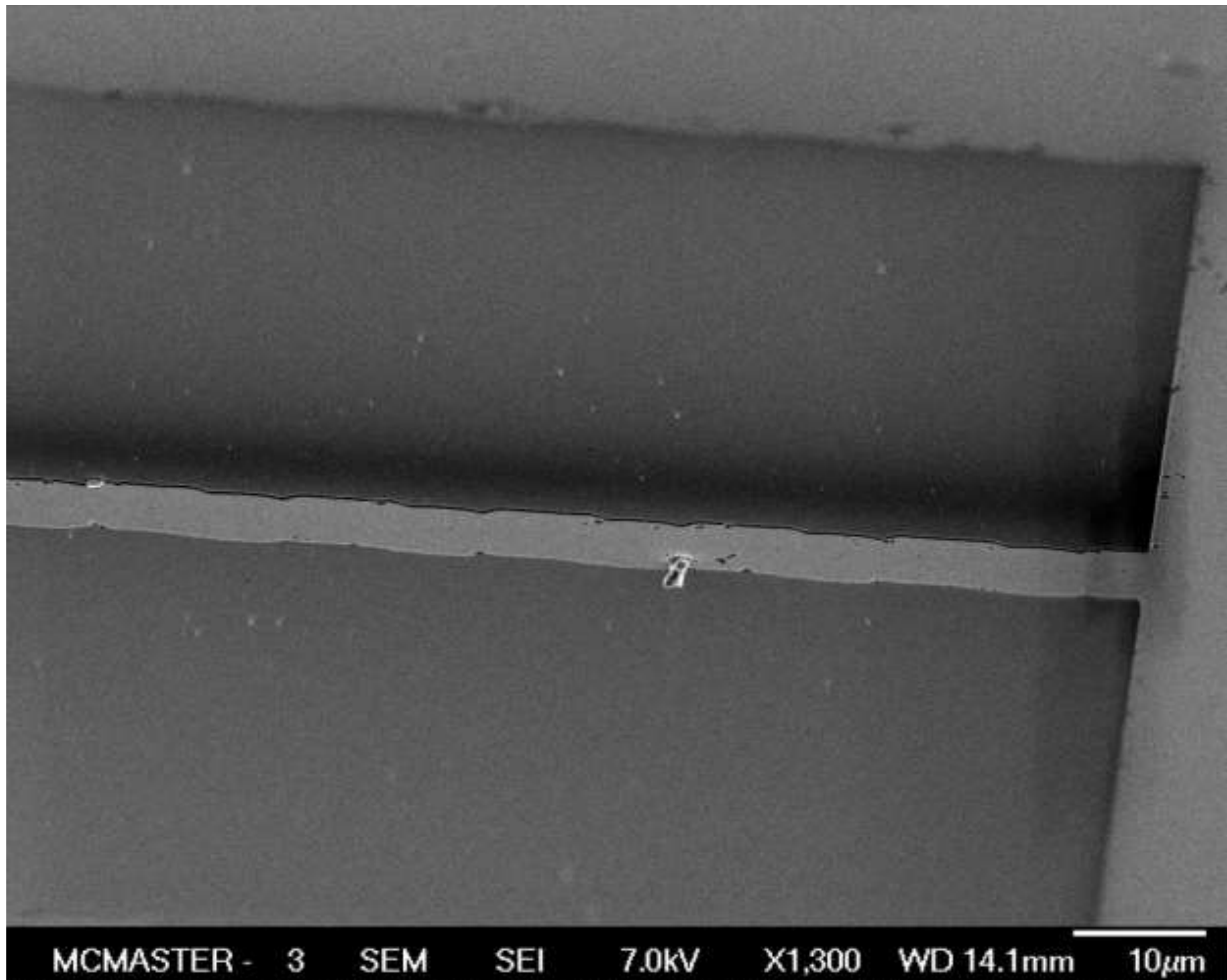

Figure 41: SEM Image of Silica Masking with High Contrast on GaAs Substrate (S-34)

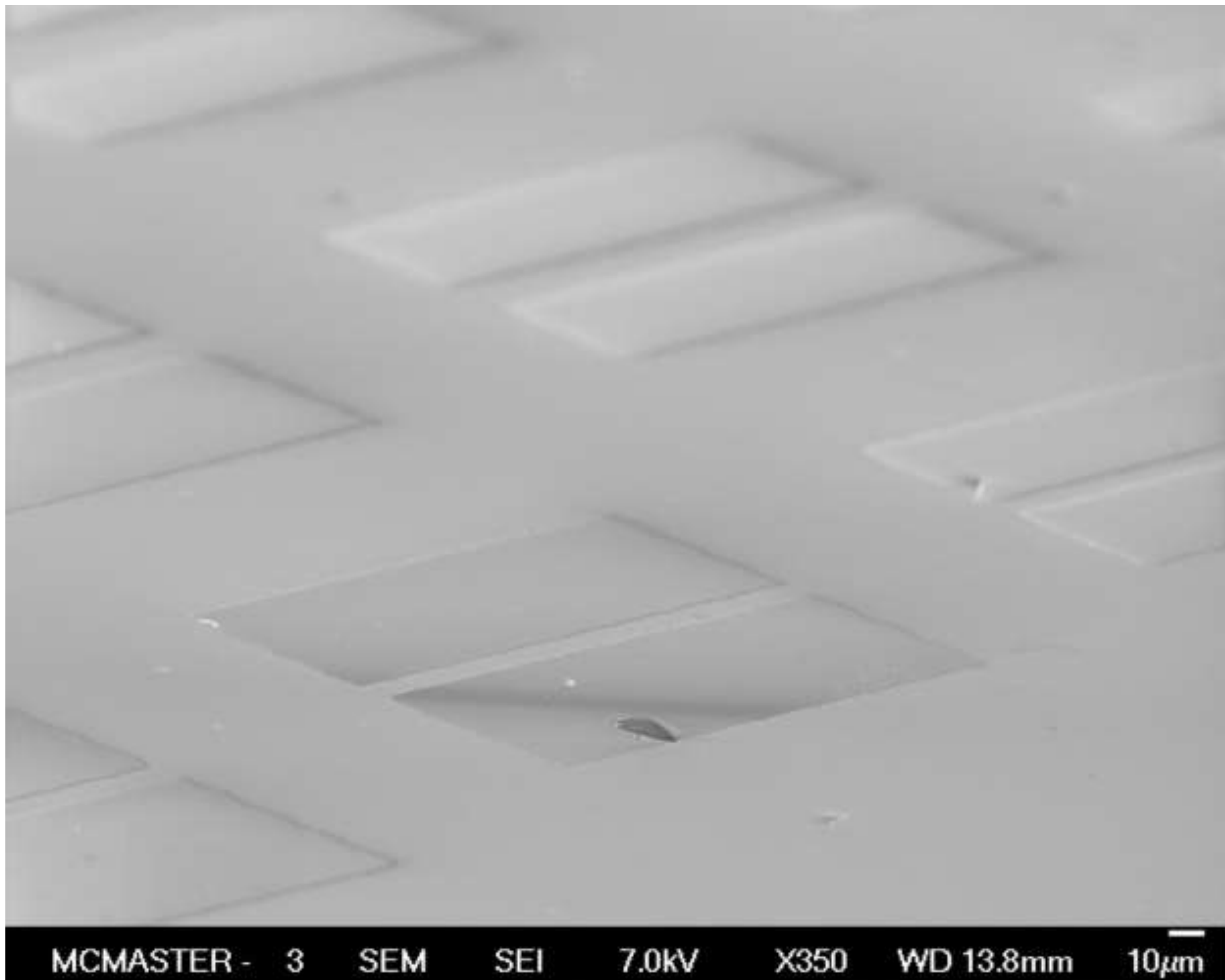

Figure 42: SEM Image of Silica Masking with Low Contrast on GaAs Substrate (S-34)

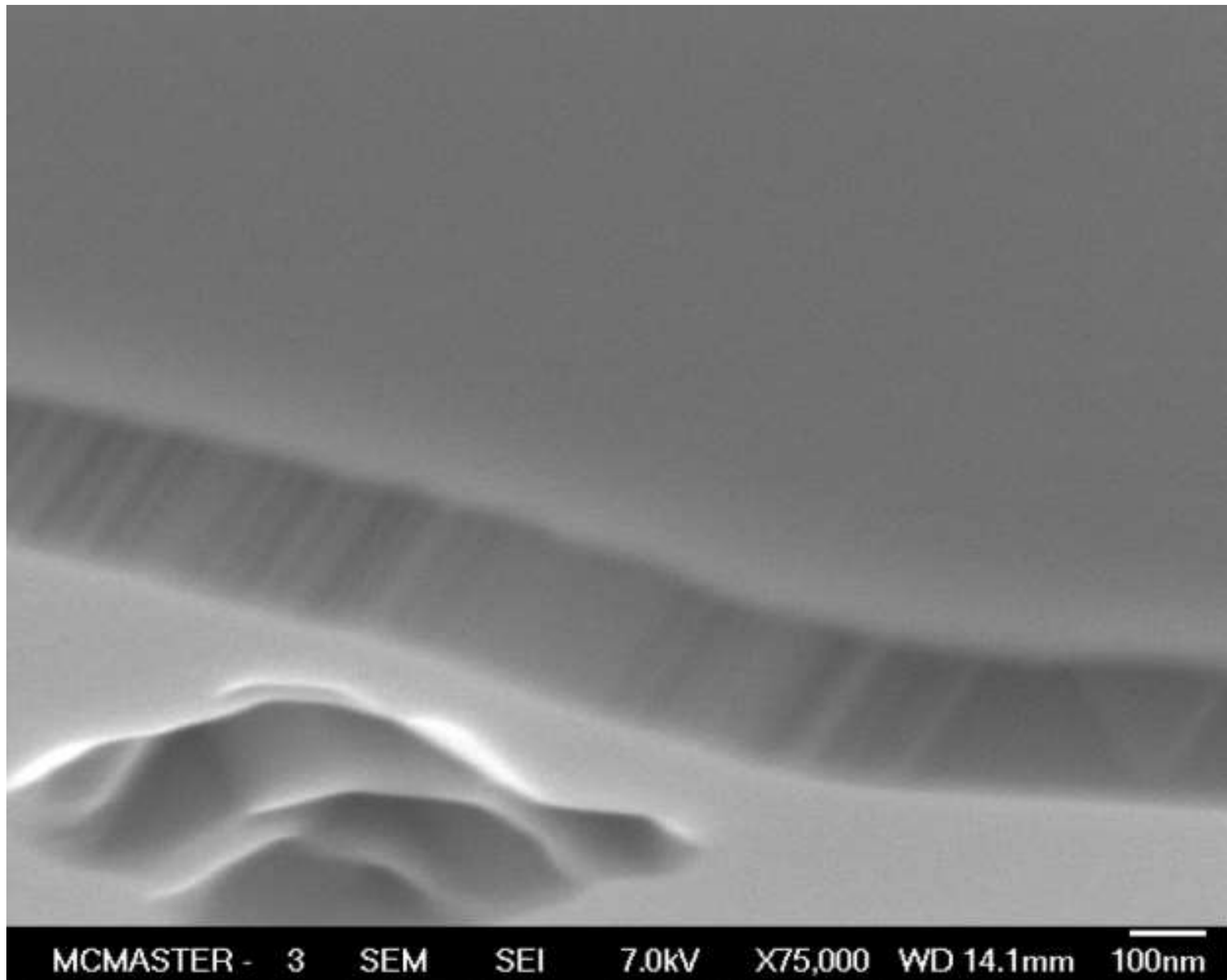

Figure 43: Closeup SEM Image of Mask Edge on GaAs Substrate (S-34)

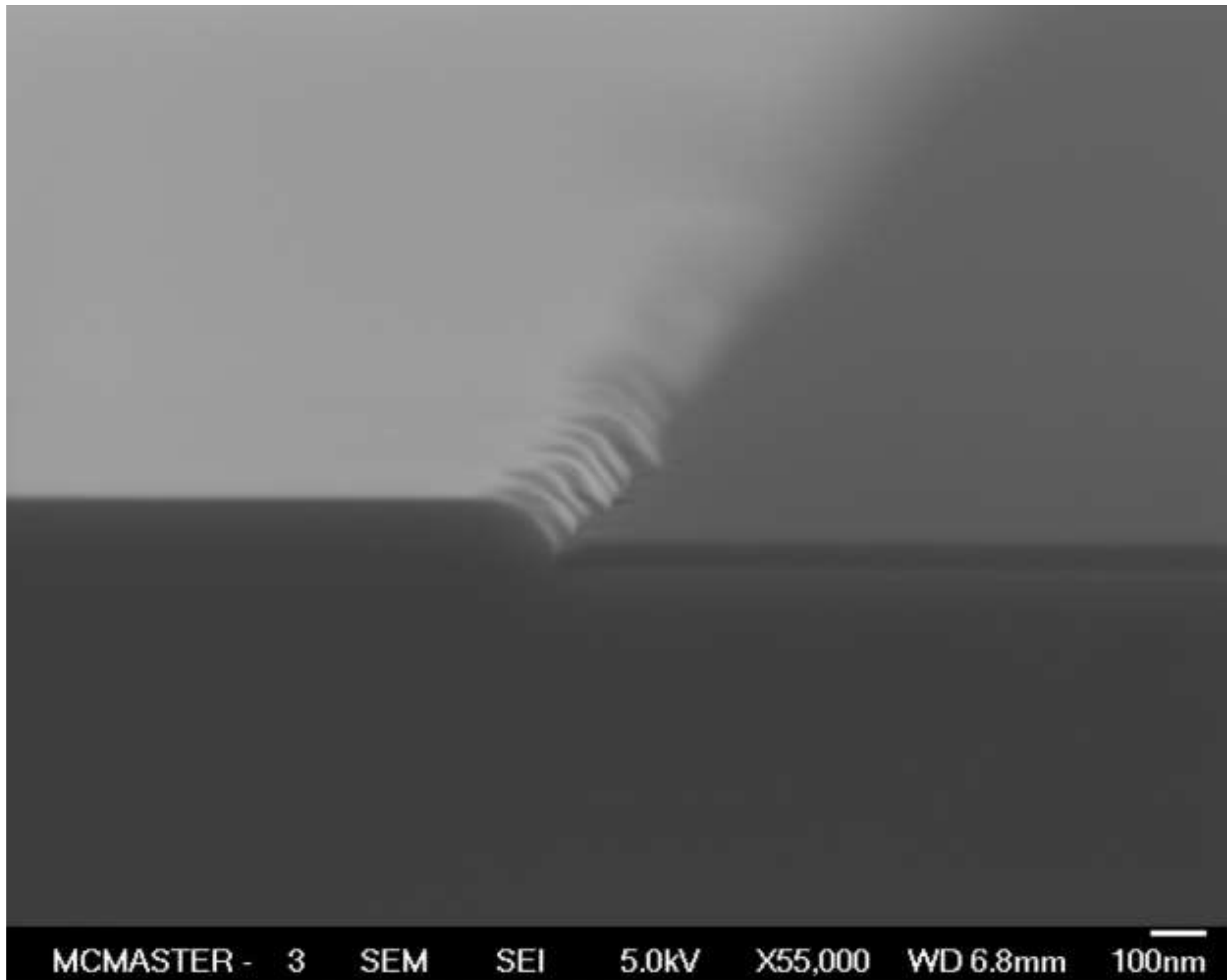

Figure 44: Cross-Sectional Image of Silica Mask (Dark) beside MOCVD Growth (Light) Demonstrating SAG (S-34)

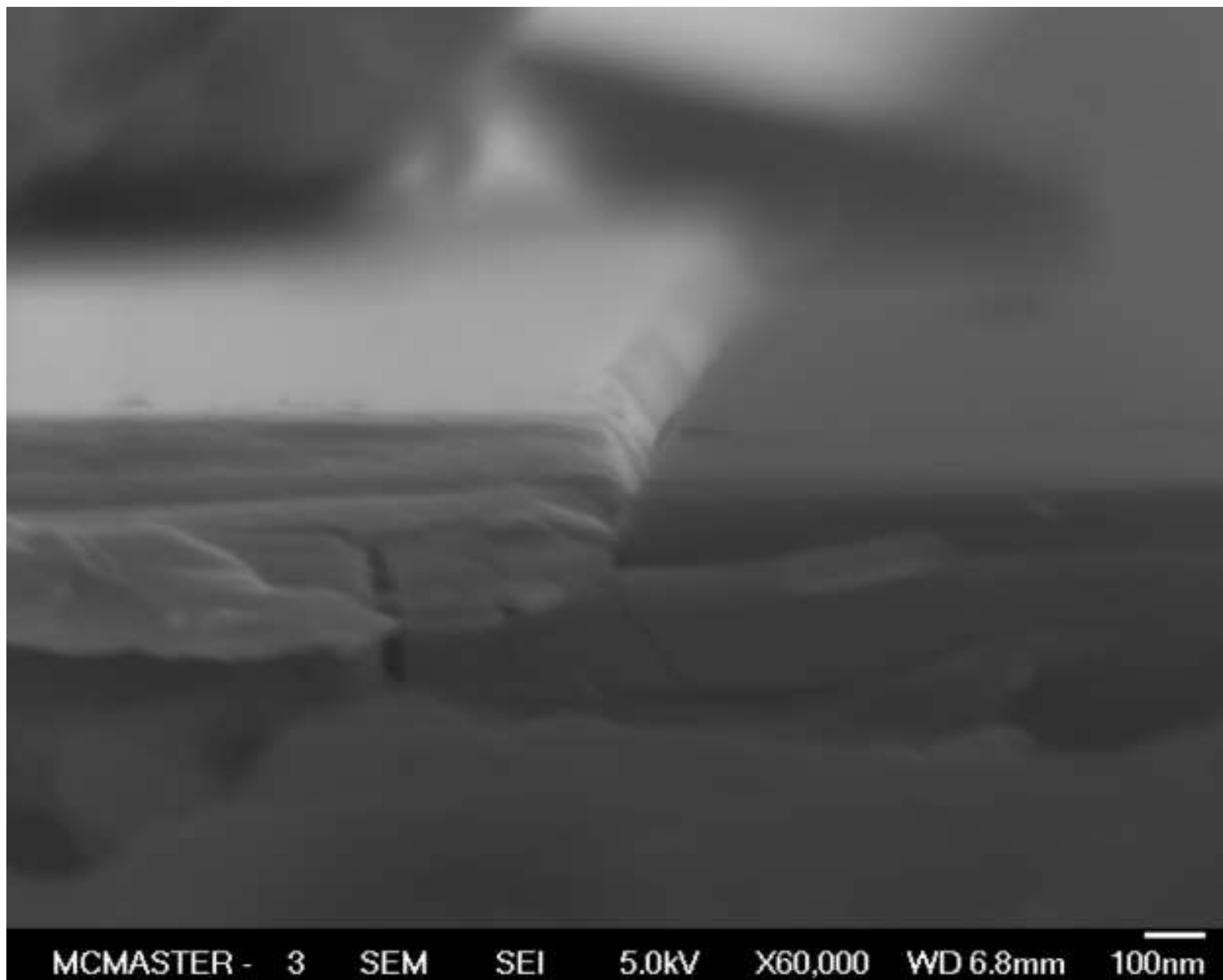

Figure 45: Closeup Cross-Sectional Image of Silica Mask (Dark) beside MOCVD Growth (Light) Demonstrating SAG (S-34)

4.1.2. Atomic Force Microscopy

The AFM process was utilized to analysis the quality of the growth mechanics. In Figure 46, S - 28 was analyzed and demonstrated precision in the layering of the MOCVD growth. This AFM image demonstrates the 2D layer growth of atomic terraces, with no surface hillocks or hexagonal pyramids, indicative of high-quality crystallographic order.

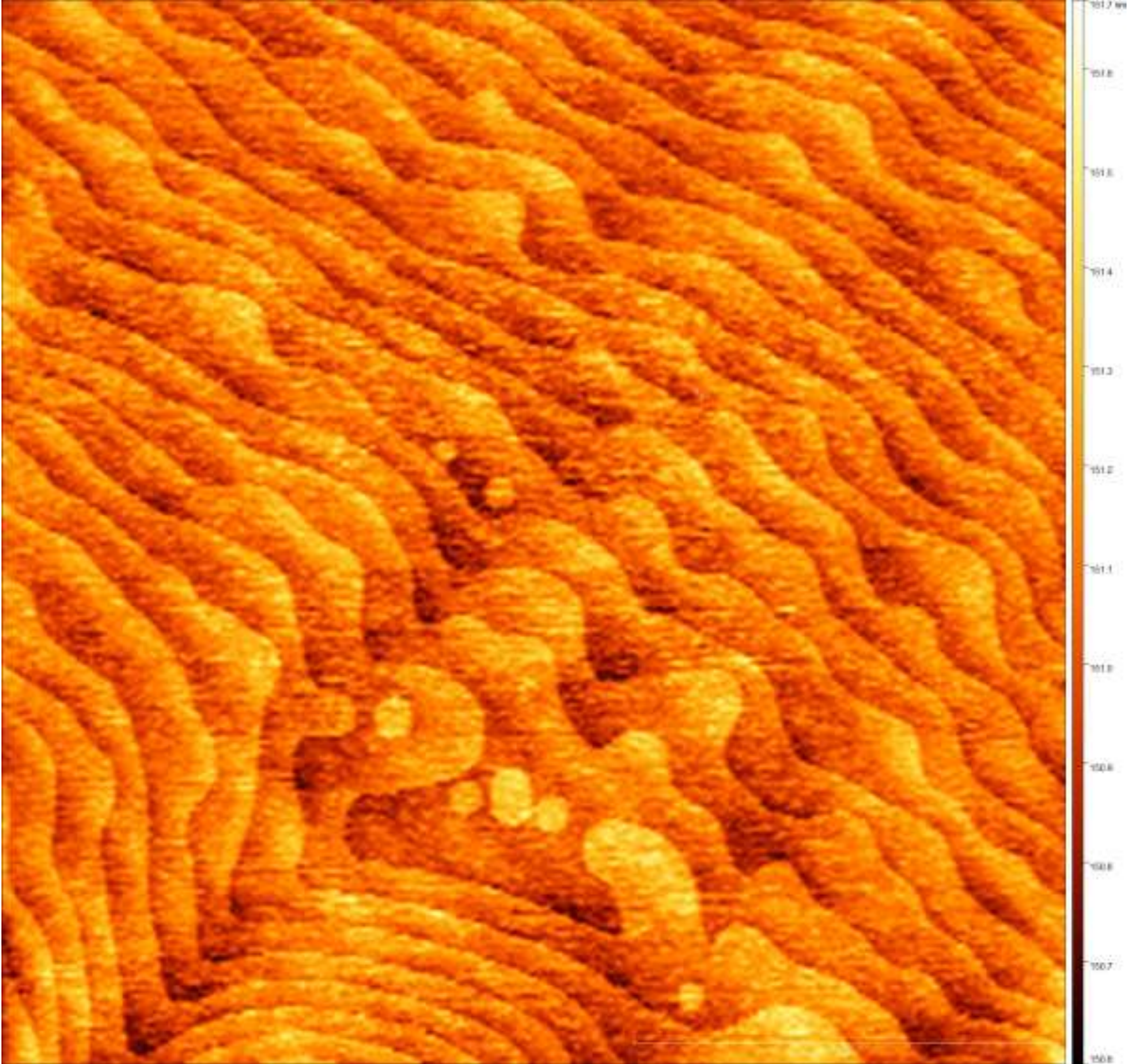

Figure 46: AFM Image of S-28 Surface - Atomic Terraces

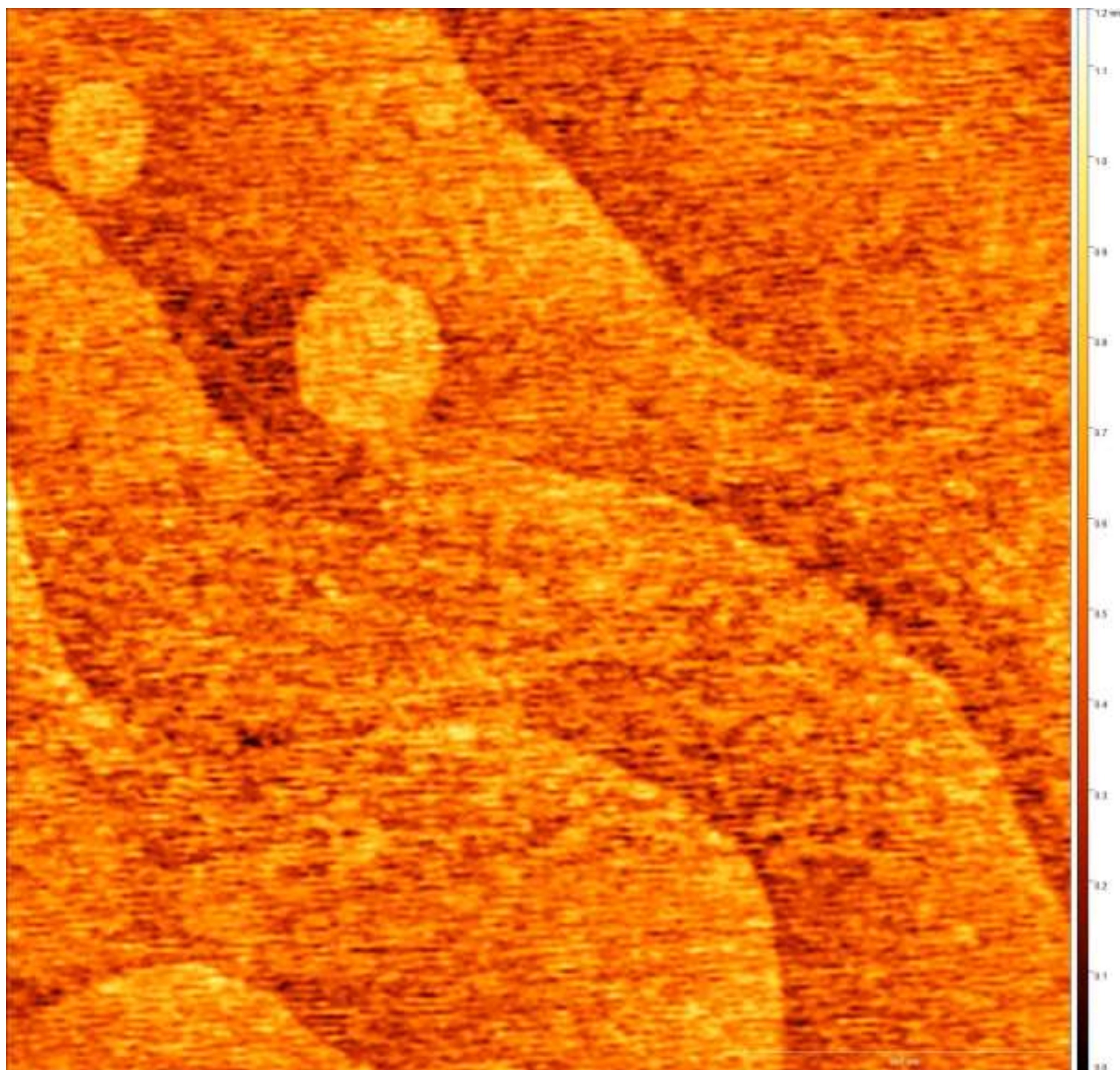

Figure 47: AFM Image Zoomed In on Atomic Terraces (S-28)

In Figures 48 and 49, sample S-34 was analyzed using a secondary AFM device. The AFM was not able to fully resolve the thickness of the MOCVD growth contribution. This process was completed by an experienced operator to explore the possibilities of topographic information for this sample and other samples in the future. The AFM procedure is a work in progress and will benefit the MOCVD parametric improvements while providing SAG quantitative thickness information.

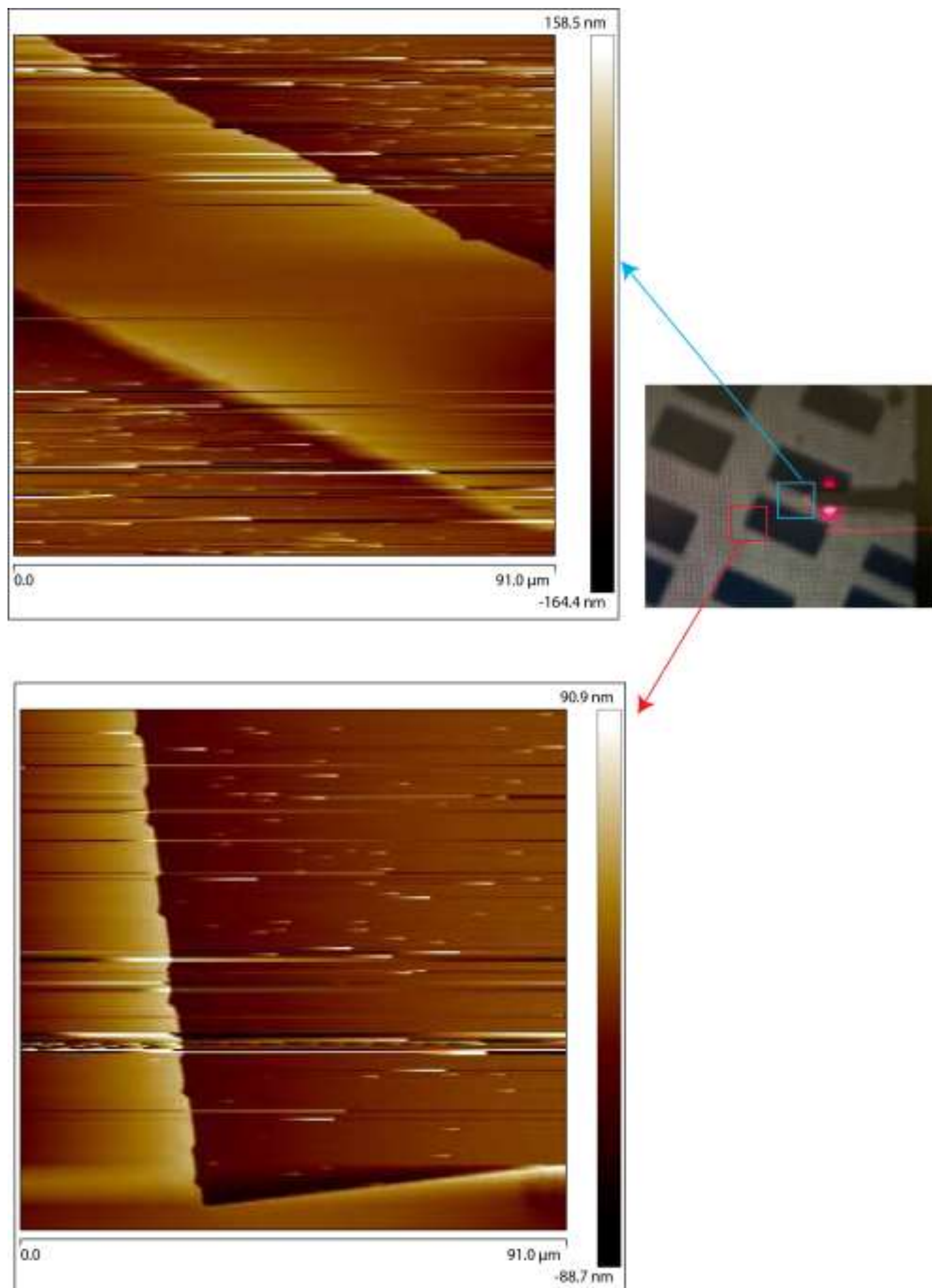

Figure 48: AFM Image of Silica Masking (Dark) beside MOCVD Growth (Light) (S-34)

Flatten Image View Analysis of 'dave.0_00000.spm'

Capture File Date: July 20, 2021
Image Note:

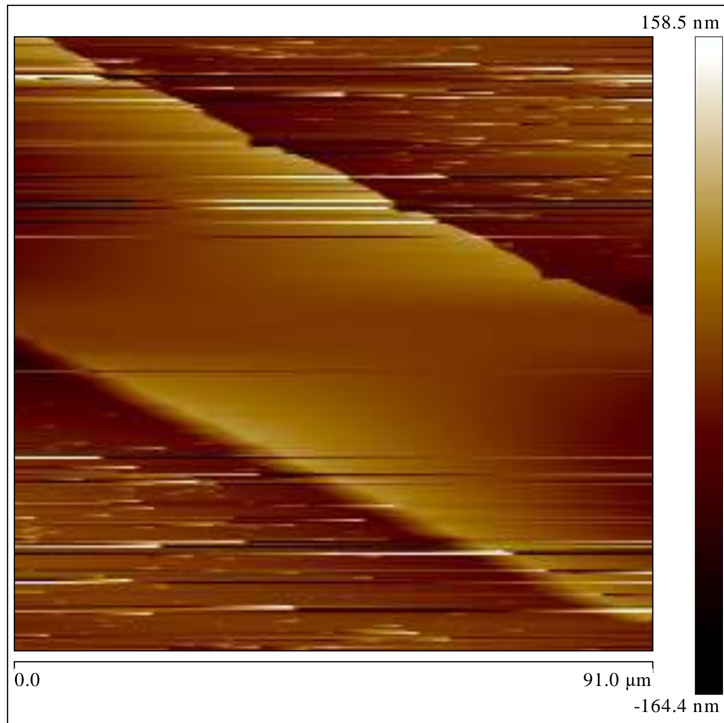

Inputs	
Flatten Order	1st
Flatten Z Threshholding Direction	No thresholding
Find Threshold for	the whole image
Mark Excluded Data	No
Number Histogram Bins	512
Threshold Height	0.00000 nm
Use Histogram	Off

Page 1 of 1

Figure 49: AFM Image of Laser Cavity (S-34)

4.2. Photoluminescence

The quantum-well samples were tested with a μ-P system in the AN Bourns Science Building measured at room temperature (298 K). This was completed to provide a quantum-well photoluminescence shape for calibration for the recently developed CEDT system. S-28 (Figure 50) did not show any quantum-well photoluminescence that is expected at ~950nm. The GaAs substrate does provide photoluminescence at 870 nm, a baseline photoluminescence consideration from the wavelength range evaluated. S-31 was able to resolve a quantum-well peak of photoluminescence at 949 nm (Figure 51). S-32 (S-34 equivalent) demonstrated a similar quantum-well peak at 985 nm. As shown below in Figure 52, this peak is considerably stronger than that of the S-31.

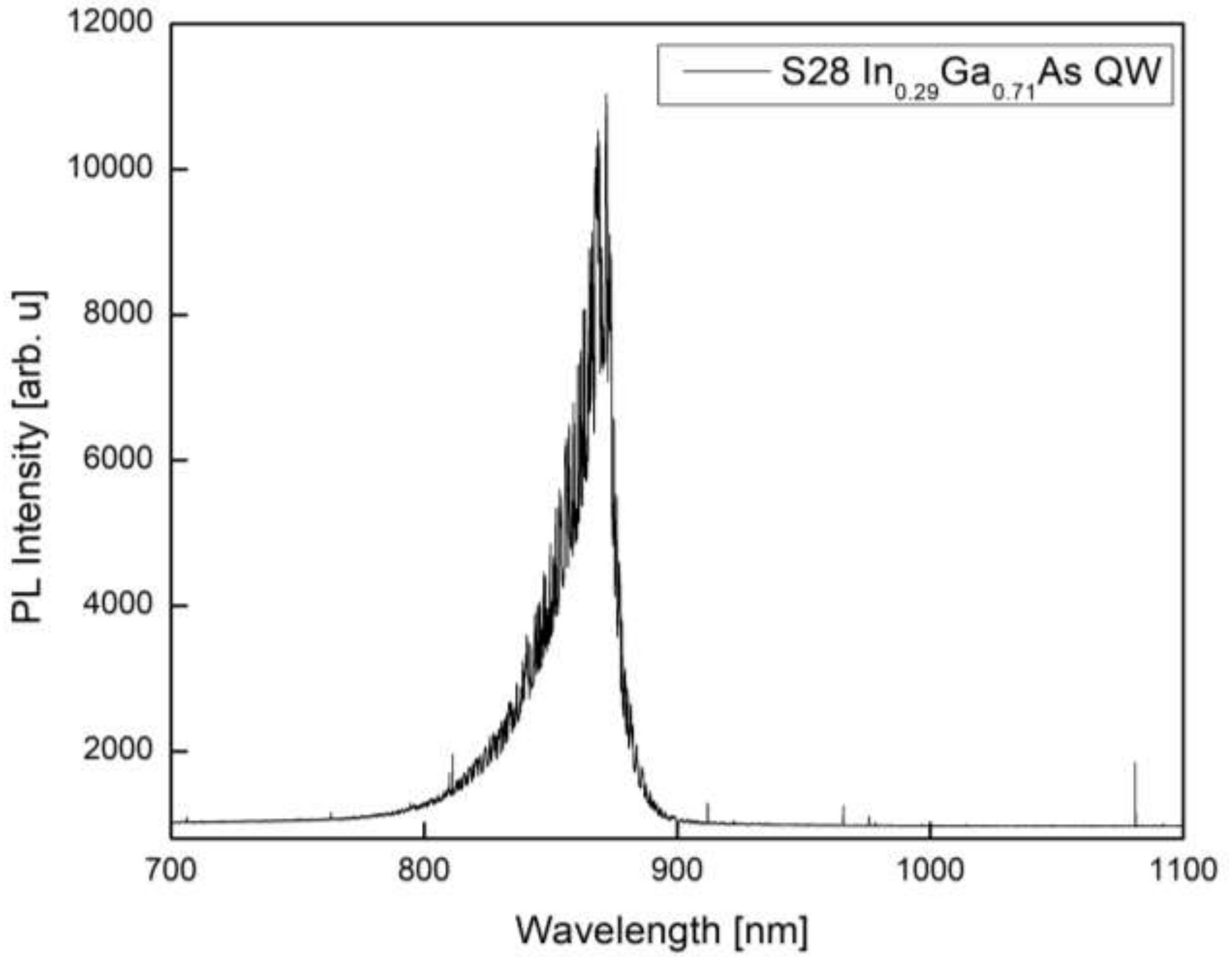

Figure 50: S-28 Photoluminescence Output with AN Bourns Science Building Photoluminescence System at Room Temperature

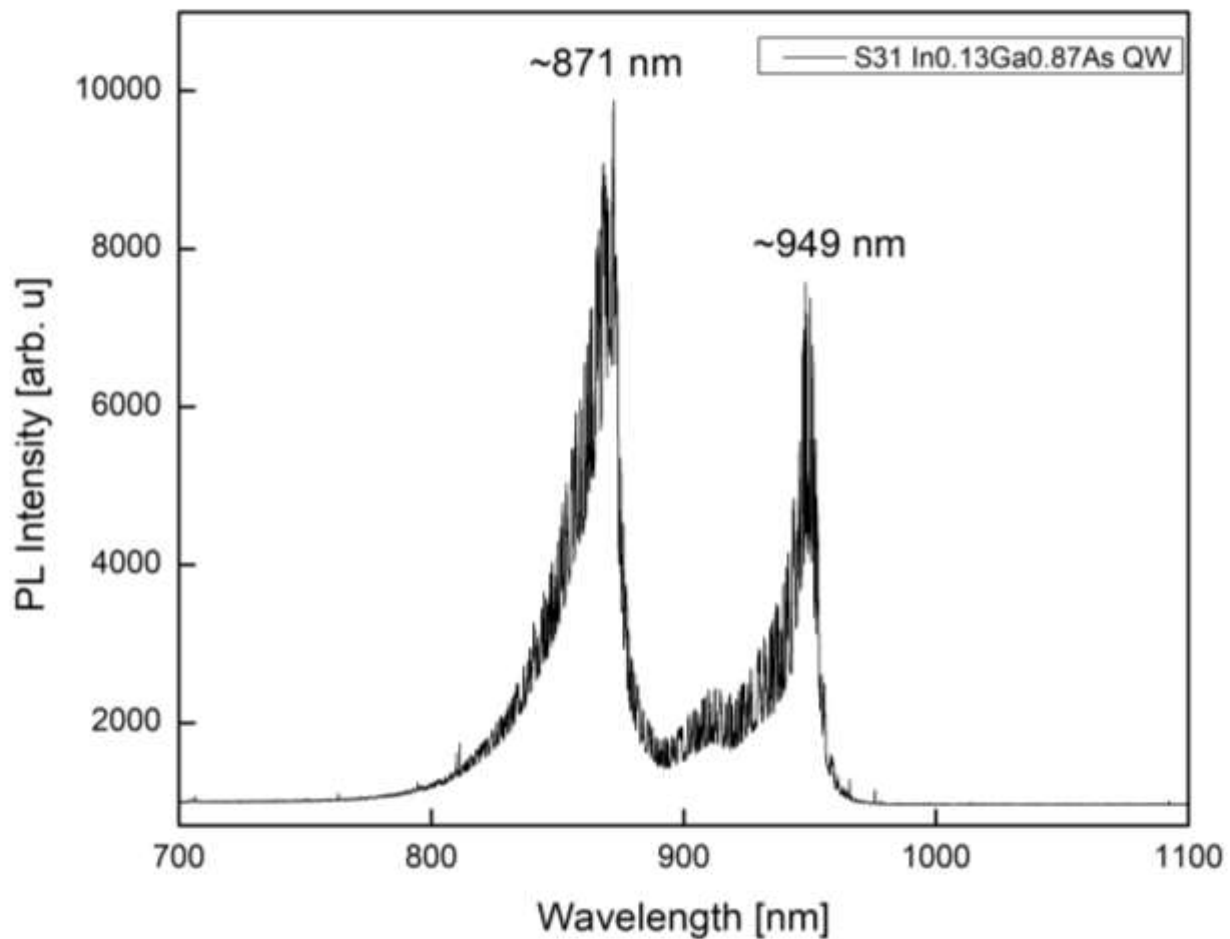

Figure 51: S-31 Photoluminescence Output with AN Bourns Science Building Photoluminescence System at Room Temperature

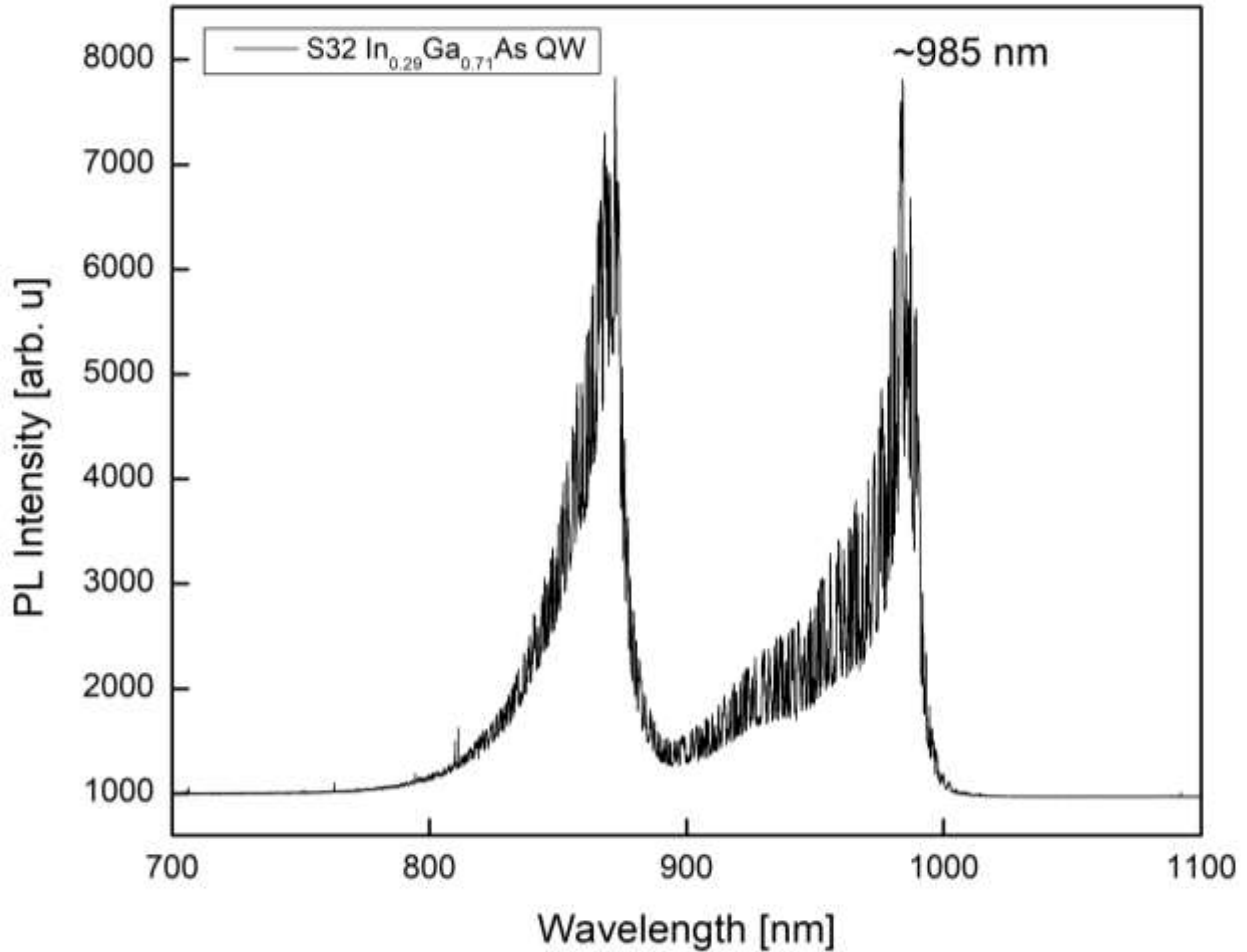

Figure 52: S-32 Photoluminescence Output with AN Bourns Science Building Photoluminescence System at Room Temperature

The externally supplied photoluminescence data provides considerable understanding of expectations for our μ-PL system. The samples S-31/S-32 were loaded into the sample holder and the system was operated with the exact same setup as the calibration of sample X. It was evident from the initial photoluminescence data that the quantum-well peak was not resolved. This is shown below with S-31 and S-32, in which adjustment of sensitivity and detector could not distinguish a quantum-well emission (Figures 56/57).

It was hypothesized that the photoluminescence from the quantum-well was simply too weak to resolve. Improvements in the system were made to compensate for misalignment possibilities while action was taken to increase the rigidity and robustness of the mirrors and lenses, additionally removing the camera and beamsplitter to increase input power was completed. Unfortunately, the quantum-well peak was still not resolved. It was then theorized that an issue may be occurring with the detector input at a high frequency of 100 kHz. The entire laser system was replaced with a HeNe 632.8 nm laser directed through a chopper mechanism at 100 Hz (Figure 53). The setup was otherwise unchanged (Figure 54), while the chopper was connected to the lock-in amplifier.

The quantum-well photoluminescence, however, was not resolved with this change of laser output wavelength and frequency. It is now hypothesized that the issue may be the monochromator. The monochromator is responsible for the filtering of the photoluminescence from the sample to the detector. It has been shown in Figure 57 that the substrate photoluminescence of GaAs can be detected accordingly and when cross referenced to Figure 52, we should expect a similar threshold for the quantum-well peak at ~985 nm. If the system operation was nearly laser and frequency independent, it can be expected that the operational issue lies with the monochromator filtering in the 900 nm – 1000 nm range.

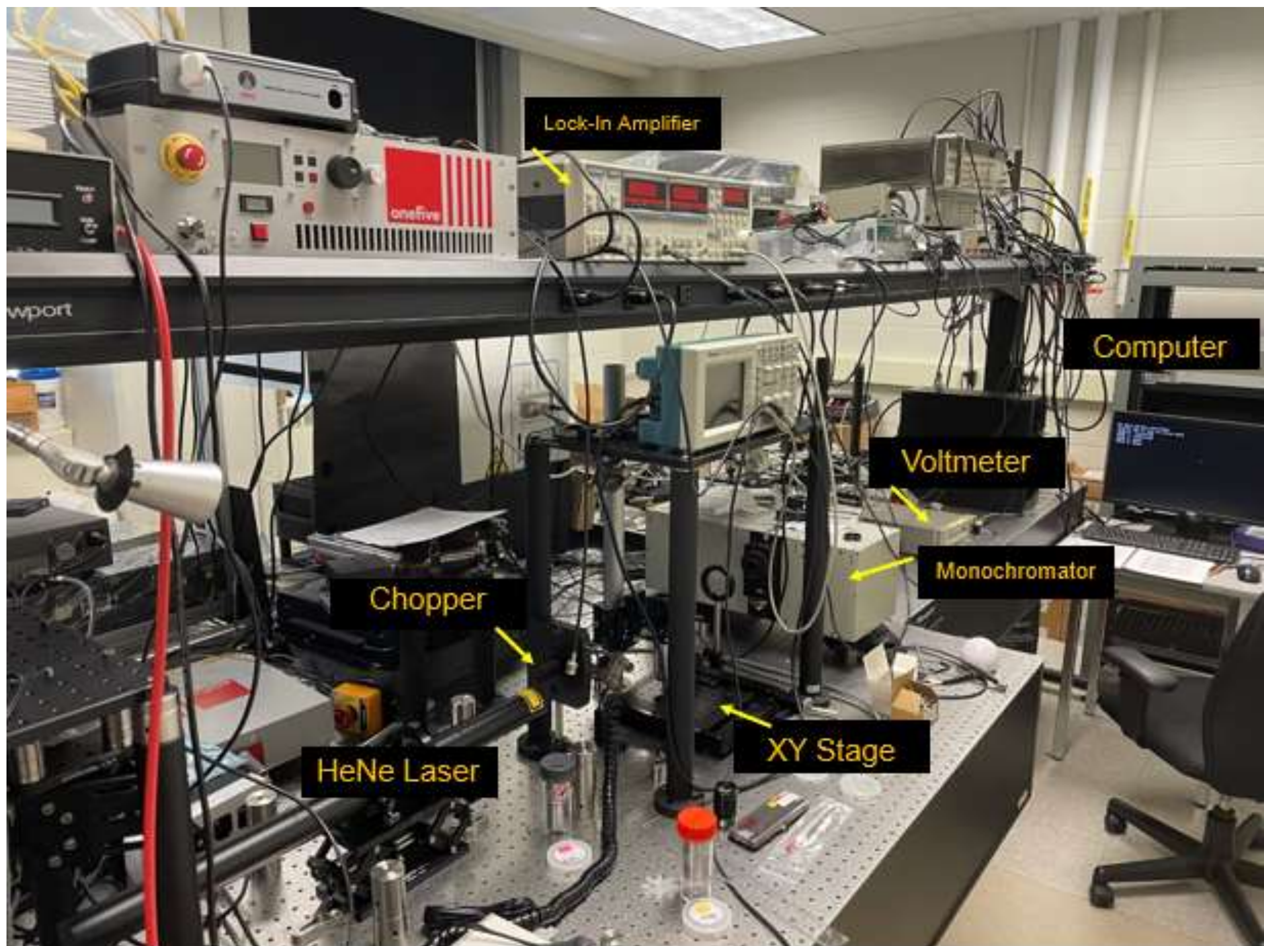

Figure 53: HeNe Photoluminescence Setup

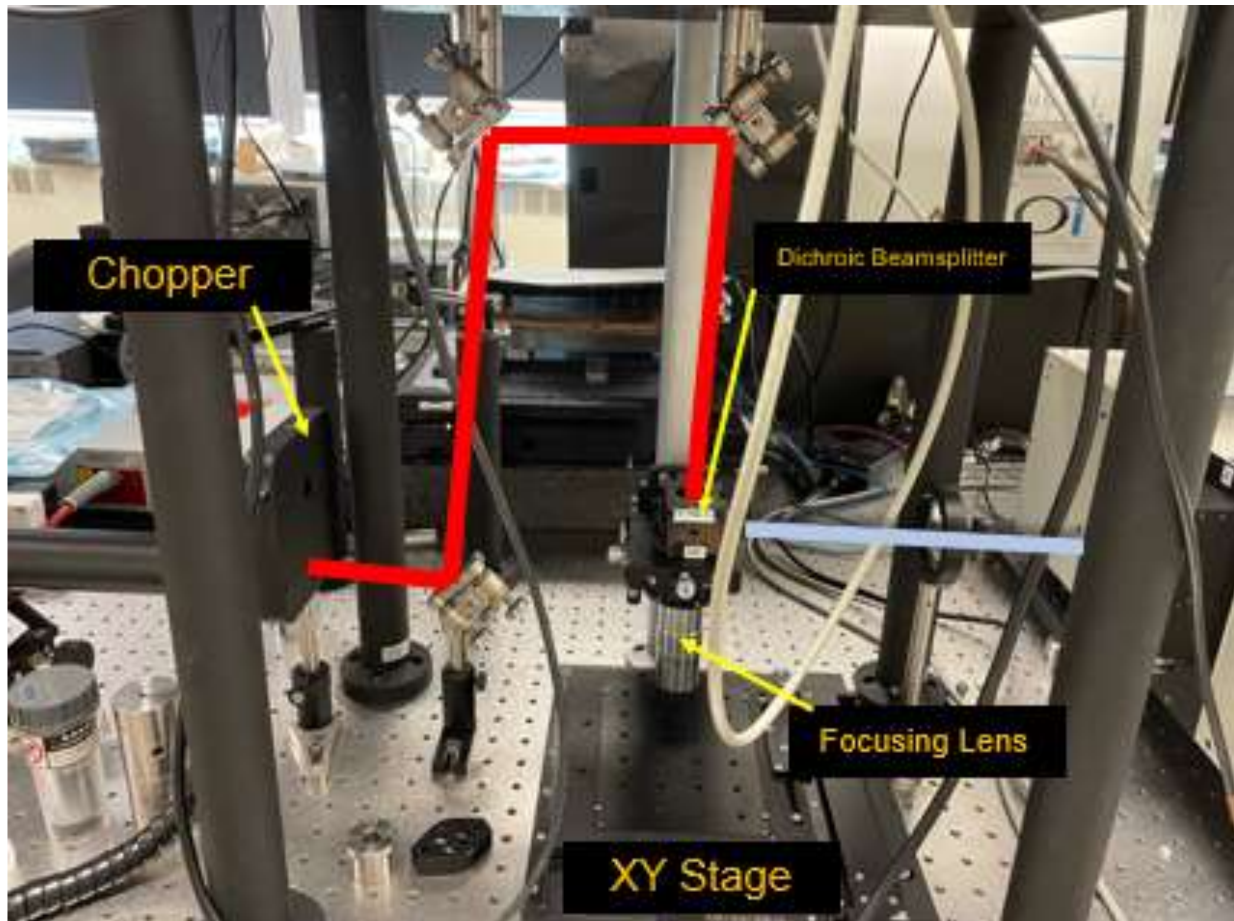

Figure 54: HeNe Chopper Mechanism Leading to Division of Photoluminescence Output by Dichroic Beamsplitter

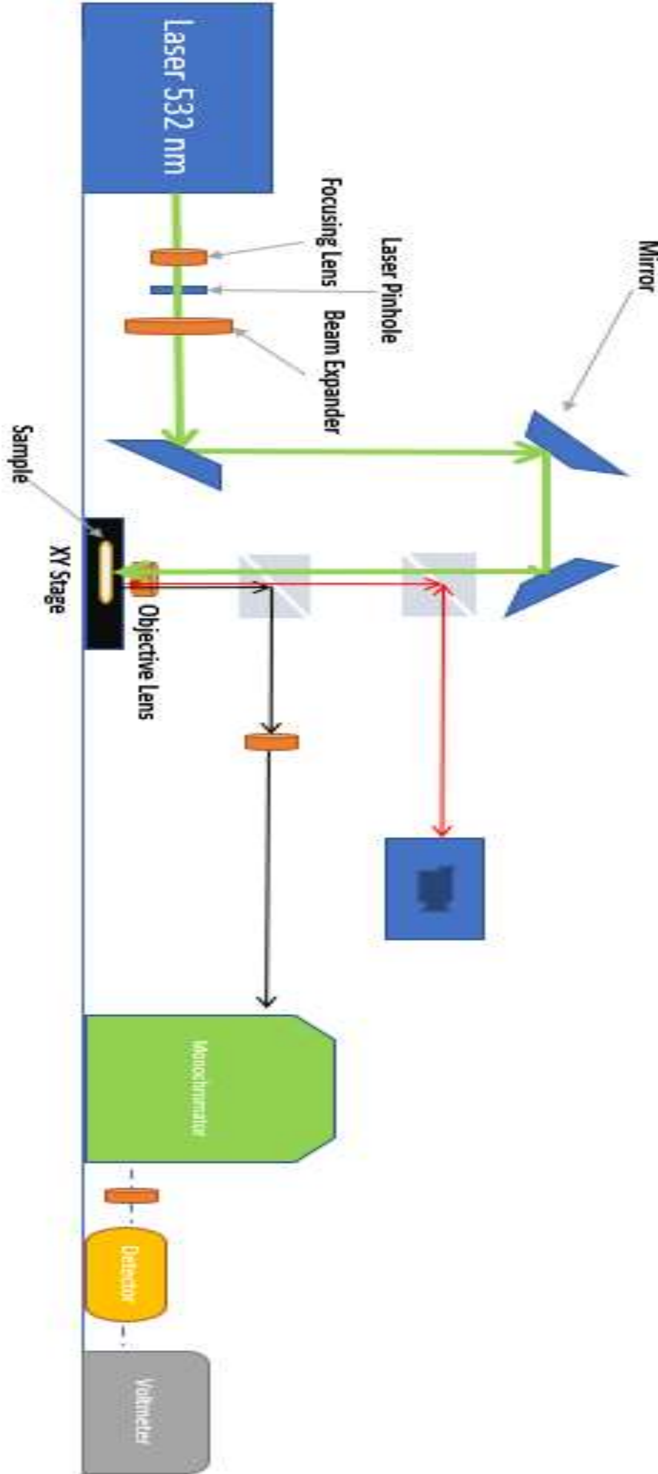
Laser 532 nm
Focusing Lens
Laser Pinhole
Beam Expander
Mirror
Sample
XY Stage
Objective Lens
Monochromator
Detector
Voltmeter

Figure 55: Schematic of μ-PL System

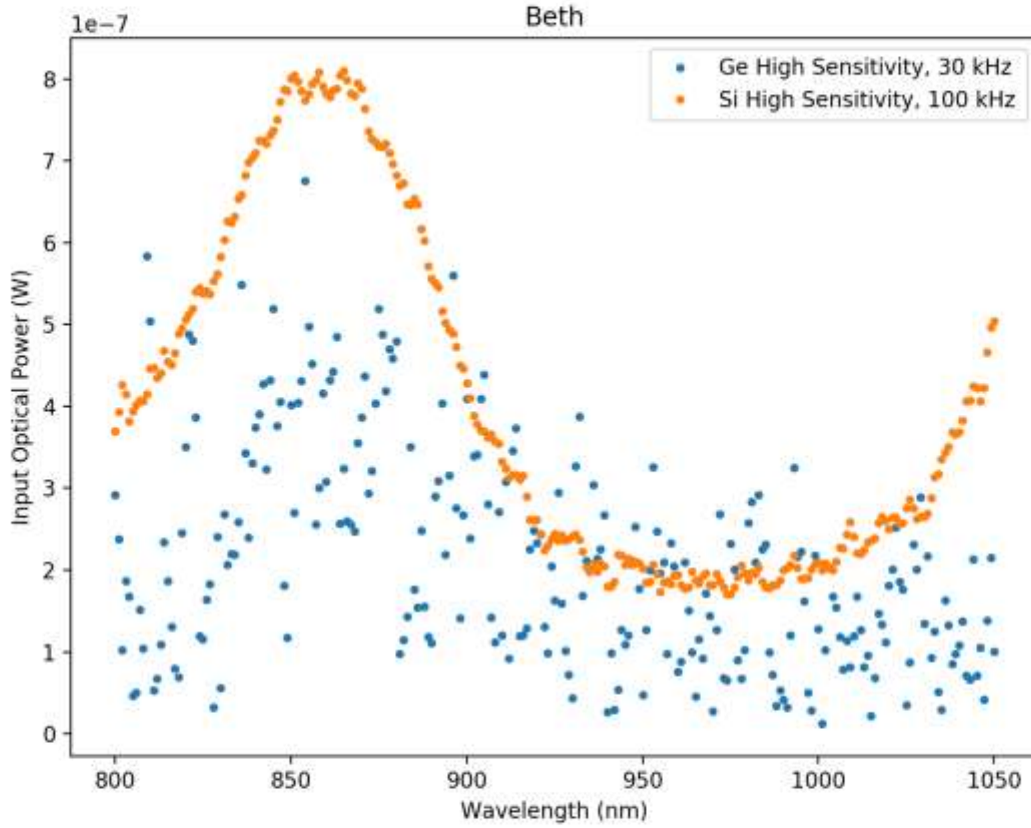

Figure 56: Photoluminescence Output using New Setup (HeNe with Chopper Mechanism) for S-31 with Germanium and Silicon Photodetectors

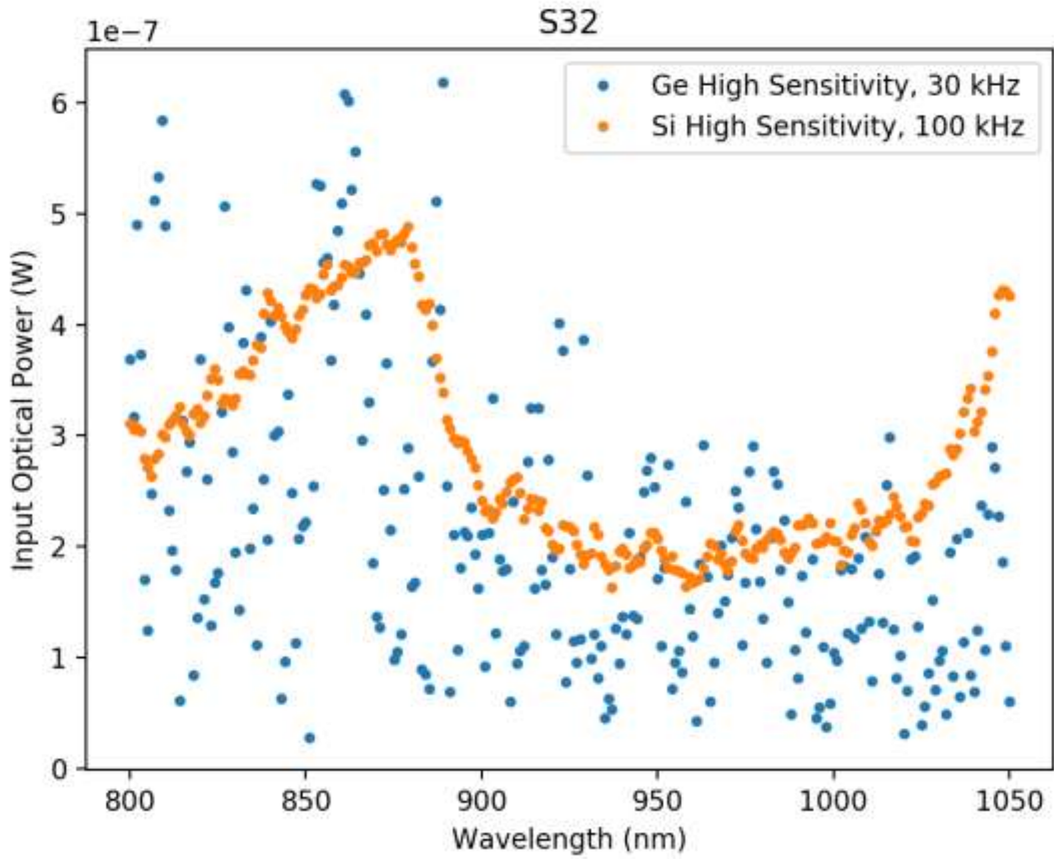

Figure 57: Photoluminescence Output using New Setup (HeNe with Chopper Mechanism) for S-32 with Germanium and Silicon Photodetectors

5. Conclusion

5.1. Conclusion

The MOCVD system at McMaster University is fully operational with daily improvements to growth parametric control. This is made possible by a robust characterization procedure for continuous advancement. The SAG recipe was generated through cleanroom troubleshooting and fabrication experimentation developing into a standardized recipe for silica 3-dimensional rectangular prisms. The laser direct pattern writing technique was developed for consistent resilience of channel etching. Additionally, standard operating procedures were solidified during the process of CVD for the CEDT.

A μ-PL system with translational spatial resolution was established with resourcefulness and creativity. A meticulous creation benefitting a plethora of graduate students to test their photoluminescent devices/substrates. This device system when fully completed will possess the capabilities for imaging of the laser beam spot's relative location and size. The μ-PL system can be adapted with dichroic filtering and laser wavelength emission variations if necessary. Photoluminescence traverses a multitude of disciplines within the scientific community, reflecting the importance of this automated resource for all.

The future of MOCVD SAG is one of optimism at McMaster University, with a truly diverse set of epitaxial growth options and experts to drive the innovation forward. This project is simply a stepping-stone for subsequent novelty and imagination of semiconductor manufacturing.

5.2. Future Work

Immediate changes and calibration are needed for the monochromator system to resolve the quantum-well emission. With emission spectra quality of high standing, the μ-PL system can be used for MOCVD daily calibration. The SAG growth can also be analyzed with minor improvements to the camera system. The characterization methodology must be collaboratively decided upon for team transparency and repeatability. Several samples were only partially characterized consequently providing many unnecessary, equivalency assumptions to be made.

Moving forward, SAG with AlGaInAs compounds on InP can be utilized for telecom applications. Several alterations to SAG mask thickness, spacing and feature sizing will be explored in the near future.

6. References

[1] G.E. Moore, “Cramming more components onto integrated circuits,” Electronics, vol. 38, no.8, 1965.

[2] J. Shalf, “2020 The future of computing beyond Moore’s Law.” Phil. Trans. R. Soc, 30 Sept 2019.

[3] G. B. de Farias, M. A. G. Porcel, D. Domenech and I. Artundo, “How to Develop your product based on Photonic Integrated Circuits Technologies,” IEEE, 2021 SBFOTON International Optics and Photonics Conference (SBFOTON IOPC), pp. 1-3, 2021.

[4] M. Aoki, H. Sano, M. Suzuki, M. Takahashi, K. Uomi, A. Takai, “Novel structure MQW electroabsorption modulator/DFB-laser integrated device fabricated by selective area MOCVD growth”, Electron. Lett., 27, pp. 2138–2140, 1991.

[5] N. Dupuis et al, “Mask pattern interference in AlGaInAs selective area metal-organic vapor-phase epitaxy: Experimental and modeling analysis”, Journal of Applied Physics, 103, 2008.

[6] M. Sugiyama, “Selective area growth of III-V semiconductors: From fundamental aspects to device structures”, 22nd International Conference on Indium Phosphide and Related Materials (IPRM), 2010.

[7] J. Wing and M. Lundstrom, “Does source-to-drain tunnelling limit the ultimate scaling of MOSFETs?,” IEEE, pp. 707-710, 2002.

[8] Z. Alferov, “Double heterostructure lasers: early days and future perspectives,” IEEE Journal of Selected Topics in Quantum Electronics, vol. 6, no. 6, pp. 832-840, Dec 2000.

[9] Z. I. Alferov, V. B. Khalfin, and R. F. Kazarinov, “A characteristic feature of injection into heterojunctions,” Fiz. Tverd. Tela, vol. 8, pp. 3102–3105, 1966.

[10] H. Kroemer, “Theory of a wide-gap emitter for transistors,” Proc. IRE, vol. 45, p. 1535, 1957.

[11] D. T. Cheung and G. L. Pearson, “An analysis of the superinjection phenomenon in heterostructure devices,” Journal of Applied Physics, vol. 46, no. 5, 1975.

[12] D. Downs and T. E. Vandervelde, “Progress in Infrared Photodetectors Since 2000,” Pubmed, vol. 13, no. 4, pp. 5054-5098, 2013.

[13] Z. I. Alferov, V. M. Andreev, V. I. Korol’kov, D. N. Tret’ya-kov, and V. M. Tuchkevich, “High-voltage p-n junctions in Ga Al As crystalls,” Fiz. Tekh. Poluprovodn., vol. 1, pp. 1579–1581, 1967.

[14] Z. I. Alferov, V. M. Andreev, E. L. Portnoy, and M. K. Trukan, “AlAs–GaAs heterojunction injection lasers with a low room-temperature threshold,” Fiz. Tekh. Poluprovodn., vol. 3, pp. 1328–1332, 1969.

[15] Z. I. Alferov, V. M. Andreev, V. I. Korol’kov, E. L. Portnoi, and A. A. Yakovenko, “Spontaneous radiation sources based on structures with AlAs–GaAs heterojunctions,” Fiz. Tekh. Poluprovodn., vol. 3, pp. 930–933, 1969.

[16] Z. I. Alferov, V. M. Andreev, M. B. Kagan, I. I. Protasov, and V. G. Trofim, “Solar-energy converters based on p-n Al Ga As–GaAs heterojunctions,” Fiz. Tekh. Poluprovodn., vol. 4, pp. 2378–2379, 1970.

[17] Z. I. Alferov, F. A. Ahmedov, V. I. Korol’kov, and V. G. Nikitin, “Phototransistor utilizing a GaAs–AlAs heterojunction,” Fiz. Tekn. Poluprovodn., vol. 7, pp. 1159–1163, 1973.

[18] Z. I. Alferov, V. M. Andreev, V. I. Korol’kov, V. G. Nikitin, and A. A. Yakovenko, “p-n-p-n structures based on GaAs and on Al Ga As solid solutions,” Fiz. Tekn. Poluprovodn., vol. 4, pp. 578–581, 1970.

[19] H. M. Manasevit, “Single crystal GaAs on insolating substrates,” Appl. Phys. Lett., vol. 12, p. 156, 1968.

[20] J. R. Arthur, “Molecular beam epitaxy,” Elsevier Surface Science, vol. 500, no. 1-3, pp. 189-217, March 2002.

[21] P. D. Dapkus, “Metalorganic chemical vapor deposition,” Ann. Rev. Mater. Sci, vol 12, pp. 243-269, 1982.

[22] R. Dingle, W. Wiegmann, and C. H. Henry, “Quantized states of confined carriers in very thin Al Ga As–GaAs–Al Ga As heterostructures,” Phys. Rev. Lett., vol. 33, pp. 827, 1974.

[23] S. L. Chuang, “Physics of Optoelectronic Devices”, Wiley, 1995.

[24] K. F. Renk, “Quantum Well Lasers from the UV to the Infrared,” Basics of Laser Physics, pp. 485-490, 31 March 2017.

[25] D. W Shaw, “Selective Epitaxial Deposition of Gallium Arsenide in Holes,” The Electrochemical Society, vol. 133, no. 9, 1966.

[26] E. Colas et al, “Lateral and longitudinal patterning of semiconductor structures by crystal growth on nonplanar and dielectric-masked GaAs substrates: application to thickness-modulated waveguide structures,” Journal of Crystal Growth, vol. 107, no. 1-4, pp. 226-230, 1 January 1991.

[27] R. Bhat, “Current status of selective area epitaxy by OMCVD,” Journal of Crystal Growth, no.120, pp. 362-268, 1992.

[28] Emil S. Koteles, "Methods for monolithically fabricating photonic integrated circuits," Proc. SPIE 10278, Defining the Global Information Infrastructure: Infrastructure, Systems, and Services: A Critical Review, 3 November 1994.

[29] J. J. Coleman, “Progress in InGaAs-GaAs selective-area MOCVD toward photonic integrated circuits,” IEEE Journal of Selected Topics in Quantum Electronics, vol. 3, no. 3, pp. 874-884, June 1997.

[30] J. Cai et al, “Very low threshold, Carrier- and Index-Confined Semiconductor Lasers by One Single Selective-Area-Growth,” Optical Society of American, 2005.

[31] H. Debregeas et al, “Selective-area-growth technology for flexible active building blocks,” Advanced Photonics Congress, 2012.

[32] J. Décobert, N. Dupuis, P. Lagrée, and N. Lagay, “240 nm wide wavelength range of AlGaInAs MQWs selectively grown by MOVPE,” International Conference on Indium Phosphide and Related Materials (IPRM), pp. 13–16, 2008.

[33] D. J. Dunstan, “Strain and strain relaxation in semiconductors,” Journal of Materials Science: Materials in Electronics, vol. 8, no. 6, pp. 337–375, 1997.

[34] Q. Zhang, D. Sando and N. Valanoor, “Chemical Route derived Bismuth Ferrite Thin films and Nanomaterials,” Journal of Materials Chemistry, April 2016.

[35] A.M. Jones, “Strained-layer InGaAs-GaAs-InGaP buried-heterostructure quantum-well lasers on a low-composition InGaAs substrate by selective-area MOCVD,” IEEE Photonics Technology Letters, vol. 10, no. 4, April 1998.

[36] C. Luo et al, “Review of recent advances in inorganic photoresists,” RSC Advances, no.14, 2020.

[37] A.G Thompson, “MOCVD technology for semiconductors,” Material Letters, vol. 30, no. 4, pp. 255-263, March 1997.

[38] K. Min et al, “Photoluminescence and Lifetime Measurement for the Excitation and Temperature Dependence of Carrier Relaxation in III-V Semiconductors,” Materials Science, 2018.

[39] “Lock-in Amplifier and Applications,” Lehigh Edu., https://www.lehigh.edu/~jph7/website/Physics262/LockInAmplifierAndApplications.pdf.

[40] M. Walock, “Nanocomposite coatings based on quaternary metal-nitrogen and nanocarbon systems,” Thesis for: Doctorate (A& ParisTech), November 2012.

[41] S. Nasir et al, “Potential Valorization of By-product Materials from Oil Palm: A review of Alternative and Sustainable Carbon Sources for Carbon-based Nanomaterials Synthesis,” Bioresources, November 2018.

[42] L. A. Coldren, S. W. Corzine and M. L. Masanovic, “Diode Lasers and Photonic Integrated Circuits,” Wiley, 2012.

[43] J. Nayyar et al, “Theoretical estimation of optical absorption and photoluminescence in nanostructured silicon; an approach to improve efficiency in nanostructured solar cells,” Thesis for: Masters (Mich. Tech.), January 2010.

[44] S. Kar, "Effect of Out-Tunnelling Leakage and Electron-Hole Asymmetry on Modulation Response of Semiconductor Double Tunning-Injection Quantum Dot Lasers," Thesis for: Masters (Virginia Poly. Tech.), January 2019.

[45] S. Mokkapati and C. Jagadish, "III-V Compound SC for optoelectronic devices," Materials Today, April 2009.

7. Appendices

7.1. Appendix A

Density of States [42]

An electron within a crystal structure will behave like a free electron moving in a region of uniform potential if it is along the energy momentum available quantum mechanical state curve shown below in Figure A.1. This approximation allows for complex understanding of lattice periodicity regardless of the potential of the crystal. In the finite dimensions (d_x, d_y, d_z) we can approximate the lattice periodicity to that of a constant a.

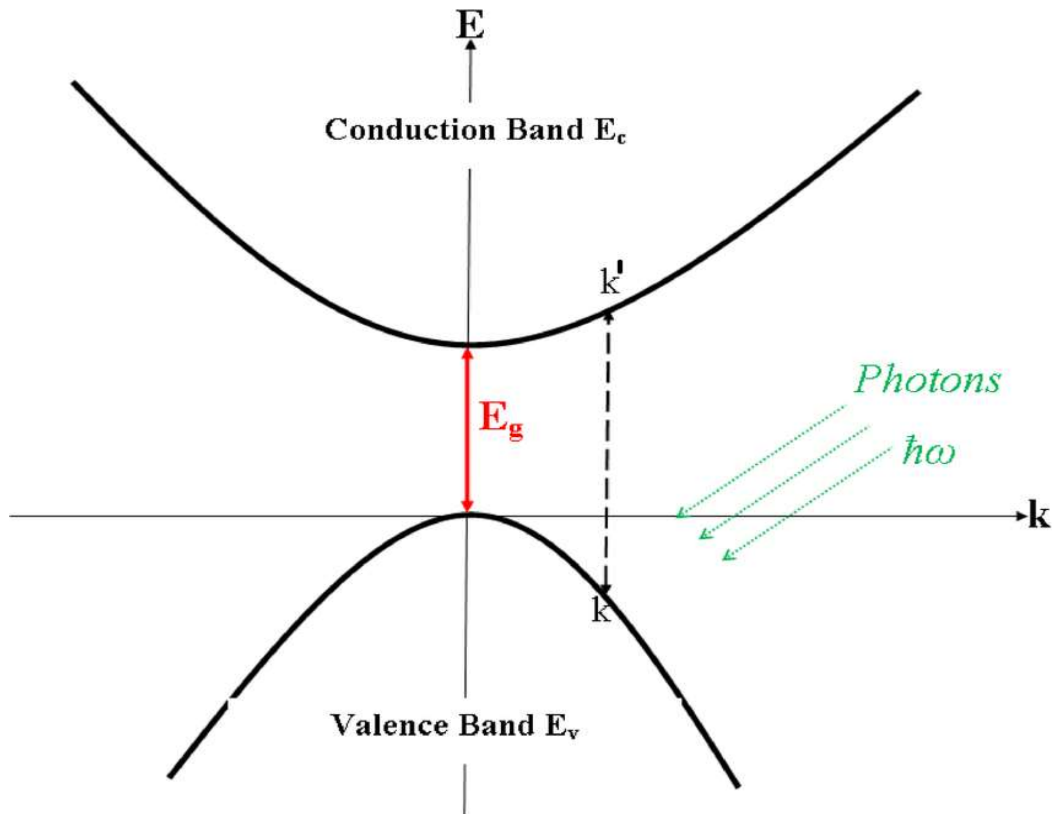

Figure A.1: E-k curve for available quantum mechanical states [43]

The energy momentum (E-k) curve can define a potential based on momentum coordinates and the effective mass which is defined in A.1.1.

$$m^* = \frac{\hbar^2}{d^2E/dk^2} \quad \text{(A.1.1)}$$

The energy can therefore be defined in A.1.2 with the boundary conditions of large potential barriers, given the assumption ($k_j d_j = n_j \pi$), with completeness and uniformity in all directions of the effective mass A.1.3.

$$E = \frac{\hbar^2 k^2}{2m^*} = \frac{\hbar^2}{2m^*} = \frac{\hbar^2}{2m^*}[{k_x}^2, {k_y}^2, {k_z}^2] \quad \text{(A.1.2)}$$

$$E = \frac{\hbar^2 k^2}{2m^*} = \frac{\hbar^2}{2m^*} = \frac{\hbar^2}{2m^*}[\left(\frac{n_x}{d_x}\right)^2, \left(\frac{n_y}{d_y}\right)^2, \left(\frac{n_z}{d_z}\right)^2] \quad \text{(A.1.3)}$$

The quantum confinement regime of states become apparent when d_j < 100 nm, above this regime is considered a bulk continuum of states. We can define both regimes by the counting of available states in what is called the carrier density or density of states. The density of states, ρ, can be utilized as an integral over some range in E-k space to determine the number of states in that specific range. If N_s is the number of states up to some given point, we can generally state equation A.1.4, leading to the formulation of A.1.5 where u is the desired variable and V is the volume.

$$N_s(\text{u}) = \text{V}\int_0^u \rho(u)du \quad \text{(A.1.4)}$$

$$\rho(u)du = \frac{1}{V}dN_s(u) \quad \text{(A.1.5)}$$

To solve for the density of states the number of states for the volume of $N_s(\text{n})$ or n-space is calculated. Then the desired variable is substituted as $n = f(\text{u})$ which gives $N_s(\text{u})$ and lastly

equation A.1.5 is applied to determine the desired $\rho(u)du$. For example, in the bulk regime, $N_s(\text{n})$ is given by A.1.6.

$$N_s(\text{n}) = \frac{4}{3}\pi n^3 \cdot 2 \cdot \frac{1}{8} \quad \text{(A.1.6)}$$

The approximation of volume is given for a spherical coordinate yet written in rectangular coordinates for continuity with A.1.5. The factor of 2 relates to the spin degeneracy at each allowed energy while the factor of 1/8 pertains to the availability and existence of only the positive quantum numbers. The equation can be rewritten substituting for E instead of n-space in spherical coordinates (A.1.7).

$$N_s(\text{E}) = \frac{\pi}{3}\left(\frac{2m^* E d^2}{\hbar^2 \pi^2}\right)^{3/2} \quad \text{(A.1.7)}$$

Lastly apply the third step involving equation A.1.5 where $V = d^3$.

$$\rho(\text{E})dE = \frac{1}{2\pi^2}\left[\frac{2m^*}{\hbar^2}\right]^{3/2} E^{1/2} dE \quad \text{(A.1.8)}$$

We can extend this methodology to different dimensions including the quantum well 2-dimensional approach that is a fundamental part of this work. First define one of the dimensions as the "small" dimension, in this case d_z. The energies of this regime are given by A.1.3. and there no longer exists a third variable for dimension k_z, leaving k_x and k_y. The volume is therefore one quadrant of positive quantum numbers multiplied by 2 for spin degeneracy formulating A.1.9.

$$N_s(n_{xy}) = \frac{\pi}{2}({n_x}^2 + {n_y}^2) \quad \text{(A.1.9)}$$

If we once again assume the effective masses are uniform in both directions, we can simplify to A.1.10. The last step to achieving A.1.11. is the substitution of A.1.5. to quantify the density of states for quantum well structures.

$$N_s(E_{xy}) = \frac{m^* d^2}{\pi \hbar^2} E_{xy} \quad \text{(A.1.10)}$$

$$\rho(E) = \frac{1}{d_z} \sum_{n_z} \frac{m^*}{\pi \hbar^2} u(E - E_{n_z}) \quad \text{(A.1.11)}$$

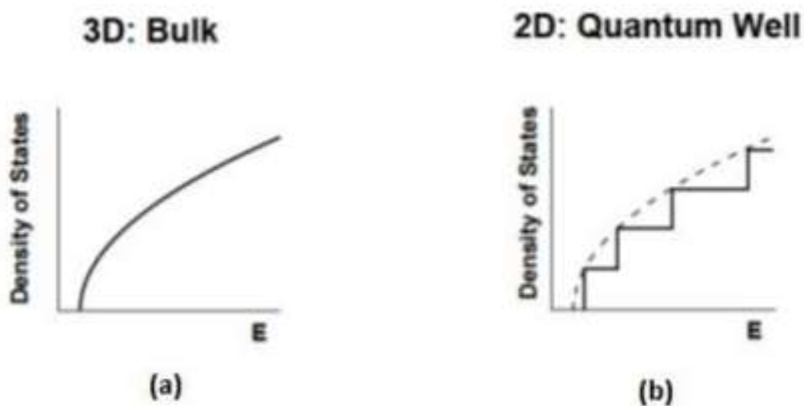

Figure A.2: The density of states as a function of E for different dimensions [44]

7.2. Appendix B

Quantum Confined Stark Effect (QCSE) [42]

The QCSE describes the alteration of subband wave functions by an external applied electric field onto a quantum-well. This effect can alter the light absorption or emission spectrum of the given quantum-well structure by modifying the discrete energy levels. In Figure B.1.1 below, the valence band is bent upwards while the conduction band is bent downwards, this will ultimately lower the required energy to cross the bandgap. The sudden decrease in the energy requirement to cross the bandgap, will fundamentally reduce the recombination efficiency and the amount of permitted light absorption/emission. QCSE is often deployed for optical modulators, to switch optical communications on and off in rapid succession.

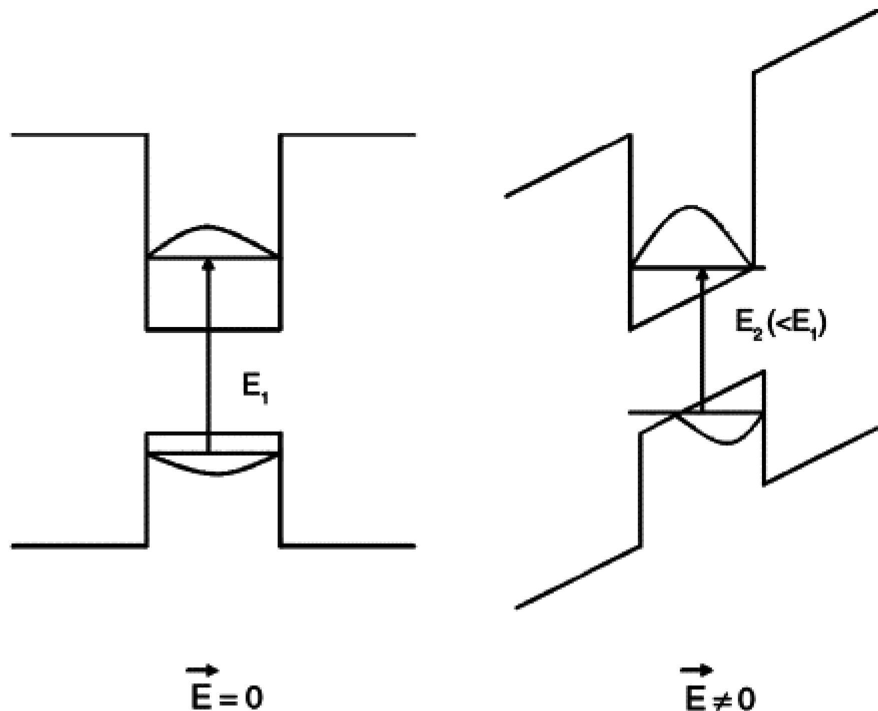

Figure B.1: Quantum Confined Stark Effect (QCSE) - Quantum-well subband bending due to an applied electric field [45]